5-2019

Elucidating the Role of Physiochemical Properties on Gas Transport in Ionic Liquids and Porous Liquids for Carbon Dioxide Separations

Jennifer Ann Schott
University of Tennessee, jschott4@vols.utk.edu

To the Graduate Council:

I am submitting herewith a dissertation written by Jennifer Ann Schott entitled "Elucidating the Role of Physiochemical Properties on Gas Transport in Ionic Liquids and Porous Liquids for Carbon Dioxide Separations." I have examined the final electronic copy of this dissertation for form and content and recommend that it be accepted in partial fulfillment of the requirements for the degree of Doctor of Philosophy, with a major in Chemistry.

Sheng Dai, Major Professor

We have read this dissertation and recommend its acceptance:

Michael Sepaniak, Shawn Campagna, Robert Counce

Accepted for the Council:

Dixie L. Thompson

Vice Provost and Dean of the Graduate School

(Original signatures are on file with official student records.)

Elucidating the Role of Physiochemical Properties on Gas Transport in Ionic Liquids and Porous Liquids for Carbon Dioxide Separations

A Dissertation Presented for the

Doctor of Philosophy

Degree

The University of Tennessee, Knoxville

Jennifer Ann Schott

May 2019

ACKNOWLEDGEMENTS

I would first like to thank my advisor Dr. Sheng Dai for allowing me to part of his dynamic research group. Throughout my time here, there was never a shortage of ideas, group members, or projects to keep me moving. I would also like to thank my committee members Dr. Michael Sepaniak, Dr. Shawn Campagna, and Dr. Robert Counce for contributing their time and feedback to my academic career.

In the last few years, I have had the opportunity to work with so many wonderful people. My sincere appreciation goes out to Dr. Shannon Mahurin and Dr. Richard Mayes for the advice, guidance, and friendship that they have provided. Through many rotations of students, visitors, and postdocs I have so many people to thank. To Kim, Nada, Chi-Linh and Suree – thanks for making sure I felt welcomed into the crowd at UT. To my cubical crew throughout the years – Michelle, Ilja, Matt, KC, Dmitriy, and Halie – thanks for the laughs and keeping things interesting. To the visiting faculty members – Dr. Allison Fleshman, Dr. Craig Teague, and Dr. Pasquale Fulvio – the summers would not have been the same without you. I am also thankful for the friends who reminded me to take a break every few weekends and have game night – Danielle, Rachel, Matt, Jonathan, Kiran, and Josh.

I would also like to thank my family for lending their ears to lengthy phone conversations during my drive home from the lab at odd hours. My sister Kelly has always been one of my biggest advocates. She reminds me of why I am here and never lets me forget my goals. Last but not least, I would like to thank my husband Eric Tague for his constant support, encouragement, and sense of humor. I could not have made it through it all without you.

ABSTRACT

The rising concentration of atmospheric carbon dioxide to unprecedented levels has prompted global initiatives to reduce carbon emissions from anthropogenic sources. However, technologies to support these initiatives are somewhat limited and are not the most economically advantageous for cost to capture ratios. Current strategies using liquid amines are corrosive and have a significant thermal penalty for regeneration. There is a need for a passive, efficient approach for carbon dioxide sequestration. Rather than harnessing a chemical reaction, which requires added energy to release carbon dioxide and reuse the sorbent, other materials that operate by a mechanism of physical interactions will be explored.

Membranes are a low energy alternative for gas separations but require thoughtful design to circumvent the inherent permeability-selectivity tradeoff. To mitigate this effect, ionic liquids (ILs) were functionalized to enhance carbon dioxide selectivity between gases of interest. Cations were designed to reduce cation-anion interactions and increase free volume in efforts to enhance permeability, but gains were minimized due to increased viscosity of the new ILs. New relationships between fractional free volume and gas solubility were examined.

Mixed matrix mediums have recently gained prominence for their ability to bridge the gap between permeability and selectivity. Ionic liquid absorbents are adept at selectively separating light gases, while porous adsorbents with large surface areas have high capacities at low partial pressures. Porous liquids are a new class of fluid sorbents that combine the positive attributes of both components. Through judicious selection of the liquid and dispersed colloidal solid, permanent cavities can be achieved in the liquid phase. A porous liquid was created using zeolitic imidazolate framework nanocrystals incorporated into a bulky ionic liquid. The composite exhibited distinct enhancements in both gas solubility and selectivity.

In situ Fourier transform infrared spectroscopy measurements were conducted to investigate the mode of carbon dioxide absorption in the porous liquids. While the liquid

phase remains relatively unchanged, incorporation of carbon dioxide leads to slight structural fluctuations in the porous solid and liquid. The presence of both dissolved and gaseous carbon dioxide was detected, and preliminary quantitation was completed.

TABLE OF CONTENTS

CHAPTER 1. INTRODUCTION 1
1.1 Motivation 2
1.2 Objectives 3
1.3 Background on Separations 4
1.3.1 Diffusion 4
1.3.2 Sorbents 7
1.3.3 Membranes 8
1.4 Membrane Permeability Analysis 11
1.5 Isothermal Gas Sorption 14
1.5.1 Manometric Analysis 16
1.5.2 Gravimetric Analysis 19
1.6 Organization of Dissertation 20
1.7 References 22
CHAPTER 2. PROGRESSION OF RESEARCH 24
2.1 Dense Membranes 25
2.2 Atomically Thin 2-D Membranes 25
2.2.1 Graphene Synthesis and Characterization 26
2.2.2 Graphene Transfer and Removal of CVD Catalyst 28
2.2.3 Graphene Membrane Assembly and Testing 31
2.2.4 Preliminary Conclusions on Ultrathin Membranes 39
2.3 Alternative Strategies to Reduce the Effective Thickness 39
2.4 From Mixed Matrix Membranes to Porous Liquids 43
2.5 References 45
CHAPTER 3. SUPPORTED BICYCLIC AMIDINE IONIC LIQUIDS AS A POTENTIAL CO_2/N_2 SEPARATION MEDIUM 50
3.1 Publication Statement 51
3.2 Abstract 51

3.3 Introduction 52
3.4 Experimental 54
3.4.1 Materials and Ionic Liquid Synthesis 54
3.4.2 COSMOtherm Calculations 56
3.4.3 Characterization Methods 56
3.4.4 Membrane Preparation and Gas Permeation Measurements 57
3.5 Results 58
3.5.1 Structural and Physical Properties 58
3.5.2 Viscosity 63
3.5.3 CO_2 Solubility 66
3.5.4 Free Volume 70
3.5.5 SILM Single Gas Measurements 72
3.5.6 Calculated Diffusivity Values 74
3.6 Discussion 75
3.6.1 Permeation Properties 75
3.6.2 The Role of FFV in Solubility 77
3.7 Conclusions 79
3.8 Acknowledgements 80
3.9 Supporting Information 80
3.9.1 Synthetic Procedure 80
3.9.2 Supporting Figures 85
3.10 References 89
CHAPTER 4. NEW CLASS OF TYPE III POROUS LIQUIDS: A PROMISING PLATFORM FOR RATIONAL ADJUSTMENT OF GAS SORPTION BEHAVIOR .. 98
4.1 Publication Statement 99
4.2 Abstract 99
4.3 Introduction 100
4.4 Experimental 101
4.4.1 Materials Characterization 101

4.5 Results and Discussion 107
4.6 Conclusions 117
4.7 Supporting Information 120
4.7.1 Chemicals and Reagents 120
4.7.2 Analytical Techniques 120
4.7.3 Positron Annihilation Lifetime Spectroscopy (PALS) 121
4.7.4 Synthesis of Ionic Liquids, Porous Materials, and Porous Liquids 121
4.8 References 132
CHAPTER 5. INVESTIGATING THE MODE OF GAS SORPTION IN POROUS LIQUIDS VIA IN-SITU FTIR STUDY OF CARBON DIOXIDE ISOTHERMS 137
5.1 Abstract 138
5.2 Introduction 138
5.3 Experimental 140
5.4 Results 142
5.4.1 Preliminary Spectroscopic Investigation – Precursors vs. Composite 142
5.4.2 In-situ CO_2 Adsorption Monitored via FTIR 145
5.4.3 CO_2 and Ionic Liquid, [DBU-PEG][Tf_2N]$_2$. 147
5.4.4 CO_2 and Porous Solid, ZIF-8. 150
5.4.5 CO_2 and 20 wt% Porous Liquid 152
5.5 Discussion 154
5.5.1 Moderate Peak Shift in ZIF-8 and Porous Liquid 154
5.5.2 Free CO_2 155
5.5.3 Relative Quantitation of CO_2 157
5.5.4 IR Pathlength 160
5.5.5 Concentration Calculations 163
5.5.6 Additional Structure Factors – XRD 163
5.6 Conclusion 164
5.7 References 167
CHAPTER 6. CONCLUSION 172

6.1 Synopsis 173
VITA 175

LIST OF TABLES

Table 3-1. Physical properties of bicyclic ILs: glass transition (T_g), solid-solid transition ($T_{s\text{-}s}$), melting transition (T_m), decomposition temperature (T_d), percent decomposition ($\%_d$), viscosity (η), and activation energy for viscous flow (E_a) 61

Table 3-2. Calculated values for the IL density (ρ), molar volume (V_m), fractional free volume (FFV). Experimentally determined CO_2 solubility, Henry's constants (HCO_2), gas permeability (P), selectivity (α), and diffusivity (D). All determined at 25 °C unless otherwise noted 68

Table 4-1. Summary of high-pressure experimental and theoretical CO_2 adsorption capacities for as-synthesized porous liquids, pure IL, and porous solids 108

Table 4-2. Textural Properties of as-synthesized porous frameworks..... 112

Table 5-1. IR peaks of interest for pure CO_2, IL, and ZIF-8 144

LIST OF FIGURES

Figure 1-1. Plot of the Stokes-Einstein relationship between viscosity and diffusivity for carbon dioxide (330 pm diameter). To provide a frame of reference, points extrapolated are from literature viscosity values for water and ethylene glycol representing species of different fluidity. 6

Figure 1-2. Robeson plot of polymer membranes (reproduced from Reference[13]) 10

Figure 1-3. Schematic of membrane permeability test system 12

Figure 1-4. Raw data from membrane test system, a plot of pressure vs time. The initial lag time of 1-2 minutes accounts for the gas diffusion through the membrane, followed by a linear slope 13

Figure 1-5. Graphic depicting the solution diffusion process of transport through the membrane. 15

Figure 2-1. A) Raman spectrum of single-layer graphene B) SEM of predominately single layer graphene. Darker "islands" are additional nucleation sites where a second layer is beginning to form 29

Figure 2-2. Photographs of: A) copper foil before (left) and after (right) electropolishing, B) CVD tube furnace and mass flow controllers, C) glow from 1000 °C furnace during CVD of graphene, D) PDMS covered copper foil in etchant bath, E) PMMA coated graphene on silicon wafers, F) graphene on porous filter membrane, G) oxygen plasma etching of graphene 30

Figure 2-3. A) graphical side-view representation of the composite membrane using a silicon wafer with one hole, B&C) top-down SEM images of graphene covering 5 μm hole one intact (B) and one broken (C) with residual polymer contamination, D) Raman spectra of intact graphene over hole before (black) and after (red) oxygen plasma treatment showing appearance of the defect peak at 1350 cm^{-1} 32

Figure 2-4. A) graphical side-view representation of the composite membrane using commercial filter, B) polycarbonate track etch membrane filters – top-down SEM image from Sterlitech, C&D) top-down photograph of two transfers of single-layer

graphene to polycarbonate, E&F) top-down SEM image of graphene coated polycarbonate before (E) and after (F) adding IL 34
Figure 2-5. Dopamine coated graphene. Images captured from optical microscope camera using 20x objective. A&B) showing PMMA coated graphene/dopamine with visible grain boundaries in both images and defects/cracks in the underlying graphene denoted by asterisks, C&D) graphene/dopamine after PMMA removal by solvent (C) or thermal treatment (D) 37
Figure 2-6. SEM cross-section of PMMA-PEO polymer films before (A, C, & E) and after (B, D, & F) solvent extraction 38
Figure 2-7. Graphic depicting the mixed matrix membrane comprised of hollow carbon spheres (HCS) in block copolymer PS-PEB-PS. Reproduced from reference[30] 41
Figure 2-8. a) Gas permeability and b) selectivity as a function of hollow carbon spheres (HCS) loading; c) a Robeson plot for CO_2/N_2 with label 1: the pure block copolymer, and labels 2-8: 5, 10, 20, 30, 40, 60, 80 wt% HCS loadings in the MMM. Reproduced from reference[30] 42
Figure 2-9. Graphic depicting the three main types of porous liquids as defined in the initial concept paper by James et al. Reproduced from reference[33] 44
Figure 3-1. Structures and abbreviations of the bicyclic ionic liquid cations and anions 55
Figure 3-2. FTIR for a) DBU and b) DBN based ILs including labels for some distinctive ▲ cation and * anion features. From top to bottom [Et-][$B(CN)_4$] green, [Me-][$B(CN)_4$] blue, [Et-][Tf_2N] red, and [Me-][Tf_2N] black. 59
Figure 3-3. TGA traces for a) DBU and b) DBN based ILs. [Me-][Tf_2N] black, [Et-][Tf_2N] red, [Me-][$B(CN)_4$] blue, [Et-][$B(CN)_4$] green 62
Figure 3-4. a) Temperature dependent viscosity measurements for the RTILs, and b) corresponding Arrhenius plots 65
Figure 3-5. Carbon dioxide adsorption isotherms for the bicyclic ionic liquids at a) 25 °C and b) 40 °C 67
Figure 3-6. Optimized structures of ions a) [MeDBU], b) [EtDBU], c) [MeDBN], d) [EtDBN], e) [Tf_2N], f) [$B(CN)_4$] 71

Figure 3-7. a) Carbon dioxide (solid) and nitrogen (stripes) permeability of the SILMs. b) Robeson plot showing a representative sample and five bicyclic ILs from this paper 73
Figure 3-8. Plot of solubility and molar volume with Camper's model (red line), literature values (open squares and circles[18]), and the bicyclic ILs with [Tf_2N] (green squares) and [$B(CN)_4$] (blue circles) 78
Figure 3-9. Synthesis scheme for bicyclic ionic salts and liquids 85
Figure 3-10. a) FTIR and b) TGA for bicyclic iodide precursors 86
Figure 3-11. DSC curves for a) bicyclic iodide precursors b) $[DBU]^+$ based ILs c) $[DBN]^+$ based ILs 87
Figure 3-12. 3-D plot showing the relationship between molar volume, fractional free volume, and solubility. Bicyclic ILs with [Tf_2N] (green spheres) and [$B(CN)_4$] (blue spheres), and literature ILs [18, 54] (black spheres), with projections onto the xy and yz planes for clarity 88
Figure 4-1. a) molecular formula of [DBU-PEG][Tf_2N]$_2$ ILs and b) top- and side- view of optimized molecular conformation of [DBU-PEG][Tf_2N]$_2$ ILs at the B3LYP/6-31+G(d, p) level 103
Figure 4-2. A Schematic illustration of the formation of ZIF-8 porous liquids 104
Figure 4-3. Positron annihilation lifetime spectroscopy (PALS) of ZIF-8 porous liquid (9.1 wt%). The annihilation lifetime of o-Ps (refer to the period between the generation and annihilation of o-Ps) can be correlated to the average pore size in the materials by the Tao-Eldrup model as following: 106
Figure 4-4. High-pressure CO_2 adsorption-desorption isotherms at 298 K of ZIF-8, ZSM-5, and Silicalite-1 incorporated into: a) [Bmim][Tf_2N] based liquid mixtures with pure [Bmim][Tf_2N] included for comparison, b) [DBU-PEG][Tf_2N]$_2$ based porous liquids, with pure [DBU-PEG][Tf_2N]$_2$ IL included for comparison. 109
Figure 4-5. N_2 adsorption isotherms (77 K) for the as-synthesized porous framework solids 111

Figure 4-6. CO_2 adsorption-desorption isotherms of ZIF-8 porous liquids at 25 °C, [DBU-PEG][Tf_2N]$_2$ IL included for comparison. 113
Figure 4-7. High-pressure (10 bar) CO_2 adsorption-desorption isotherms for pure framework solids. 115
Figure 4-8. TEM images of a) as-synthesized ZIF-8 nanoparticles, and b) as-synthesized ZIF-8 porous liquids (30 wt%) 116
Figure 4-9. Selectivity values for the 30 wt% porous liquid show significant enhancement over those of pure ZIF-8 118
Figure 4-10. Schematic diagram of the positron annihilation lifetime spectroscopy (PALS) system 123
Figure 4-11. General synthetic scheme for synthesis of [DBU–PEG][Tf_2N]$_2$ ionic liquid 124
Figure 4-12. XRD of synthesized ZIF-8, ZSM-5, and Silicalite-1 nanoparticles 128
Figure 4-13. SEM images of as-synthesized ZIF-8 nanoparticles 129
Figure 4-14. a) SEM and b-d) TEM images of as-synthesized ZSM-5 nanoparticles 130
Figure 4-15. a) SEM and b-d) TEM images of as-synthesized Silicalite-1 nanoparticles 131
Figure 5-1. The chemical structures of a) [DBU-PEG][Tf_2N]$_2$ IL; b) ZIF-8 porous framework with tetrahedrons showing the coordination of zinc to 2-methylimidazolate;[4] and c) a graphical schematic depicting the porous liquid. 141
Figure 5-2. a) Image of the setup for in-situ measurements, and b) a graphical representation of the evanescent wave 143
Figure 5-3. Spectra of the two precursors, [DBU-PEG][Tf_2N]$_2$ and ZIF-8, and resultant 20 wt% ZIF-8-PL in the evacuated sample chamber. Points of interest included increased resolution of ZIF-8 features in the PL (marked by *) and changes in relative intensity of IL (marked by arrows). 146
Figure 5-4. Stretching and bending modes of carbon dioxide and representative spectra from empty ATR cell with increasing pressures of CO_2 gas 148

Figure 5-5. In-situ FTIR of [DBU-PEG][Tf_2N]$_2$. Changes in IR absorption with increasing pressure in pure ionic liquid, [DBU-PEG][Tf_2N]$_2$, from vacuum up to 4 bar CO_2. 149
Figure 5-6. In-situ FTIR of ZIF-8. Intensity changes in IR absorption with increasing pressure in pure porous solid, ZIF-8, from vacuum up to 5 bar CO_2. Arrows indicate the direction of intensity change with increasing pressure. Scale bars represent 0.01 arbitrary units of absorbance. 151
Figure 5-7. In-situ FTIR of 20 wt% PL. Changes in IR absorption with increasing pressure in 20 wt% PL, from vacuum up to 7 bar CO_2. Arrows indicate the direction of intensity change with increasing pressure 153
Figure 5-8. Differences in the CO_2 asymmetric stretching region between pure gas and CO_2 sorption into IL, ZIF-8, and PL at 1 bar (a) and 4 bar (b). 156
Figure 5-9. Molecular dynamics showing the interactions of carbon dioxide with the ionic liquid. The bulky cation, [DBU-PEG]$^{2+}$, adopts a bowl shape that expands with increasing CO_2 concentration. 158
Figure 5-10. Trends in absorbance peak heights with increasing pressure for a) IL [DBU-PEG][Tf_2N]$_2$, b) 20 wt% PL, and c) ZIF-8 159
Figure 5-11. Trends in integrated peak areas with increasing pressure for a) IL [DBU-PEG][Tf_2N]$_2$, b) 20 wt% PL, and c) ZIF-8 161
Figure 5-12. XRD of pure ionic liquid (blue) and porous framework (black) with the porous liquid (red) derived from ~5 wt% combination of the two. 165

ABBREVIATIONS AND SYMBOLS

α	selectivity coefficient
ATR	attenuated total reflectance
$[B(CN)_4]$	tetracyanoborate
BET	Brunauer-Emmett-Teller
[bmim]	1-butyl-3-methylimidazolium
CO_2	carbon dioxide
CCS	carbon capture and sequestration
CVD	chemical vapor deposition
δ	solubility parameter
D	diffusion coefficient
DBU	1,8-diazabicyclo[5.4.0]undec-7-ene
DBN	1,5-diazabicyclo[4.3.0]non-5-ene
DI	deionized
DSC	differential scanning calorimetry
η	viscosity
[emim]	1-ethyl-3-methylimidazolium
FFV	fractional free volume
FTIR	Fourier Transform Infrared Spectroscopy
FWHM	full width at half maximum
H_{CO2}	Henry's constants for CO_2
HS	hollow sphere
IL	ionic liquid
IR	infrared spectroscopy
J	flux
K	equilibrium constant
λ	wavelength
m	mass

M_i	molecular mass
MMM	mixed matrix membrane
MOF	metal organic framework
N_A	Avogadro's number
NIST	National Institute of Standards and Technology
P_a	permeability of gas a
p	partial pressure
p/p°	relative pressure
PALS	positron annihilation lifetime spectroscopy
PDMS	polydimethylsiloxane
PEO	poly(ethylene oxide)
PL	porous liquid
PMMA	poly(methyl methacrylate)
PTMSP	poly(1-trimethylsilyl-1-propyne)
R	gas constant
ρ	density
RST	Regular Solution Theory
RTIL	room temperature ionic liquid
σ	cross section
SEM	scanning electron microscopy
SILM	supported ionic liquid membrane
T	temperature
T_d	decomposition temperature
[Tf_2N]	bis(trifluoromethanesulfonyl)imide
T_g	glass transition
TGA	thermal gravimetric analysis
T_m	melting transition
V_m	molar volume
XRD	X-ray diffraction

ZIF-8	zeolitic imidazolate framework-8

CHAPTER 1. INTRODUCTION

1.1 Motivation

Measurements by the National Oceanic and Atmospheric Administration have shown that atmospheric carbon dioxide (CO_2) is currently at the highest level compared to recorded historical data, averaging 408 ppm worldwide in late 2018. According to the U.S. Energy Information Administration 1,555 million metric tons of carbon dioxide was produced in 2015 from coal fired power plants alone.[1] The current technology for carbon capture in industry is scrubbing with liquid amines. CO_2 reacts in a 1:2 ratio with primary amines forming a carbamate salt,[2] and in the presence of water creates hydrogen carbonate.[3] The drawback of this method is the regeneration of the amine solvent takes place at high temperatures and pressures creating a significant energy requirement. Also, due to the corrosive nature and volatility of the solvent the process is not "green". Environmental concerns have shown the need for more efficient, cost effective, and less energy intensive carbon capture techniques.

A primary limitation for catch and release type systems are the overall energy expenditures. Typically, the “best” sorbent materials have the strongest attractions due to favorable, exothermic reaction pathways which are most effective during the initial removal stage. These spontaneous chemical reactions with high enthalpy of adsorption, low activation energies, and high molar capacities fit the need precisely for catching the species of interest for removal. However, the more favorable the initial reaction, the less favorable the reverse pathway becomes. Emissions streams are high volume systems and therefore require processing of large quantities of gases. Engineering of these systems necessitates a regeneration step to minimize the quantities of sorbent species required. Endothermic processes are required to release the captured gas to regenerate and reuse solvents.

The energy cost to clean the flue gas using traditional amine “scrubbers” can reduce the power produced by 30% or more, making the process less efficient losing both time and money. There is a need for a low energy, low cost alternative for carbon capture and sequestration. Ideal systems must be optimized for both catch and release.

1.2 Objectives

Before carbon capture and sequestration (CCS) can gain prominence and become commercially viable, more research must be completed to create the most economically feasible option. Therefore, investigating sorbent species with low enthalpy change and high solubility will be one goal of this research. To this end, attention will be directed to physical interactions with sorbents rather than chemical reactions. A variety of physical sorbents have been investigated for carbon capture including porous materials, e.g. activated carbon and metal organic frameworks, as well as unique solvents such as ionic liquids. In general, porous materials allow for relatively high capacity but are limited by low selectivity. On the contrary, ionic liquids are specifically tailored to the task allowing for high selectivity but those that operate on physisorption tend to be limited by lower capacity.

The objective of this research will be to develop and characterize advanced materials to find ideal characteristics between these tradeoffs. Prior research using ionic liquids (ILs) has shown that molar volume and cation-anion interactions are important factors in carbon dioxide solubility. These relationships prompt a series of questions aimed to further optimize carbon capture technologies through a better understanding of the physical and chemical interactions with the solute. Can a balance between strong attraction and quick diffusion be achieved in ionic liquids? Can high free volume liquids be created? Unique ILs were designed by integrating CO_2-philic moieties in a nontraditional format to interrogate this question. Some of the highest gas throughput is seen in high free volume polymers. By increasing the internal voids in solution phase, can capacity and permeance enhancements be achieved? Leveraging knowledge of both the benefits and limitations of solid and liquid sorbents, designs for a “smart” sorbent from mixed matrix materials attempt to harness these effects to promote synergy between different mediums. Further studies will proceed to evaluate the structure and its evolution during the carbon capture process.

1.3 Background on Separations

Some background to support the interrogation of these questions comes from accepted theories which sought to answer similar questions focused on relatively simple systems. One theory of molecular transport in liquids modelled the molecules as hard spheres, while later works laid the foundation for understanding systems of increased complexity. The relationships between diffusivity, fluidity, and free volume are now being analyzed in novel systems. For membrane based separations, the product of solubility and diffusivity describe the permeability.

1.3.1 Diffusion

One way to quantify transport properties is through Fick's law of diffusion,[4] which describes the flux, *J*, of matter in a certain area over a given time interval.

$$J = -D\frac{dn}{dx}$$

where *D* is the diffusion coefficient, *n* is the number density of particles (molecules/m^{-3}), and *x* is the position. The rate of diffusion varies with the magnitude of the concentration gradient with respect to position. In open spaces where the molecular mean free path exceeds the diameter of the path the collisions are primarily with walls instead of other molecules.[5]

$$D_{K,i} = \frac{d}{3}\left(\frac{8RT}{\pi M_i}\right)^{1/2}$$

Here, Knudsen diffusion (D_K) dominates, the diffusion of gases is inversely proportional to the square root of the molecular mass (M_i). This type of transport is common in porous mediums.

Diffusion within normal liquids with high number density per unit area can furthermore be described as the random Brownian motion of molecules. Therefore, the diffusion constant ($D_{S\text{-}E}$) of a given material could instead be defined by the Stokes-Einstein equation,[6] which relates the movement of a spherical particle to the fluidity of the medium

$$D_{S-E} = \frac{RT}{N_A} \cdot \frac{1}{6\pi\eta r}$$

using the gas constant (R), temperature (T), and Avogadro's number (N_A), combined with the viscosity of the diffusion medium (η) and the hydrodynamic radius of the particle (r). Using this hard-sphere model, one can generate a graphical representation (**Figure 1-1**) of the influence of viscosity on diffusivity. A variety of ionic liquids have been used throughout this dissertation. These liquids have relatively high viscosity when compared to water or ethylene glycol, therefore methods to enhance the diffusivity will be subsequently discussed.

Cohen and Turnbull later proposed a free volume theory,[7] on the basis that a significant fraction of molecules are constantly in a transition state that allows for self-diffusion, a movement that is governed by the presence of transient holes of that are continually redistributing throughout the bulk phase. Their work is analogous to the fluidity model of Stokes-Einstein but with more rigorous attention to physical equilibria and distribution of intermolecular vacancies. In this case the diffusion coefficient was dependent on the proportion of holes greater than a critical volume (v^*) and their possible overlapping regions (γ) in relation to the total free volume (v_f) at a given temperature (T). Additional prefactors were included to account for geometric (g) parameters of a given molecule with diameter a^*.

$$D = g a^* T^{\frac{1}{2}} e^{\frac{-\gamma v^*}{v_f}}$$

$$v_f = \alpha \bar{v}_m (T - T_0) - \beta \bar{v}_p \Delta P$$

The free volume can be further defined using the average values of the thermal expansion coefficient (α) and molecular volume ($\bar{v}_m$) at a given temperature range and the average compressibility (β) and molecular volume ($\bar{v}_p$) at a specific pressure interval (ΔP).

While all these findings are based on simple systems with predominately van der Waals forces, they stand as a frame of reference for discussion in later parts of the text. The gases of interest flow along concentration gradients, while their diffusion is primarily controlled by molecular mass in large open spaces, and by viscosity and free volume in

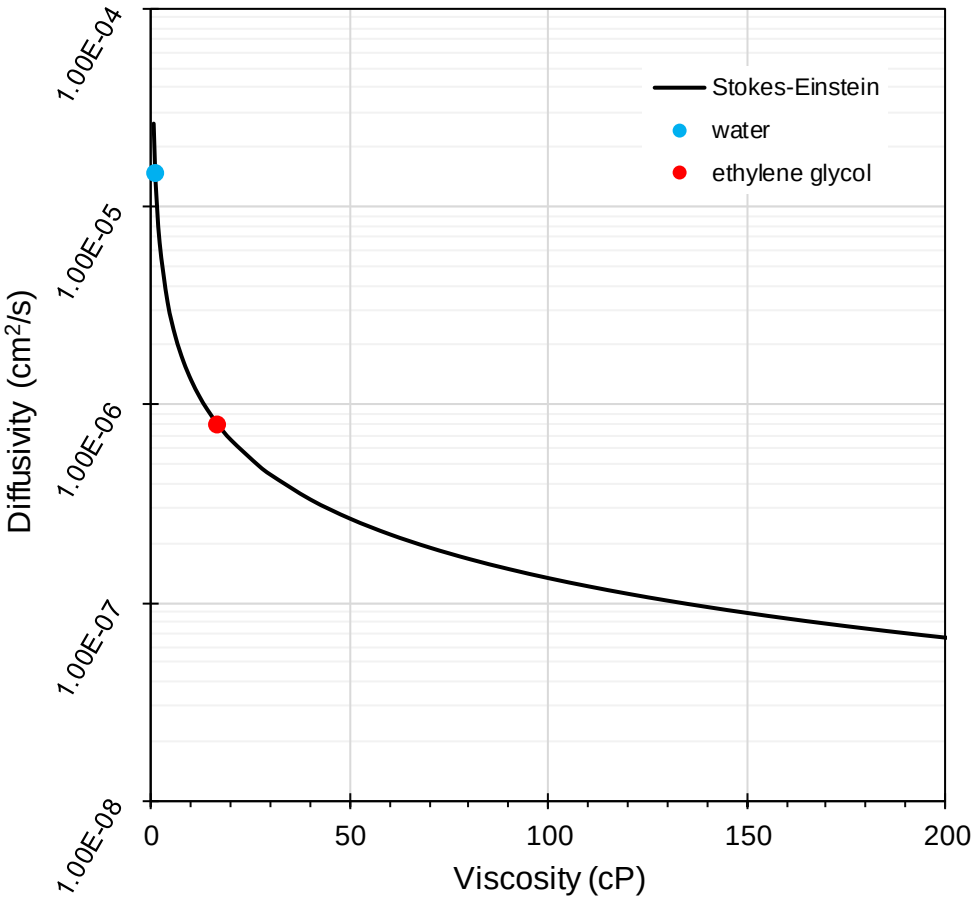

Figure 1-1. Plot of the Stokes-Einstein relationship between viscosity and diffusivity for carbon dioxide (330 pm diameter). To provide a frame of reference, points extrapolated are from literature viscosity values for water and ethylene glycol representing species of different fluidity.

fluids and other dense mediums. The concept of free volume has continually been a focus of those in the field of membrane separations and has allowed for a better understanding of mass transport through polymer films. Herein, it will allow us new insights to similar systems including ionic liquids and mixed matrix sorbents.

1.3.2 Sorbents

There are two primary classes of sorbents which depend on the mode in which sorption occurs and the interactions with the sorbate molecule. Adsorption is distinctly an interfacial process and is limited to monolayer surface coverage. When the sorbate extends past this interface and is incorporated into the sorbent on bulk scale, it is known as absorption. Frequently, both adsorption and absorption may occur and in this situation a more generic descriptor, sorption, may be used.

One of the most well-known adsorption models can be described by monolayer gas sorption onto a uniform surface with identical sites and no sorbate-sorbate interactions. This type of Langmuir isotherm can be represented solely by surface coverage or fractional loading, θ, where K is the equilibrium constant and p is the partial pressure of adsorbate gas.

$$\theta = \frac{Kp}{1 + Kp}$$

The Langmuir adsorption, by definition, is limited to a statistical monolayer. However, after initial surface coverage, multilayer coverage can occur due to sorbate-sorbate interactions and capillary condensation. Additional parameters relating to differences in surface sites and porosity can be determined with knowledge of the excess adsorbate.

For absorption measurements when the amount absorbed is low, the system can be considered at infinite dilution. In this regime, Henry's law applies and the solubility coefficient (S), also known as Henry's constant, can be determined

$$C = Sp$$

from the concentration (C) and the partial pressure (p). Henry's constants are readily used in the field of molecular solvents and ionic liquids. However, the most unified presentation of data is using mole fractions rather than concentrations.

Regular solution theory (RST) has been commonly used to describe binary mixtures where the energies deviate from ideal solutions and the enthalpy of mixing is nonzero due to differences in interactions between the two species.[4] In real or regular solutions where the solute-solvent interactions are stronger than the interactions of the individual components with themselves, this leads to an exothermic heat of mixing. Hildebrand defined solubility parameters for the solvent (δ_1) and solute (δ_2) using the enthalpy of mixing (ΔH) and the volume fraction of solvent (φ_1) and molar volume of solute (V_2).[8-9]

$$\Delta H = \phi_1^2 V_2 (\delta_1 - \delta_2)^2$$

$$\delta = \left(\frac{E_{vap}}{V_m}\right)^{1/2}$$

Where the solubility parameter is dependent on both the energy of vaporization (E_{vap}) and the molar volume (V_m) of the solvent. Noble's group has had success fitting traditional liquids using a modified version of these RST equations using Henry's constants.[10] However, using RST is not so simple with ionic liquids since the vapor pressure is so small. The energy of vaporization for ILs is not easily determined making the solubility parameter difficult to calculate. Camper proposed using the Kapustinskii equation to simplify the equation using only the molar volume.[11] The relationship between solubility and molar volume will be further addressed in Chapter 3.

1.3.3 Membranes

Cycling of liquid sorbents is a known strategy for executing CCS, however the large quantity of sorbent can be cost prohibitive. Therefore, another method for implementation of liquid sorbents can be in supported liquid membranes (SLMs). Traditional SLMs have more drawbacks due to volatility of the liquid phase. However, in the case of ionic liquids with negligible vapor pressures evaporation is no longer a problem.

A key factor in membrane separations is the overall permeability, which is a quantification of the analyte's ability to pass through the membrane medium. The ideal permeability (P_a) of a membrane is determined via the gas flux (J) through a membrane of thickness (l) over a certain pressure drop (Δp). The ratio of the more permeable species (a) to the less permeable species (b) is known as the selectivity coefficient (α_{ab}).

$$P_a = J\frac{l}{\Delta p}$$

$$\alpha_{ab} = \frac{P_a}{P_b}$$

The ideal gas separation membrane would have high values of both permeability and selectivity. However, typically the easier it is for gases to flow through a membrane, the less selective it becomes. This tradeoff between the permeability and selectivity of a membrane was well studied. In 1991 Robeson assembled data for the separation of various light gases through polymer membranes and coined the terminology "the upper bound" for the slope n of the line of which virtually all known measurements fell below.[12] This line represents the correlation between the permeability (P_a), the selectivity (α_{ab}), and the 'front factor' (k).

$$P_a = k\alpha_{ab}^n$$

Robeson's publication provided a clear goal for those in the field of membrane gas separations, to surpass the upper bound. The substantial growth that followed is apparent and a new upper bound (**Figure 1-2**) was published in 2008.[13] While the boundary is listed for polymeric membranes, it provides a great frame of reference for analyzing other supported liquid membranes as well.

In general, polymeric films have some of the highest recorded permeability due to large free volumes but are limited by low selectivity between gases. Task specific ionic liquids can be tailored to achieve some of the highest selectivity values between gases, making the nonvolatile liquids a great option for supported liquid membranes. However, ILs have relatively high viscosity which limits the diffusivity of gases and therefore only

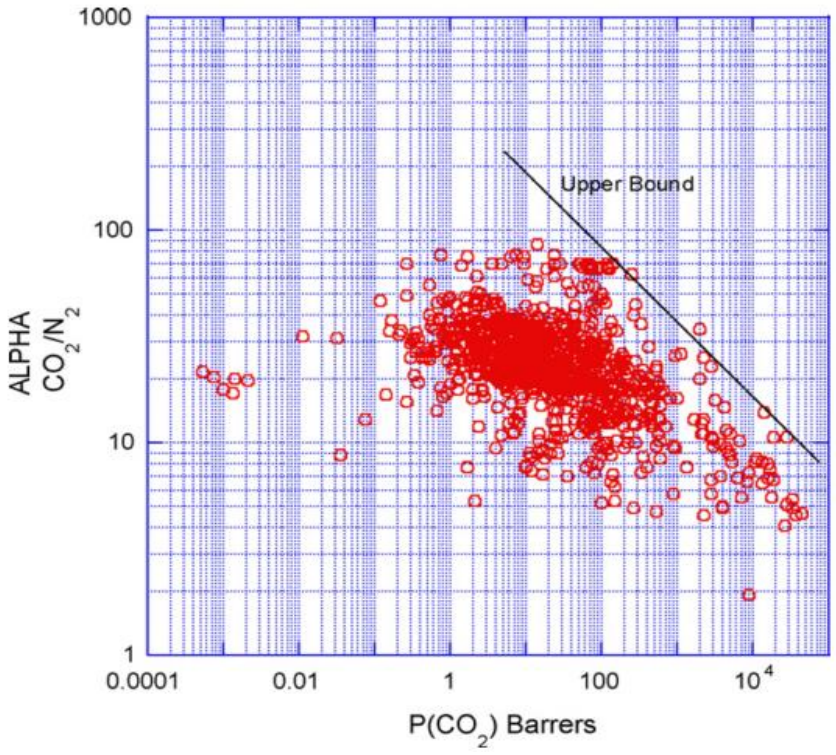

Figure 1-2. Robeson plot of polymer membranes (reproduced from Reference[13])

moderately high permeabilities are achieved. One promising strategy to get around the permeability-selectivity tradeoff is the use of mixed matrix materials. Chapters 4 and 5 investigate the use of complementary materials to create next generation sorbents. Additionally, since permeability is directly proportional to thickness, the analysis of nanoscale membranes could provide insight to unique features opposed from their bulk counterparts. This approach is explored through the creation of atomically thin membranes in Chapter 2.

1.4 Membrane Permeability Analysis

To test the permeation properties of membrane materials, a custom built apparatus was used.[14] The membrane test system consists of a cell in which the membrane to be examined is placed as a separator across which the flux is recorded via pressure transducer (**Figure 1-3**). Membranes are equilibrated in the sample chamber under vacuum to outgas and desorb any gases present. An assortment of gas lines are connected via a ballast system with a pressure gauge, as shown, for a static measurement. Alternatively, mass flow controllers can be connected to the feed side of the sample cell for a dynamic mixed gas measurement. Multiple Swagelok ball valves or needle valves are strategically placed throughout the manifold system. This allows for a specified pressure or concentration of gas to be applied on the feed side of the membrane, while the downstream side remains evacuated prior to measurement. A pressure transducer on the permeate side of the sample chamber records the change in pressure over time. From these measurements, the gas permeance through the membrane can be determined.

For reference, raw data from the test system pressure transducer is presented in (**Figure 1-4**). The data acquisition system is initialized at concurrent timing as the opening of the ballast valve. Following the dosing of gases into the analysis chamber, there is a clear time delay before an increase in pressure is recorded. This “lag time” correlates to the time each gas requires to penetrate the membrane medium. Different samples will have

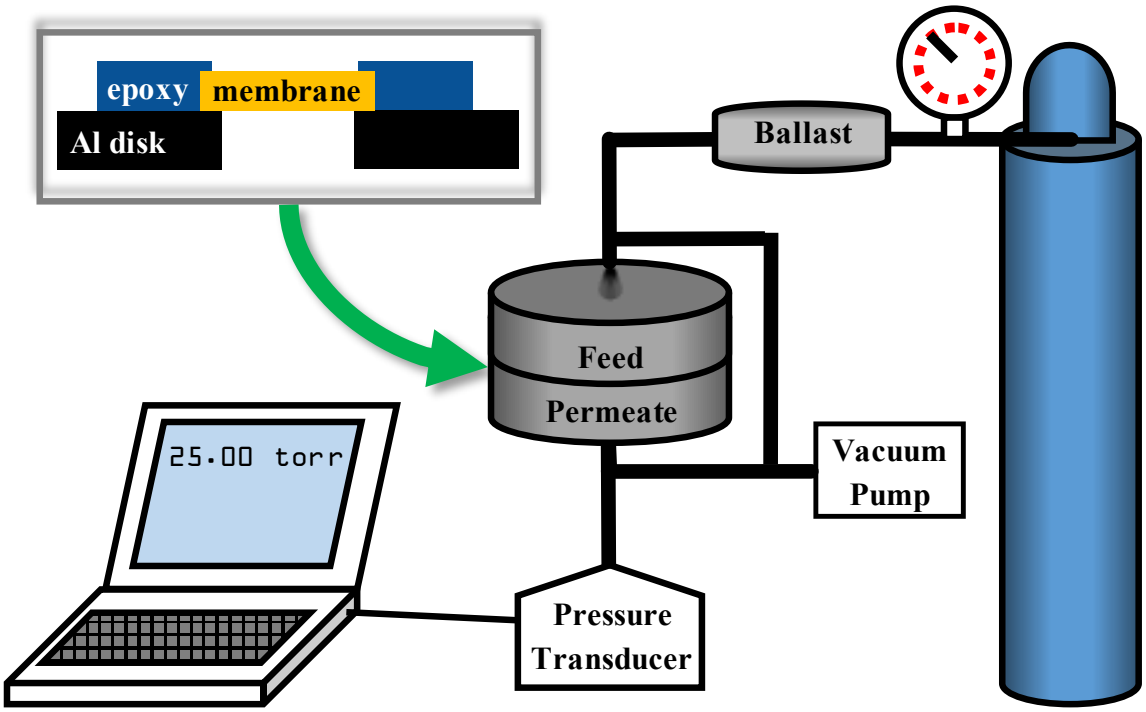

Figure 1-3. Schematic of membrane permeability test system

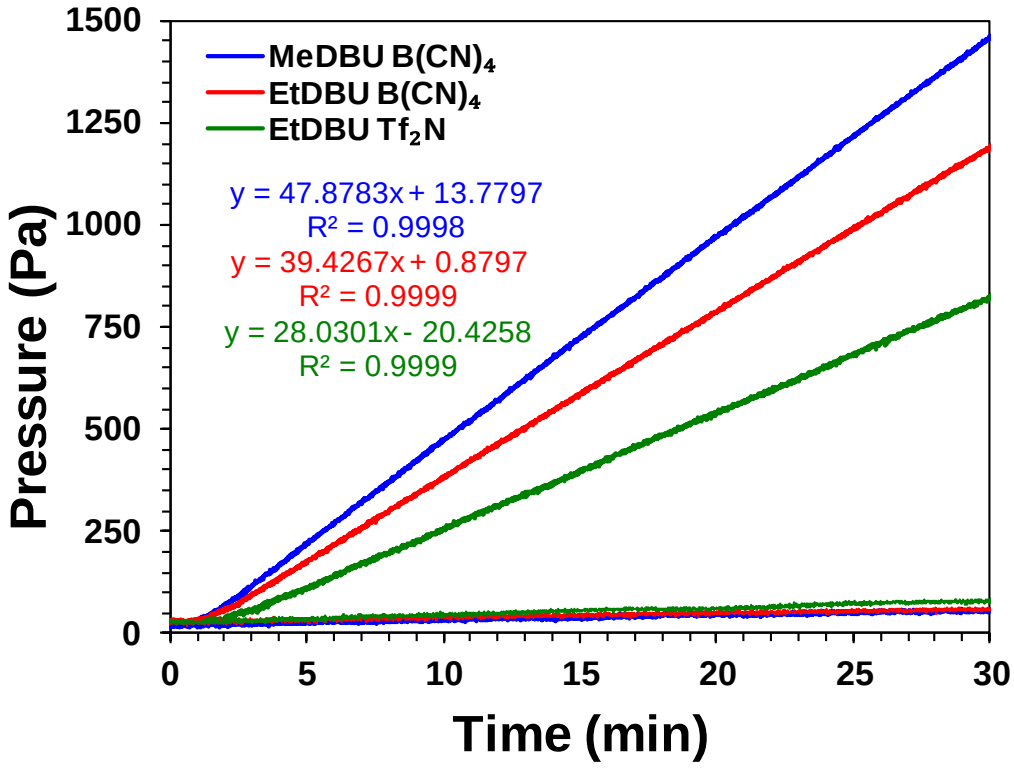

Figure 1-4. Raw data from membrane test system, a plot of pressure vs time. The initial lag time of 1-2 minutes accounts for the gas diffusion through the membrane, followed by a linear slope

varying lag times, which can be correlated to the diffusivity of the gas through the membrane. For most light gases such as the ones in question, CO_2 and N_2 – as well as several others like CH_4, H_2, and O_2 – the diffusivity in ionic liquids is quite similar. Permeation of supported ionic liquid membranes operates on the same principle as polymer membranes, through a solution diffusion mechanism (**Figure 1-5**). Therefore, the determining factor of increased selectivity in the membranes is primarily due to the differences in solubility between the two gases.

For supported liquid membranes, both the porosity and tortuosity of the porous support must be taken into consideration to isolate the features of the liquid. This can be determined by infiltration of a known reference material to determine the tortuosity or curvature in the porous path. Subsequently, the area and thickness of the ionic liquid are determined for the composite membrane. Two methods of determining the membrane area have been used. For large specimens, high-resolution digital calipers were used to measure the diameter at several positions around the circular membrane. However, even using an average from multiple measurements there is inherent uncertainty in area due to non-uniform epoxy coverage. Therefore, a new strategy was adopted using computer image analysis. Photographs of the membrane and a ruler were captured and processed using ImageJ. The ruler was used to create a digital scalebar, and a sufficient number of points around the circumference of the membrane were selected to create an accurate rendering of the membrane shape. The software was then used to calculate the area enclosed by these points. Membrane thickness was determined using a micrometer. Further details on the permeability and selectivity calculations are provided in Chapter 3.

1.5 Isothermal Gas Sorption

There are two primary methods to experimentally record a gas adsorption isotherm, which are named according to the detection method. The first is a manometric technique where pressures are recorded, while the second is a gravimetric technique where mass is

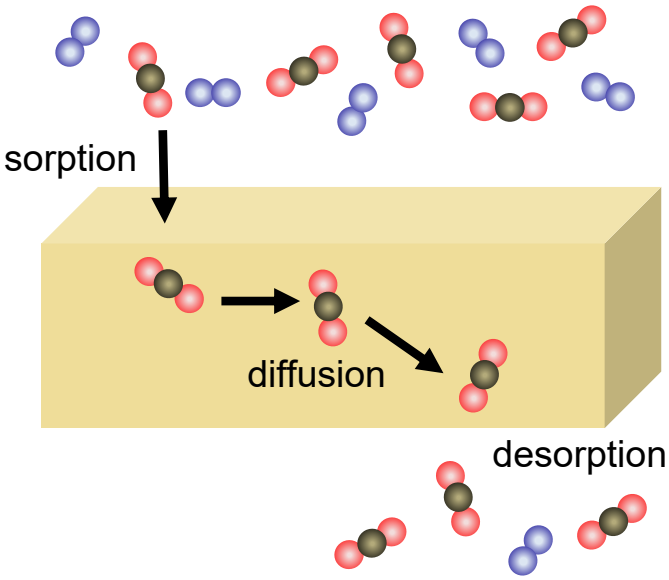

Figure 1-5. Graphic depicting the solution diffusion process of transport through the membrane.

recorded. Each have their own benefits and special considerations necessary for best measuring practices which will be discussed in the following sections.

Regardless of the analysis technique, proper preparation of the sample prior to measurement is incredibly important. A preliminary outgassing procedure is required to obtain an accurate analysis of the sample capacity, where any atmospheric sorbate species are removed. Primary contaminants include both surface and bulk sorbed gases and water. Desorption of these species can be accomplished at elevated temperatures under flow of inert gas, but the chosen temperature should remain sufficiently below the region of thermal instability. Flowing inert gas is adequate for most samples, however outgassing the sample under vacuum may be necessary to if there are ultramicropores with diameters approaching the molecular cross section of the desired adsorbate gas.

A variety of manometric adsorption instrumentation has been used including: Micromeritics Tristar 3000, Micromeritics Gemini VII, Micromeritics 3-flex, and Quantachrome Autosorb-1. Additionally, the Hiden Intelligent Gravimetric Analyzer was used for absorption experiments. Each of these instruments operates by dosing prescribed volumes of the analysis gas, followed by an equilibration time, and then measurement of the equilibrated cell pressure or mass. Specific intervals of relative pressures are selected to produce a gas adsorption isotherm, from which several sample parameters can be distinguished.

1.5.1 Manometric Analysis

The manometric, also referred to as volumetric, method is the most commonly employed for surface area and porosity analyzers. Due to their most common use they are frequently given the misnomer of "BET" due corresponding to the Brunauer-Emmett-Teller (BET) fitting of the resulting dataset. These instruments provide an ideal setup for measurements at cryogenic temperatures since there is direct contact between sample container and thermostatic bath. These instruments are suited to examine low pressures with starting values as low as 10^{-7} torr. Equipped with high resolution parani gauges and

one or more additional transducers, these instruments are well suited for sub-monolayer to multilayer measurements but are pressure limited to 1 bar due to the glass sample tubes. With current manometric setups it is difficult to obtain kinetic data or monitor sample equilibration, however multiple samples can be analyzed at a time using a common manifold.

As with other analytical measurements, the sample size is dependent on concentration. To obtain reasonable data one must not under or over load the instrument with an inappropriate amount of sample. For reliable measurements, a minimum of 20-50 m^2 of surface area should be used for an adsorption experiment. Either prior knowledge of similar samples or repeat measurements are typically required. For low surface area materials high masses are necessary, while only small masses are needed for high surface area materials. Predominately high surface area samples will be investigated throughout this research, for example a surface area of 400+ m^2/g necessitates sample sizes on the order of 100 mg or less. Reducing the area analyzed allows for equilibrium to be established sooner and provides a quicker analysis, however it is important to maintain enough sample so that it is representative of the bulk material.

Mass measurements are recorded before and after sample preparation but are completed ex-situ which allow for potential sample contamination and can affect the reliability in mass measurements. The mechanism of both dosing and measuring pressure can introduce propagated errors in measurement, which can be exacerbated by changing cold and warm volumes. Most experiments are conducted at sub-ambient to cryogenic temperatures where evaporation of the cooling agent creates difficulties in measurement. Effects can be mitigated by reducing the empty volume in the sample tubes with the addition of glass filler rods and adding isothermal jackets which use capillary action to wick the receding cryostat to the same level on the sample tube.

Void Volume. Prior to analysis, each cell containing the sample must be calibrated by a void volume determination. Each of the instruments have the option to measure void

volume using the nonadsorbing gas, helium. The void volume or dead space is determined by independent measurements of the warm and cold free space:

$$V_{WFS} = \frac{V_{man}}{T_1} \times \left(\frac{P_1}{P_2} - 1\right) \times T_{std}$$

$$V_{CFS} = \frac{V_{man}}{T_2} \times \left(\frac{P_1}{P_3} - 1\right) \times T_{std}$$

Where V_{WFS} and V_{CFS} are the volumes of warm and cold free space, respectively, and V_{man} is the manifold volume all in units of cm^3 at standard temperature, T_{std}, of 273.13 K. The temperatures, T_1 and T_2, are the manifold temperature prior to the helium dose and after raising the Dewar and equilibrating with helium, also in Kelvin. The pressures P_1 and P_2 are the manifold pressures in mmHg before and after dosing helium onto the sample and P_3 is the pressure after raising the Dewar and equilibrating with helium. Following the determination of the warm and cold free space, the sample cell is evacuated, and the isotherm measurement can begin. For samples with pores less than 2 nm consideration must be taken of when this measurement is completed since helium can become entrapped in these tiny pores. This could require an additional outgassing and measurement, or alternatively the free space determination can be completed post analysis. Data recorded during these measurements are absolute pressures for the sample cell and a reference station and quantity adsorbed at standard temperature and pressure.

Surface Area and Porosity. The most common application of this technique in the literature is nitrogen adsorption at 77 K. From the adsorption isotherm, the surface area of the sample can be determined as well as the porosity. With this measurement the Brunauer-Emmett-Teller (BET) surface area can be calculated, following the generation of a "BET plot" where *n* is the specific amount adsorbed at the relative pressure *p/p°*

$$\frac{p/p^\circ}{n(1 - p/p^\circ)} = \frac{C - 1}{n_m C}(p/p^\circ) + \frac{1}{n_m C}$$

the monolayer capacity (n_m) can be determined, and *C* is a constant related to energy of adsorption.[15-16] The linear region of the plot is usually around *p/p°* 0.1-0.3 for mesoporous materials, but in the presence of micropores it shifts to much lower relative pressures.

Accurate selection of the proper BET region can be confirmed using the Rouquerol criterion.[17] From here, the monolayer capacity can be used to determine the BET surface area (a_s) for a the test sample of mass (m) using the cross-sectional area of the adsorbate molecule (σ_m).

$$a_s = \frac{n_m L \sigma_m}{m}$$

The data not only provides details on the surface area but can also yield information on the size distribution of the porosity. The Kelvin equation can be used to provide detail on the meoporosity due to capillary condensation. For smaller pores, using a thickness plot, t-plot, and nonporous reference curve can be used to determine the micropore volume

1.5.2 Gravimetric Analysis

While manometric analysis is aptly suited for analysis at cryogenic temperatures, gravimetric analysis is preferred by many because its instrumental design incorporates a stainless-steel reactor vessel capable of high-pressure measurements. Another advantage of this setup is that samples can be activated or outgassed in-situ and be monitored in real time. The testing apparatus consists of a tungsten hang down wire that holds the sample bucket opposite a similar setup for the counterweight. The gravimetric microbalance monitors the mass change over time and sample equilibrium can be determined precisely. Each measurement is independent of the former, generating discrete values where the potential for errors in weighing are diminished and propagated errors are eliminated.

Additionally, since the detector records the mass over time, this method is useful to simultaneously study the kinetics of adsorption. Gravimetric analysis is rarely used in surface area determinations due to the instrument setup, since the sample container is suspended inside a reactor vessel it is therefore more difficult to obtain reliable cryogenic temperatures throughout the duration of the measurement. Again, multiple transducers allow for a wide range of measurement pressures from as low as 10^{-7} torr up to 20 or 150 bar, depending on the instrument. While the gravimetric method can provide a more precise

measurement, additional considerations of buoyancy effects must be made especially at high pressures.

Buoyancy Correction. At high pressure it is important to consider the entire system in which the total force, f_{tot}, has two components. The first is the downward force of the sample, f_s, due to the sample mass, m_s, and acceleration due to gravity, g. The second is the upward force from buoyancy, f_{buoy}. The theory behind the buoyancy correction is Archimedes' principle, where the buoyancy is determined using the density of the sample and gas respectively, ρ_s and ρ_g, both of which are dependent on the measurement temperature and pressure.

$$f_{tot} = f_s - f_{buoy}$$

$$f_{tot} = m_s g - m_s g \left(\frac{\rho_g}{\rho_s}\right)$$

For accurate corrections at high pressures, the density of both the sample and the gas must be known precisely. The National Institute of Standards and Technology (NIST) database for thermophysical properties of fluid systems has accurate data for the gases used here.

1.6 Organization of Dissertation

In Chapter 1, an introduction to the research motivation and objectives was discussed along with some background information. Additionally, an overview of the methods and strategy in data analysis were addressed with comments on important practices in measurement and considerations for design of experiments.

Chapter 2 outlines the progression through early projects including the creation and optimization of ultrathin membranes. Additional alternative methods were identified to enhance quick permeation, and connections were made to the current state of the project.

Chapter 3 focuses on a series of new bicyclic ionic liquids used in supported ionic liquid membranes for gas separation. Through thoughtful synthetic design, these new ILs

possess high free volume in a more compact molar volume than traditional ILs. The juxtaposition of bicyclic amidine ILs and alkyl imidazolium ILs allows insight into previously unrecognized relationships between the IL structure and gas permeation properties.

Chapter 4 investigates the incorporation of free volume into the liquid phase by molecular engineering a composite fluid. This new system, termed a porous liquid, incorporates solid porous materials into a non-penetrating liquid medium in a colloidal suspension. This incorporation of intrinsic permanent porosity allows for significant enhancement of gas storage compared to the pure liquid.

Chapter 5 further probes the mechanism of CO_2 sorption the into the porous liquid via in-situ FTIR at low to moderate pressures. Upon examination of the spectral features from the individual precursors the liquid phase shows no differences upon sorption, while the porous framework structure is clearly changing. Interestingly, differences in the carbon dioxide signal could provide preliminary insights to its unique phase behavior in the three different mediums.

Chapter 6 provides a summary of the current state of the project, including key findings and perspective on future directions for continued research.

1.7 References

1. U.S. Department of Energy, E. I. A., Independent Statistics & Analysis *Short-Term Energy Outlook: Renewables and Carbon Dioxide Emissions*; December 8, 2015.

2. Ramdin, M.; de Loos, T. W.; Vlugt, T. J. H., State-of-the-Art of CO_2 Capture with Ionic Liquids. *Ind. Eng. Chem. Res.* **2012,** *51* (24), 8149-8177.

3. Kumar, S.; Cho, J. H.; Moon, I., Ionic liquid-amine blends and CO(2)BOLs: Prospective solvents for natural gas sweetening and CO2 capture technology-A review. *Int. J. Greenh. Gas Control* **2014,** *20*, 87-116.

4. Atkins, P.; de Paula, J.; Friedman, R., *Quanta, Matter, and Change: A Molecular Approach to Physical Chemistry*. W.H. Freeman and Company: New York, 2009.

5. Benitez, J., *Principles and Modern Applications of Mass Transfer Operations*. 3rd ed.. ed.; New York : John Wiley & Sons, Incorporated: 2016.

6. Miller, C. C., The Stokes-Einstein Law for Diffusion in Solution. *Proceedings of the Royal Society of London. Series A, Containing Papers of a Mathematical and Physical Character (1905-1934)* **1924,** *106* (740), 724-749.

7. Cohen, M. H.; Turnbull, D., Molecular Transport in Liquids and Glasses. *The Journal of Chemical Physics* **1959,** *31* (5), 1164-1169.

8. Hildebrand, J. H., *Regular solutions*. Englewood Cliffs, N.J.: Prentice-Hall: 1962.

9. Miller, J. M., Chromatography : concepts and contrasts. 2nd ed.. ed.; Hoboken, N.J. : John Wiley: Hoboken, N.J., 2005.

10. Bara, J. E.; Carlisle, T. K.; Gabriel, C. J.; Camper, D.; Finotello, A.; Gin, D. L.; Noble, R. D., Guide to CO2 Separations in Imidazolium-Based Room-Temperature Ionic Liquids. *Ind. Eng. Chem. Res.* **2009,** *48* (6), 2739-2751.

11. Camper, D.; Bara, J.; Koval, C.; Noble, R., Bulk-Fluid Solubility and Membrane Feasibility of Rmim-Based Room-Temperature Ionic Liquids. *Ind. Eng. Chem. Res.* **2006,** *45* (18), 6279-6283.

12. Robeson, L. M., Correlation of separation factor versus permeability for polymeric membranes. *J. Membr. Sci.* **1991,** *62* (2), 165-185.

13. Robeson, L. M., The upper bound revisited. *J. Membr. Sci.* **2008,** *320* (1–2), 390-400.

14. Mahurin, S. M.; Lee, J. S.; Baker, G. A.; Luo, H.; Dai, S., Performance of nitrile-containing anions in task-specific ionic liquids for improved CO_2/N_2 separation. *J. Membr. Sci.* **2010,** *353* (1-2), 177-183.

15. Thommes, M.; Kaneko, K.; Neimark Alexander, V.; Olivier James, P.; Rodriguez-Reinoso, F.; Rouquerol, J.; Sing Kenneth, S. W., Physisorption of gases, with special reference to the evaluation of surface area and pore size distribution (IUPAC Technical Report). In *Pure Appl. Chem.*, 2015; Vol. 87, p 1051.

16. Sing, K. S. W.; Everett, D. H.; Haul, R. A. W.; Moscou, L.; Pierotti, R. A.; Rouquerol, J.; Siemieniewska, T., REPORTING PHYSISORPTION DATA FOR GAS SOLID SYSTEMS WITH SPECIAL REFERENCE TO THE DETERMINATION OF SURFACE-AREA AND POROSITY (RECOMMENDATIONS 1984). *Pure Appl. Chem.* **1985,** *57* (4), 603-619.

17. Rouquerol, J.; Llewellyn, P.; Rouquerol, F., Is the bet equation applicable to microporous adsorbents? In *Stud. Surf. Sci. Catal.*, Llewellyn, P. L.; Rodriquez-Reinoso, F.; Rouqerol, J.; Seaton, N., Eds. Elsevier: 2007; Vol. 160, pp 49-56.

CHAPTER 2. PROGRESSION OF RESEARCH

2.1 Dense Membranes

For carbon capture and sequestration, the most viable option would be the least energy intensive. Membranes provide a passive solution with a minimal footprint. Ionic liquids (ILs) are attractive because their selectivity is primarily dependent on solubility and the ideal selectivity is similar to the mixed gas selectivity. Supported ionic liquid membranes (SILMs) because they can be tailored in many ways. Different structural supports with no native selectivity of their own can impart unique effects when holding the same ionic liquid due to interactions at the solid-liquid interface. In the literature, the most commonly used supports are commercially available porous polymer and inorganic membranes. Ionic liquids are held inside these porous supports via adhesion due to capillary forces, so if pore sizes are too large, high transmembrane pressures can be detrimental. Increased pressure drops are capable of pushing IL out of macroporous supports, so a transition to smaller diameter mesopores should provide stronger forces to hold the IL in the support.[1] Enhancements in transmembrane stability are important, but should not be at the expense of overall flux. For relevant applications, such as flue gas CCS, the gas throughput needs to be high. Therefore, materials with large permeability are becoming increasingly important. One of our goals is to develop new SILMs with greater permeability by increasing the free volume through decreased cation/anion interactions. These SILMs will be discussed further in Chapter 3.

2.2 Atomically Thin 2-D Membranes

Task specific ionic liquids are known for having good specificity and higher selectivity between species than traditional polymer membranes. Still, even SILMs for gas separations are limited by the distinct permeability/selectivity tradeoff. The dense films cannot reach the high flux that some polymers can achieve. The ultimate goal for efficiency is to create a highly permeable membrane that maintains its selectivity. Since permeance is inversely proportional to the thickness, an ideal membrane would be ultra-thin but also very strong. The properties of graphene make it an ideal candidate for an atomically thin

yet durable membrane.[2] Since pristine graphene is impermeable, sub-nanometer size holes must be created to make the graphene porous. Methods to create these holes include ion bombardment or oxygen plasma exposure. The porous graphene can then be used as a support for task specific ionic liquids with high carbon dioxide solubility. Each of these tasks are independently feasible – creation of defect free graphene, the addition of porosity to graphene, and using ionic liquids to impart selectivity in less selective medium. This section will further describe the successes and challenges during the creation of macroscopically supported 2-D graphene membranes.

2.2.1 Graphene Synthesis and Characterization

Some of the earliest preparations of graphene were completed via micromechanical cleavage[3] or exfoliation of graphite followed by reduction of graphene oxide.[4] Preparation via these methods creates flakes of graphene with significant defects, which is not desirable for creating large area single-layer graphene. For this reason, a technique using metal catalysts in chemical vapor deposition (CVD) of carbon precursors to create graphene. Nickel was one of the first metal catalysts, but its high carbon solubility often yielded multilayer graphene with small domain sizes. The work of Li et al[5] in 2009 was the first to show that a large area of predominately single-layer graphene could be achieved by using a copper foil catalyst in the CVD process instead. This method prompted subsequent publications from others optimizing conditions including temperature and methane partial pressure,[6] the hydrogen flow,[7] and the role of surface oxygen[8] to improve upon the quality of graphene.

According to Vlassiouk, the surface preparation of the copper catalyst[9] has significant effects on the nucleation and growth of graphene. Therefore, prior to CVD a rigorous solvent cleaning will be implemented, followed by electropolishing in concentrated phosphoric acid. Polishing the copper provides a smoother catalyst surface which can help reduce the number of nucleation sites, yielding larger domains. There are many procedures in the literature with slight variations in the annealing and growth process

which are somewhat system dependent[10]. Since sublimation of copper can be an issue in low-pressure CVD, the temperature was limited to 1000 °C while anneal and growth times were limited between 30-60 minutes. A variety of flow rates and partial pressures will be examined to determine which produces the best quality graphene.

Allotropes of carbon are most commonly characterized by their Raman signal. There are three peaks of significant importance: the graphitic peak around 1580 cm^{-1} (G-band), the 2D-peak around 2700 cm^{-1} (also called G'-band), and the defect peak at 1350 cm^{-1} (D-band). Pristine single-layer graphene has several distinct Raman characteristics[11-12]. There is a sharp G-band at ~1585 cm^{-1} and symmetric shaped 2D-band at ~2680 cm^{-1} with full width at half maximum (FWHM) of approximately 30cm^{-1}. The ratio of intensities for these two peaks is approximately 1:2 respectively. In pristine single-layer graphene, the defect peak should be absent. Initial Raman characterization of the graphene was completed while on the Cu catalyst. While the signal-to-noise ratio is quite poor, this allowed for verification of the presence of graphene without additional processing methods. Following initial verification, a better analysis of quality can be obtained from graphene transferred to a silicon wafer, using the polymer transfer method that will subsequently be described. With the signal to noise ratio improved, the presence or absence of the defect peak can be determined.

In addition to spectroscopic analysis, microscopy can be used for confirmation of graphene quality as well. The scanning electron microscope was resolution limited at approximately 10 nm but still capable of resolving larger features such as the graphene domains, grain boundaries, and the presence or absence of multilayer areas. For analysis of smaller features, a scanning transmission electron microscope can be used with resolving power in the sub-nanometer range. This allows for the imaging of the small defects or pores created by the oxygen plasma.

After spectroscopic analysis, it appears that defect free single-layer graphene has been synthesized using a low-pressure CVD protocol. Ideal conditions involve a 30 minute anneal in hydrogen and a 30 minute growth in a hydrogen/methane mix at 1000 °C, followed by a fast cooldown in flowing hydrogen. Characterization of graphene via Raman

spectroscopy (**Figure 2-1**) shows the 2D-band at 2686 cm^{-1} with FWHM of 31 cm^{-1}, G-band at 1589 cm^{-1}, peak intensity ratio $I_{2D}/I_G \sim 2$, and the absence of a defect peak at 1350 cm^{-1}. Graphene was transferred onto a silicon wafer and examined via the SEM. The image in **Figure 2-1** shows predominately single-layer graphene. The darker lines through the image show the grain boundaries and the small dark regions are nucleation sites where an additional layer of graphene started to form. To reduce the number of these double-layer regions two methods are being tested: increasing the rate of the cooldown and removing the flow of carbon precursor during cooldown.

2.2.2 Graphene Transfer and Removal of CVD Catalyst

While CVD is one of the easiest ways to create single-layer graphene with large domain size, it poses an additional challenge when the graphene is desired without the copper substrate. The typical process for removing the copper catalyst is via chemical etching in either a solution of acidic iron (III) chloride or an ammonium persulfate solution. However, once removed from the copper, the single layer of graphene is delicate and prone to damage in subsequent rinsing and transfer processes. There have been two main techniques developed to allow for a more intact transfer.

One transfer method is conducted in a basic pressing manner where the graphene is placed in conformal contact with the desired substrate, such as a polycarbonate track etch membrane.[13] One caveat to this method is that the desired final substrate must be sufficiently hydrophobic so the interface between graphene/substrate does not wet during the copper removal process, and it is limited to substrates that will not be damaged by the etchant solution. A similar method uses polydimethylsiloxane (PDMS) as a stamp[14-15] which supports the graphene during etching (**Figure 2-2**). Stamping is applicable for transfers to a wider variety of substrates. Also commonly used is a support method where a very thin layer of polymer[16] is coated on top of the graphene/copper via spin coating or similar methods. The polymer layer is cured and then serves as a structural support during

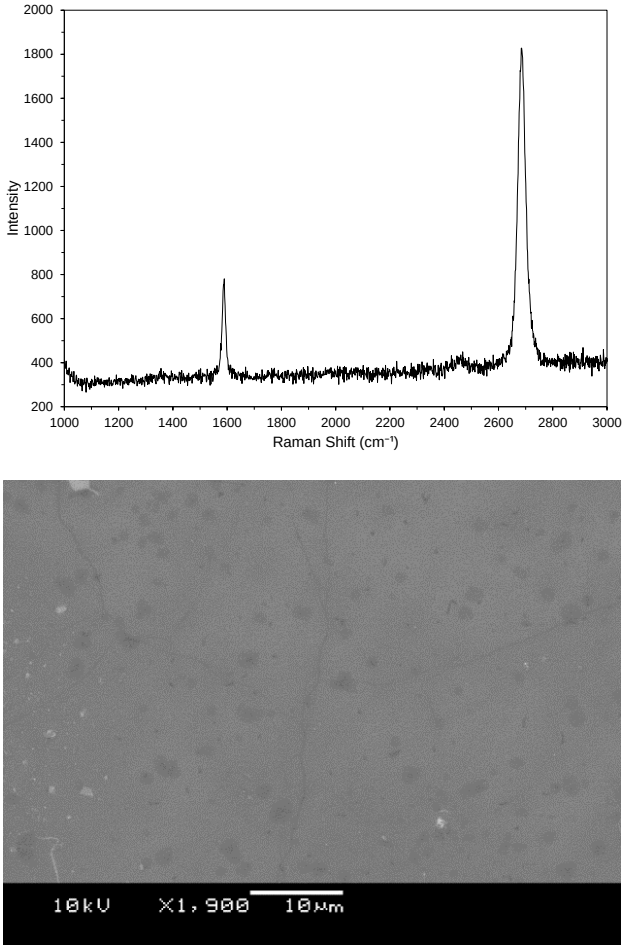

Figure 2-1. A) Raman spectrum of single-layer graphene B) SEM of predominately single layer graphene. Darker "islands" are additional nucleation sites where a second layer is beginning to form

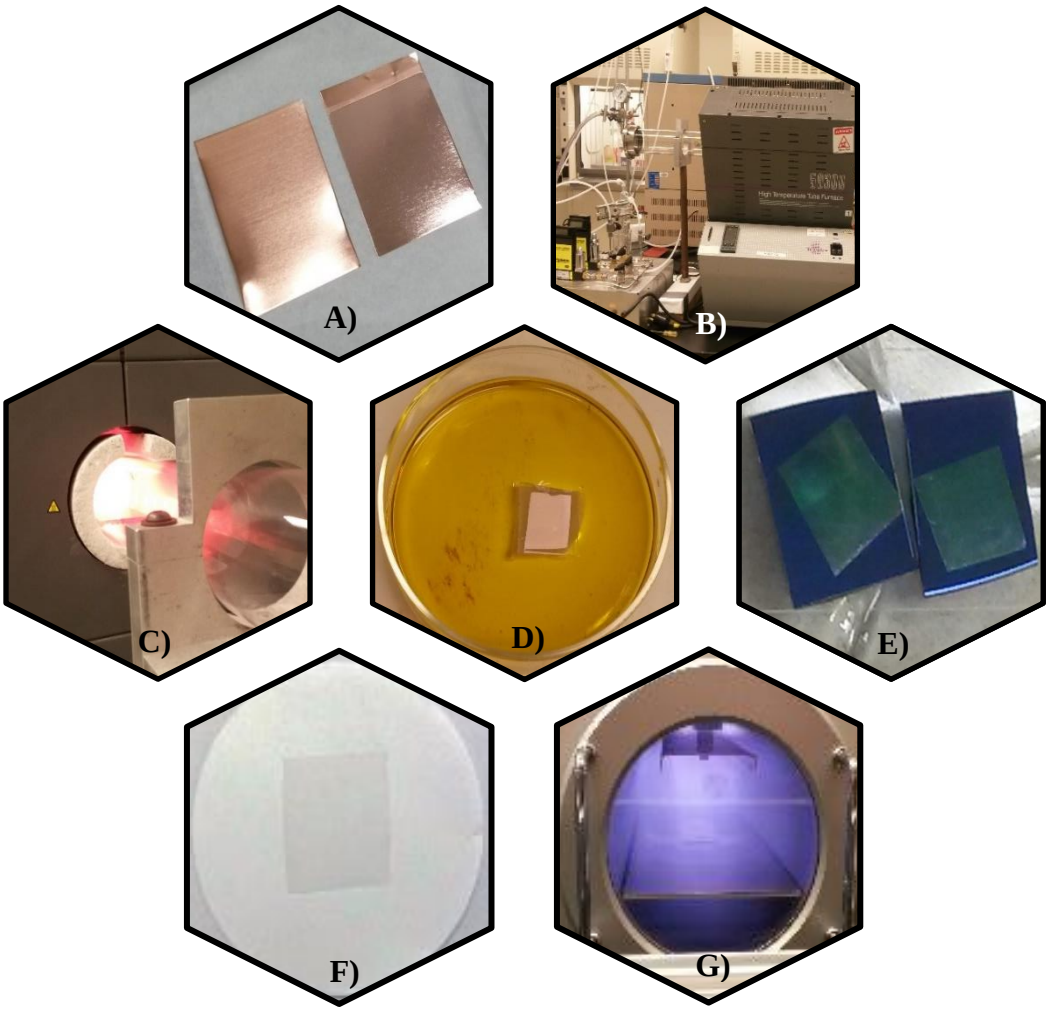

Figure 2-2. Photographs of: A) copper foil before (left) and after (right) electropolishing, B) CVD tube furnace and mass flow controllers, C) glow from 1000 °C furnace during CVD of graphene, D) PDMS covered copper foil in etchant bath, E) PMMA coated graphene on silicon wafers, F) graphene on porous filter membrane, G) oxygen plasma etching of graphene

the etching process. Post etching, the polymer assist layer must be removed upon placement on the final substrate. Therefore, the polymer and its corresponding solvent used for removal must be chosen so they are compatible with the final substrate. Removing residual polymer from the transfer can be problematic, so thermal annealing is sometimes necessary for complete removal. When using a rigid and nonporous substrate, the transfer is uniform with minimal added defects, however if the substrate is a flexible or porous medium transfer defects become more apparent.

Two distinct testing strategies were envisioned to create the atomically thin graphene/IL composite membrane. A small-scale proof of concept method was to suspend graphene over a single micrometer scale hole in a non-porous support such as a silicon wafer or stainless steel pinhole aperture. Graphene domain sizes can be on the order of 50 μm and larger depending on the synthesis conditions. Therefore, using a 5 μm pinhole, the odds of having a single domain cover the entire opening are quite good. This should reduce the impact of grain boundaries or defects, providing a pristine layer of graphene support that is nonporous. Subsequently, the oxygen plasma can be used to create a random assortment of nanopores to which ionic liquids can be added.

2.2.3 Graphene Membrane Assembly and Testing

Starting with the proof of concept strategy, graphene was transferred over a 5 μm hole in a Si wafer (**Figure 2-3**). The quality of transfers to a silicon wafer setup were checked by both SEM and Raman. Approximately 40 percent of the silicon wafer samples showed the intact transfer of the single layer graphene over the hole. A representation of both a good quality transfer and broken sheet of graphene are seen in **Figure 2-3**, where a thin layer can be seen suspended over the hole in the SEM image. For the pinholes successfully covered with graphene, the initial Raman spectra shows no presence of a defect peak (**Figure 2-3.D**, black line). After confirmation from both optical and spectroscopic methods, the wafers were tested in gas permeation chambers. As expected,

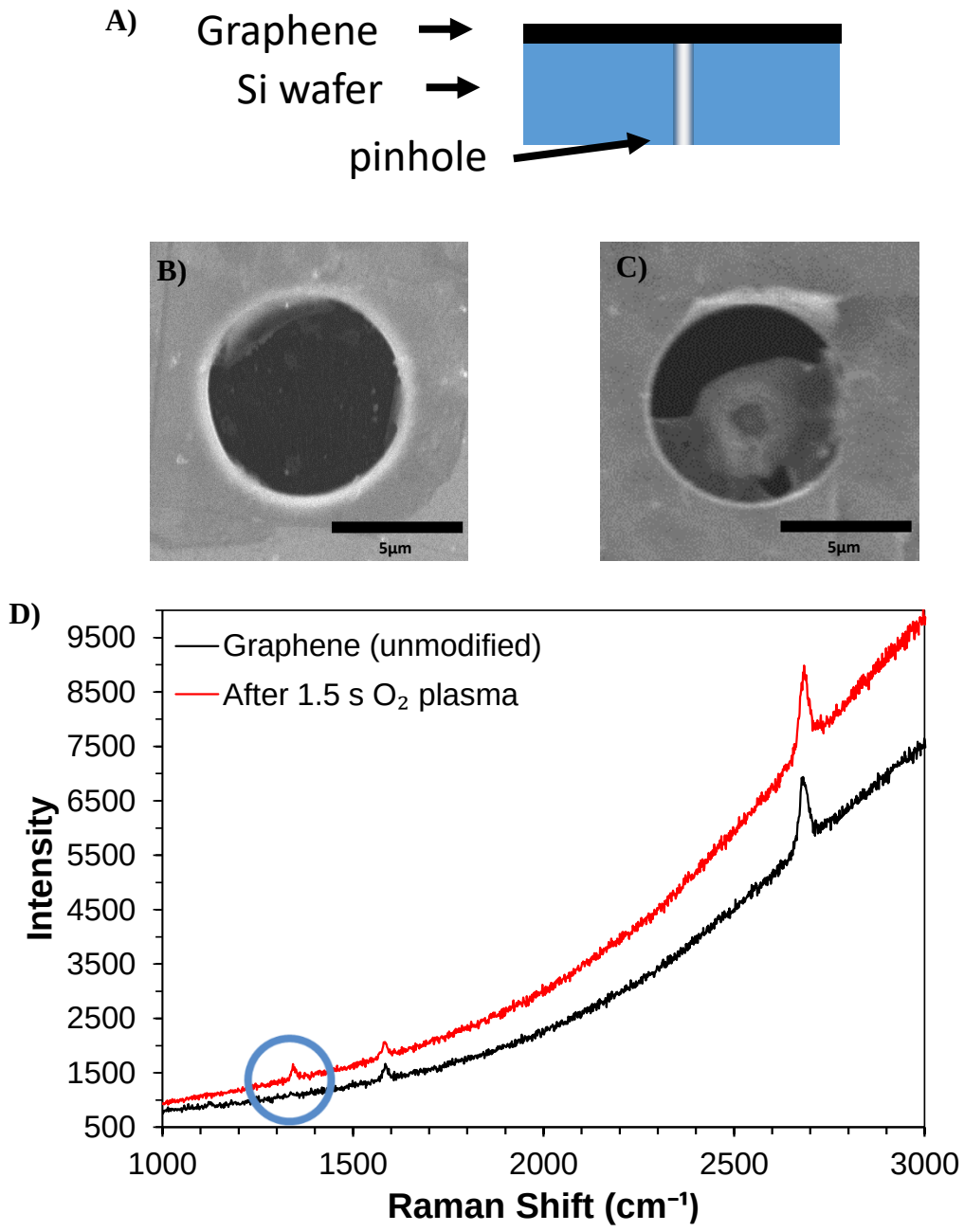

Figure 2-3. A) graphical side-view representation of the composite membrane using a silicon wafer with one hole, B&C) top-down SEM images of graphene covering 5 µm hole one intact (B) and one broken (C) with residual polymer contamination, D) Raman spectra of intact graphene over hole before (black) and after (red) oxygen plasma treatment showing appearance of the defect peak at 1350 cm^{-1}

there was negligible gas transport upon loading of 20 kPa of both CO_2 and N_2 gases, another confirmation of the hole being blocked by the graphene sheet. The samples were then exposed to various lengths of oxygen plasma etching in half second intervals from 0.5-5 seconds. Following 1.5 seconds of treatment, the defect peak at 1350 cm^{-1} becomes clearly present in the Raman spectrum (**Figure 2-3.D**, red line) due to the creation of holes in the graphene sheet. The wafers were loaded once again into the permeation chamber for gas testing, however there was no difference in the transport properties from the baseline measurements. One cause for the lack of permeation could be due to residual PMMA contamination blocking the holes. Another possibility could be due to the reduced dimensions of the overall membrane, the resolution of our system may not be high enough to monitor the changes.

Moving forward, the large-scale alternative was to support a large area of graphene on a porous polymer membrane like those used for traditional SILMs (**Figure 2-4**). Although the polymer assist layer provided stability during transfer, the numerous additional steps required in the transfer the process tend to impart more intrinsic defects in the final graphene.[13, 17] Additionally, the high pore density of the membrane filters lead to imperfect adhesion, which caused more defects in the late stages of testing. Throughout the course of research, a variety of commercial filters were used for structural supports including polycarbonate, polytetrafluoroethylene, and alumina. The most pristine transfers were achieved from conformal contact of the graphene onto polycarbonate during etching. Seemingly successful transfers of the single-layer graphene onto porous polycarbonate membranes appeared to have no large defects under preliminary SEM investigation (**Figure 2-4.E**). Those that showed initial promise were tested with 20 kPa of CO_2 and N_2 but were found to have very fast transport with similar permeance as the structural polycarbonate support. With this information, it was clear there were larger defects present below the resolution limit of the SEM. Assuming these defects were small enough, on the order of a few nanometers, they might be acceptable since nanopores were going to be created via oxygen plasma etching[18] to make add porosity to the graphene. Therefore,

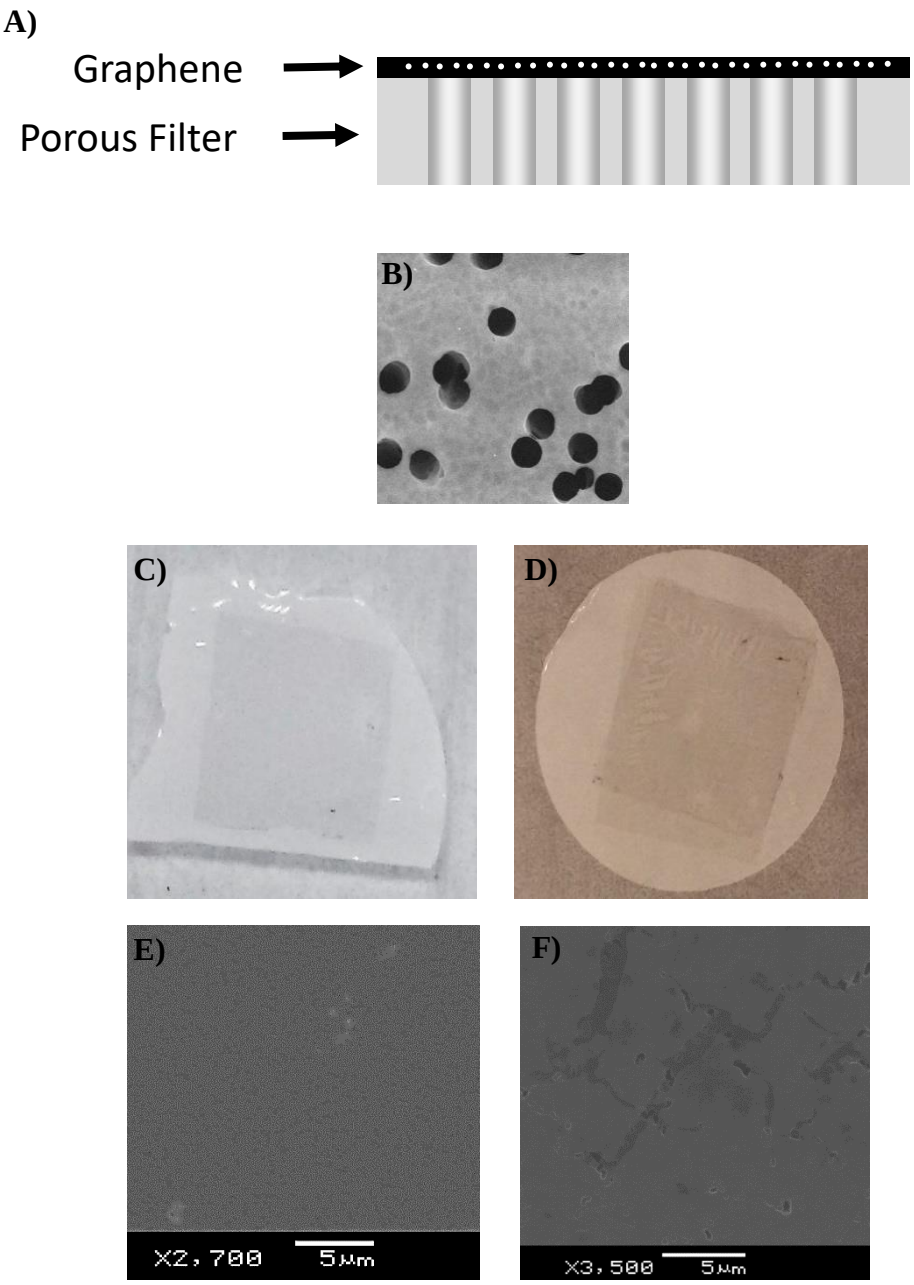

Figure 2-4. A) graphical side-view representation of the composite membrane using commercial filter, B) polycarbonate track etch membrane filters – top-down SEM image from Sterlitech, C&D) top-down photograph of two transfers of single-layer graphene to polycarbonate, E&F) top-down SEM image of graphene coated polycarbonate before (E) and after (F) adding IL

rather than using the plasma to etch holes, the native defects alone were examined as pores to contain the IL.

The area of the exposed membranes was calculated, and an aliquot of dilute IL was added to create a layer approximately 6 μm thick to ensure all defects were thoroughly coated. The gas transport of the composite membranes was 1.54×10^{-9} mol/m² Pa s for CO_2 and 5.44×10^{-11} mol/m² Pa s for N_2, (permeability of 28 and 1 respectively using 6 μm as the thickness) with a selectivity of 29. This selectivity was slightly higher than the selectivity of 23 reported for a traditional SILM of [emim][Tf_2N].[19] Based on the gas permeance analysis, the IL appeared to block the defective sites and the composite membrane showed early promise. After the ionic liquid addition and gas permeability tests, SEM images were obtained again (**Figure 2-4.F**). Unfortunately, either during the gas pressurization across the membrane or loading of the ionic liquid, large cracks and tears were generated measuring several micrometers in size.

Additional membranes were assembled, but all showed increased damage in the post-test imaging. Gas testing yielded fluctuating permeability values while maintaining relatively consistent selectivity values, due variable coverage of intact graphene and the IL being incorporated into the support in defective areas. Due to the nature of the electron microscopy analysis, it is difficult to examine the same exact regions of the large scale membranes before and after testing. To mitigate any holes prior to moving forward, new strategies were applied to fill potential gaps. Previously, Karnik's group has repaired tears in graphene via interfacial polymerization of nylon to fill any voids.[20] Rather than using nylon, an alternative patch could be generated by creating a secondary layer that is similar in chemical composition.

Recently, mussel inspired biomimetic films have been popular since the auto-polymerization of polydopamine has been found to create a thin conformal coating on a wide variety of substrates through a simple immersion method.[21-22] A ten millimolar tris(hydroxymethyl)aminomethane buffer was created at pH 8.5 for the immersion bath since the reaction proceeds in alkaline conditions.[23] Thickness of the coating is determined by the duration of immersion. In this case, the graphene will float on the surface and only

one side is coated. The best concentration of dopamine was 2 milligrams per milliliter of buffer, and the dopamine coating of graphene was completed immediately following the DI water rinse after removal of the copper catalyst. **Figure 2-5** includes optical microscopy images following dopamine coating. It seems the repair is only successful when a thermal treatment is used to remove the PMMA transfer layer.

In many regards, the it has been shown that the PMMA transfer layer causes more problems than benefits. Therefore, a more sensible alternative would be to use a dual-purpose polymer layer rather than the sacrificial layer of PMMA which is difficult to remove. Instead of functioning solely as a temporary support, if a highly porous or high permeability polymer was used, it could remain on the graphene to act as the final substrate for membrane analysis. This *in situ* creation of a structural support would reduce the number of steps required in the graphene transfer process. By eliminating extra steps, the additional defects can be avoided, and pristine graphene should remain.

Porous polymer films can be created via phase inversion following casting directly onto the graphene while still on the copper catalyst. Morphological control of the polymer porosity can be adjusted by adjusting the ratio of volumes between solvent and nonsolvent in the casting solution.[24] Results can further be tailored through dry or wet phase inversion changing the resultant symmetry of the final membrane.[25] Attempts to create a phase inversion porous PMMA membrane were conducted since it is both frequently used for graphene transfer, and there are previously reported phase diagrams for a variety of ternary and quaternary blends.[26-27] A mixture was selected to yield a membrane with prior reports of high air and water flux.

The quaternary mixture consisted of poly(methyl methacrylate) (PMMA 120,000 g/mol), poly(ethylene oxide) (PEO 20,000 g/mol), tetrahydrofuran, and water in a weight ratio of 18/3/76/3. Preliminary tests were completed on a glass substrate. After casting the blend with a doctor blade, a hexane coagulation bath was used.[26] A cross section of the resulting film was examined by SEM before and after PEO removal by solvent extraction in a 60 °C water bath (**Figure 2-6**). The enhanced porosity upon removal of PEO was

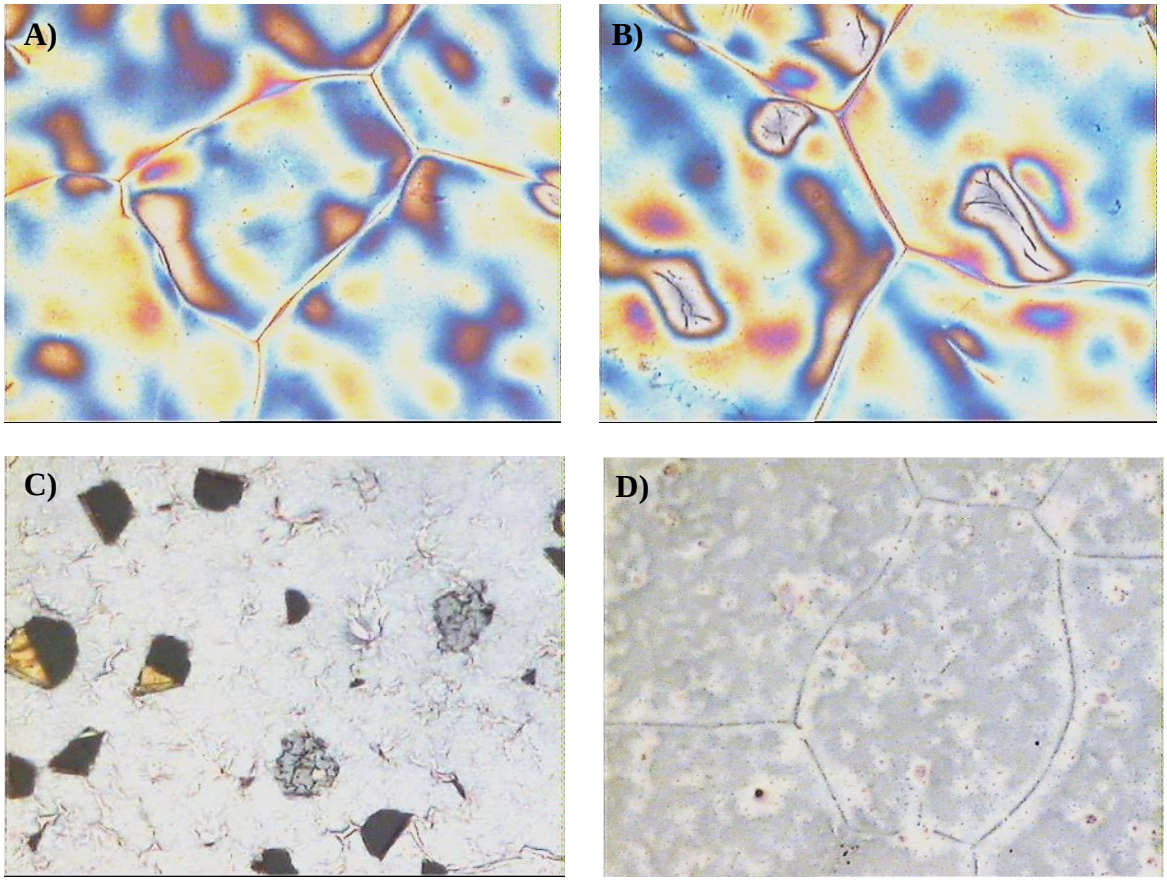

Figure 2-5. Dopamine coated graphene. Images captured from optical microscope camera using 20x objective. A&B) showing PMMA coated graphene/dopamine with visible grain boundaries in both images and defects/cracks in the underlying graphene denoted by asterisks, C&D) graphene/dopamine after PMMA removal by solvent (C) or thermal treatment (D)

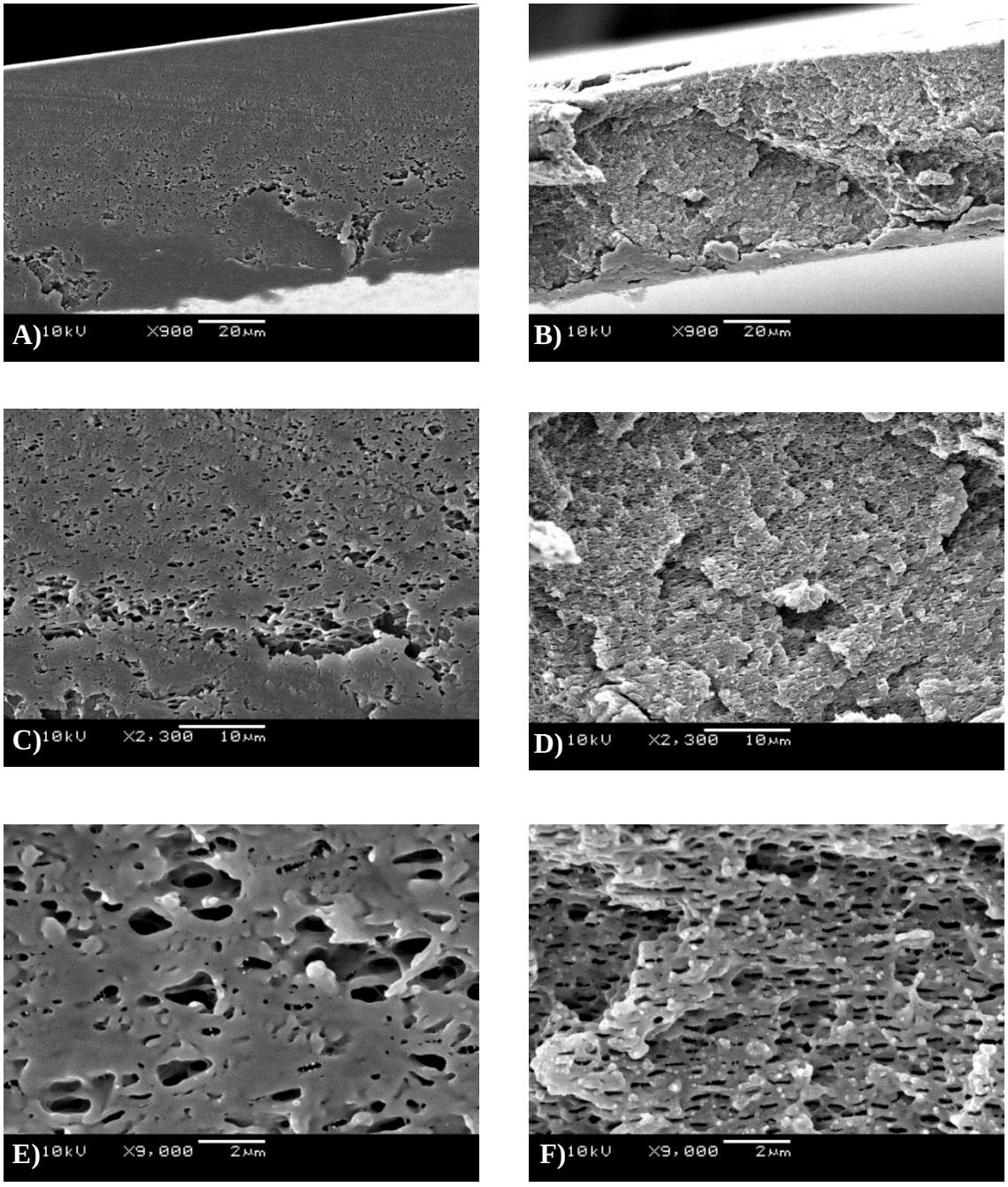

Figure 2-6. SEM cross-section of PMMA-PEO polymer films before (A, C, & E) and after (B, D, & F) solvent extraction

apparent in the SEM, so the polymer film was mounted to an aluminum support for initial permeability testing. Surprisingly the membranes showed very little transport (only about 1 Barrer) lower than some dense polymer films. Different polymers that have high flux will need to be determined before combining with graphene.

2.2.4 Preliminary Conclusions on Ultrathin Membranes

Graphene stability should be excellent based on theoretical calculations,[2] however in practice this is a significant engineering challenge. Through careful tuning of CVD parameters, defect free graphene was synthesized on a copper catalyst. Successful catalyst removal and relatively pristine transfer of graphene has also been achieved from nanoscale to macroscopic regions as large as centimeters. Of the examined porous structural supports, the best graphene quality was attained using polycarbonate track etch membranes.

One of the primary limitations in the current state of the project is achieving precise characterization down to the nanometer scale of test specimens once they are prepared for membrane evaluation. Due to the way in which graphene is supported for membrane testing, it is more difficult to analyze by electron microscopy where the sample must be adhered to the specimen holder. Optical microscopy and Raman spectroscopy allow direct observation of test samples but can only provide limited information on the bulk scale. Because the laser spot size used for Raman microscopy is small, the proof of concept model over a single pinhole will allow for more representative sampling for accurate characterization with respect to the entire membrane. However, at this size the flux is low and more challenging to precisely measure. Continued efforts have been made to reduce the size of the gas chamber to allow for greater sensitivity in future measurements.

2.3 Alternative Strategies to Reduce the Effective Thickness

As an alternative to enhancing the permeability by decreasing the membrane thickness, a different approach was taken from a new direction. Rather than making things ultra-thin on the large scale, the incorporation of numerous microscopic voids into a

macroscopic film allows for a reduction of the "effective" thickness by increasing the amount of empty space enhance the permeability. Some of the highest permeability polymer membranes have an extremely high percentage of intermolecular voids. For example, one of the highest permeability polymers at ~10,000 Barrer is poly(1-trimethylsilyl-1-propyne) (PTMSP) has a fractional free volume of 0.34.[28] However, PTMSP and other glassy polymers with high free volumes are prone to significant degradation due to aging as the polymer chains relax.[29] In addition, polymer swelling on gas adsorption can lead to membrane densification and a reduction in the voids over time. This correlates to overall losses in the gas transport and reduced permeability, reducing the effective lifetime of the membrane system.

Enhancements in the stability must be achieved through thoughtful architecture, much like the development of an open-concept floorplans. While a pure polymer membrane can collapse into its own voids, the incorporation of rigid matrices into the polymer phase could provide structural support to prevent compaction. One collaboration with Jinshui Zhang included the generation of mixed matrix membranes (MMMs) using hollow carbon nanospheres and polystyrene-*block*-poly(ethylene-ran-butylene)-*block*-polystyrene (PS-PEB-PS), a block copolymer (**Figure 2-7**).[30] Upon the addition of hollow carbon spheres, the permeability was increased relative to the pure polymer with the magnitude of enhancement dependent on the loading of spheres. In addition, the selectivity of the MMM showed marginal enhancements from 17 for the block copolymer membrane up to 24 for the 5-30 wt% MMMs (**Figure 2-8**). At greater loadings, the selectivity began decreasing likely due to aggregation of particles and imperfect interfacial coating of the polymer. The integration of hollow spheres can provide free space for fast transport and provide structural support enhanced stability and membrane permeability.

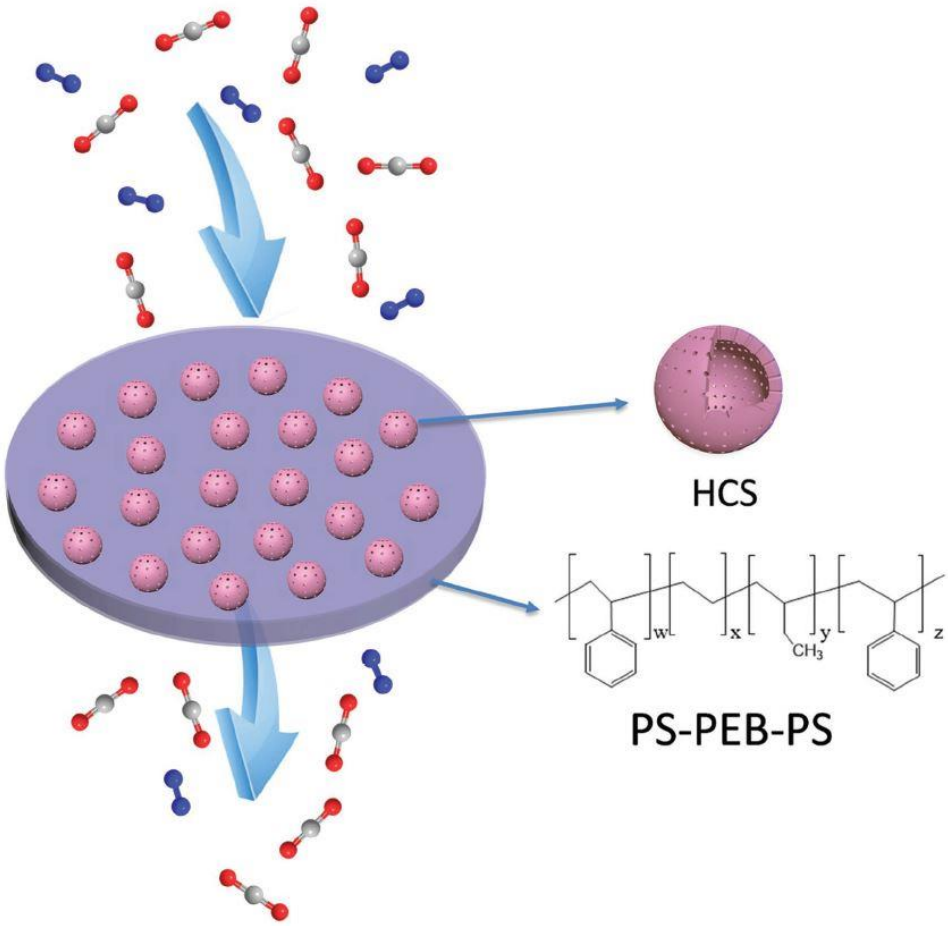

Figure 2-7. Graphic depicting the mixed matrix membrane comprised of hollow carbon spheres (HCS) in block copolymer PS-PEB-PS. Reproduced from reference[30]

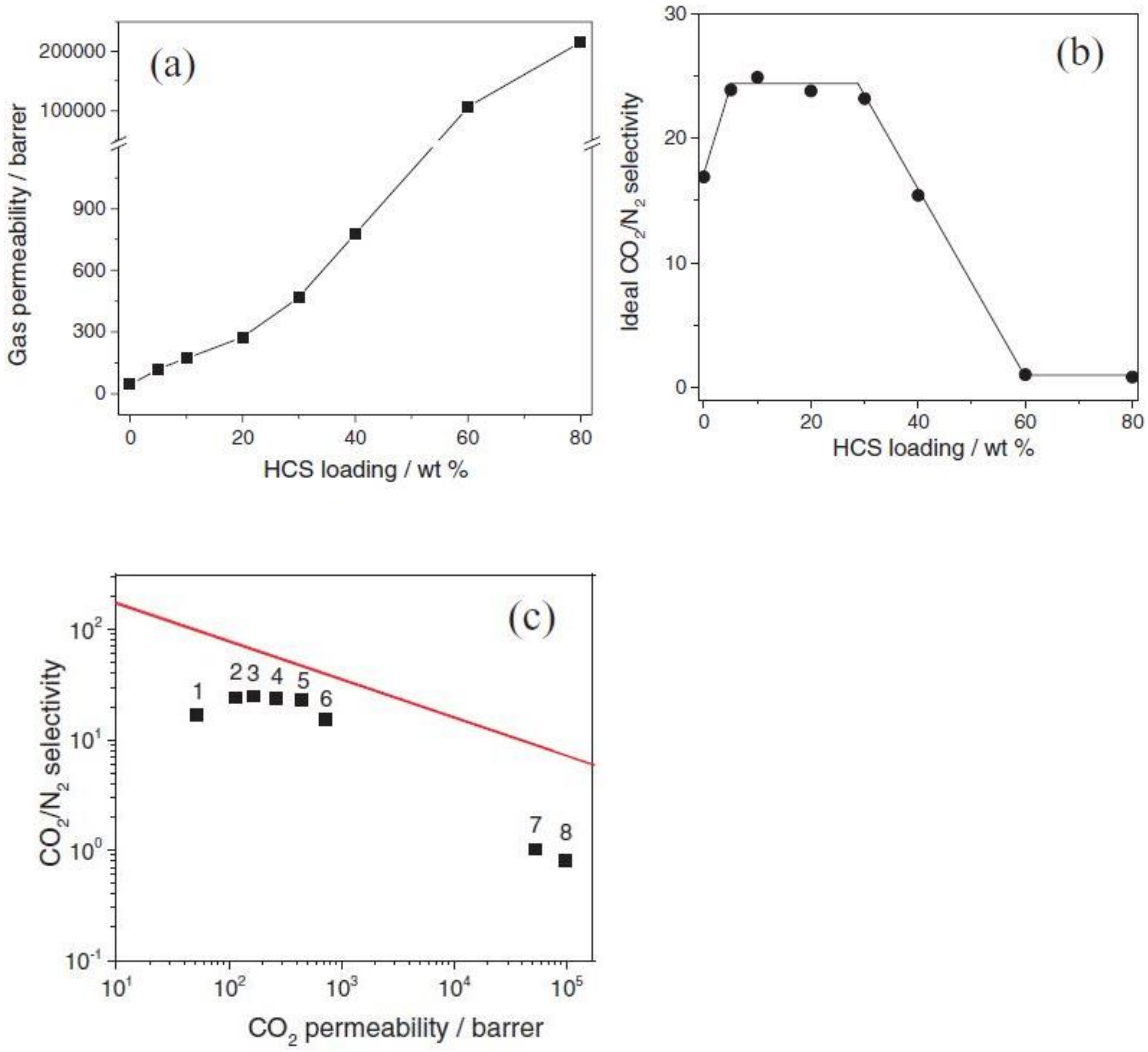

Figure 2-8. a) Gas permeability and b) selectivity as a function of hollow carbon spheres (HCS) loading; c) a Robeson plot for CO_2/N_2 with label 1: the pure block copolymer, and labels 2-8: 5, 10, 20, 30, 40, 60, 80 wt% HCS loadings in the MMM. Reproduced from reference[30]

2.4 From Mixed Matrix Membranes to Porous Liquids

Furthermore, the same strategy that provided enhancements in mixed matrix membranes can be approached in the liquid phase. In 2007, James et al proposed the concept of porous liquids, fluid composites created from porous materials and sterically hindered solvents. In a conventional liquid, as shown by hard spheres in **Figure 2-9**, the free volume is composed entirely from the extrinsic porosity between molecules. Upon addition of porous materials, the fractional free volume can be enhanced when the solvent remains size excluded from the pores. The first type 2 porous liquids were developed simultaneously by the Dai group[31] and Cooper's group[32]. Further background information on porous liquids is provided in the introductions to Chapters 4 & 5. Chapter 4 will focus on the predominately on the solubility characteristics of the porous liquid, while Chapter 5 examines the mechanism of gas sorption through *in situ* FTIR.

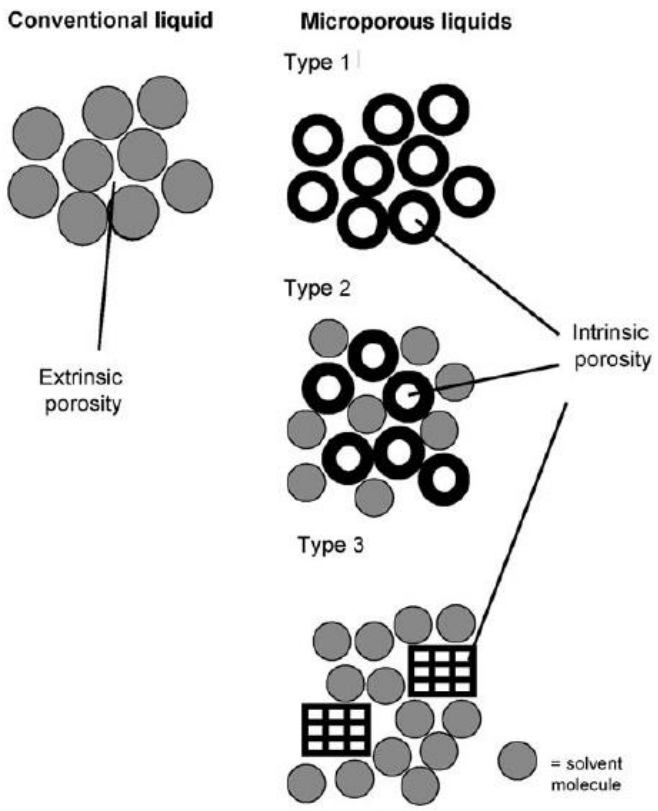

Figure 2-9. Graphic depicting the three main types of porous liquids as defined in the initial concept paper by James et al. Reproduced from reference[33]

2.5 References

1. Bélafi-Bakó, K.; Nemestóthy, N.; Bakonyi, P., Separation of Gases Using Membranes Containing Ionic Liquids. *Ionic Liquids in Separation Technology* **2014**, 261.

2. Jiang, D.-e.; Cooper, V. R.; Dai, S., Porous Graphene as the Ultimate Membrane for Gas Separation. *Nano Lett.* **2009,** *9* (12), 4019-4024.

3. Novoselov, K. S.; Jiang, D.; Schedin, F.; Booth, T. J.; Khotkevich, V. V.; Morozov, S. V.; Geim, A. K., Two-dimensional atomic crystals. *Proceedings of the National Academy of Sciences of the United States of America* **2005,** *102* (30), 10451-10453.

4. Cai, M.; Thorpe, D.; Adamson, D. H.; Schniepp, H. C., Methods of graphite exfoliation. *J. Mater. Chem.* **2012,** *22* (48), 24992-25002.

5. Li, X.; Cai, W.; An, J.; Kim, S.; Nah, J.; Yang, D.; Piner, R.; Velamakanni, A.; Jung, I.; Tutuc, E.; Banerjee, S. K.; Colombo, L.; Ruoff, R. S., Large-Area Synthesis of High-Quality and Uniform Graphene Films on Copper Foils. *Science* **2009,** *324* (5932), 1312-1314.

6. Li, X.; Magnuson, C. W.; Venugopal, A.; An, J.; Suk, J. W.; Han, B.; Borysiak, M.; Cai, W.; Velamakanni, A.; Zhu, Y.; Fu, L.; Vogel, E. M.; Voelkl, E.; Colombo, L.; Ruoff, R. S., Graphene Films with Large Domain Size by a Two-Step Chemical Vapor Deposition Process. *Nano Lett.* **2010,** *10* (11), 4328-4334.

7. Vlassiouk, I.; Regmi, M.; Fulvio, P.; Dai, S.; Datskos, P.; Eres, G.; Smirnov, S., Role of Hydrogen in Chemical Vapor Deposition Growth of Large Single-Crystal Graphene. *ACS Nano* **2011,** *5* (7), 6069-6076.

8. Hao, Y.; Bharathi, M. S.; Wang, L.; Liu, Y.; Chen, H.; Nie, S.; Wang, X.; Chou, H.; Tan, C.; Fallahazad, B.; Ramanarayan, H.; Magnuson, C. W.; Tutuc, E.; Yakobson, B. I.; McCarty, K. F.; Zhang, Y.-W.; Kim, P.; Hone, J.; Colombo, L.; Ruoff, R. S., The Role

of Surface Oxygen in the Growth of Large Single-Crystal Graphene on Copper. *Science* **2013,** *342* (6159), 720-723.

9. Vlassiouk, I.; Fulvio, P.; Meyer, H.; Lavrik, N.; Dai, S.; Datskos, P.; Smirnov, S., Large scale atmospheric pressure chemical vapor deposition of graphene. *Carbon* **2013,** *54*, 58-67.

10. Dhingra, S.; Hsu, J.-F.; Vlassiouk, I.; D'Urso, B., Chemical vapor deposition of graphene on large-domain ultra-flat copper. *Carbon* **2014,** *69*, 188-193.

11. Rao, C. N. R.; Maitra, U.; Matte, H. S. S. R., Synthesis, Characterization, and Selected Properties of Graphene. In *Graphene*, Wiley-VCH Verlag GmbH & Co. KGaA: 2012; pp 1-47.

12. Ferrari, A. C.; Meyer, J. C.; Scardaci, V.; Casiraghi, C.; Lazzeri, M.; Mauri, F.; Piscanec, S.; Jiang, D.; Novoselov, K. S.; Roth, S.; Geim, A. K., Raman Spectrum of Graphene and Graphene Layers. *Phys. Rev. Lett.* **2006,** *97* (18), 187401.

13. O'Hern, S. C.; Stewart, C. A.; Boutilier, M. S. H.; Idrobo, J.-C.; Bhaviripudi, S.; Das, S. K.; Kong, J.; Laoui, T.; Atieh, M.; Karnik, R., Selective Molecular Transport through Intrinsic Defects in a Single Layer of CVD Graphene. *ACS Nano* **2012,** *6* (11), 10130-10138.

14. Kim, K. S.; Zhao, Y.; Jang, H.; Lee, S. Y.; Kim, J. M.; Kim, K. S.; Ahn, J.-H.; Kim, P.; Choi, J.-Y.; Hong, B. H., Large-scale pattern growth of graphene films for stretchable transparent electrodes. *Nature* **2009,** *457* (7230), 706-710.

15. Song, J.; Kam, F.-Y.; Png, R.-Q.; Seah, W.-L.; Zhuo, J.-M.; Lim, G.-K.; Ho, P. K. H.; Chua, L.-L., A general method for transferring graphene onto soft surfaces. *Nat Nano* **2013,** *8* (5), 356-362.

16. Joshua, D. W.; Gregory, P. D.; Enrique, A. C.; Justin, C. K.; Joshua, A. K.; Isha, D.; Ashkan, B.; Jayan, H.; Basil, A.; Yaofeng, C.; Hefei, D.; Richard, T. H.; Joseph, W.

L.; Eric, P., Annealing free, clean graphene transfer using alternative polymer scaffolds. *Nanotechnology* **2015,** *26* (5), 055302.

17. Boutilier, M. S. H.; Sun, C.; O'Hern, S. C.; Au, H.; Hadjiconstantinou, N. G.; Karnik, R., Implications of Permeation through Intrinsic Defects in Graphene on the Design of Defect-Tolerant Membranes for Gas Separation. *ACS Nano* **2014,** *8* (1), 841-849.

18. Surwade, S. P.; Smirnov, S. N.; Vlassiouk, I. V.; Unocic, R. R.; Veith, G. M.; Dai, S.; Mahurin, S. M., Water desalination using nanoporous single-layer graphene. *Nat Nano* **2015,** *10* (5), 459-464.

19. Scovazzo, P., Determination of the upper limits, benchmarks, and critical properties for gas separations using stabilized room temperature ionic liquid membranes (SILMs) for the purpose of guiding future research. *J. Membr. Sci.* **2009,** *343* (1–2), 199-211.

20. O'Hern, S. C.; Jang, D.; Bose, S.; Idrobo, J.-C.; Song, Y.; Laoui, T.; Kong, J.; Karnik, R., Nanofiltration across Defect-Sealed Nanoporous Monolayer Graphene. *Nano Lett.* **2015,** *15* (5), 3254-3260.

21. Barrett, D. G.; Sileika, T. S.; Messersmith, P. B., Molecular diversity in phenolic and polyphenolic precursors of tannin-inspired nanocoatings. *Chem. Commun.* **2014,** *50* (55), 7265-7268.

22. Cheng, C.; Li, S.; Zhao, J.; Li, X.; Liu, Z.; Ma, L.; Zhang, X.; Sun, S.; Zhao, C., Biomimetic assembly of polydopamine-layer on graphene: Mechanisms, versatile 2D and 3D architectures and pollutant disposal. *Chem. Eng. J.* **2013,** *228*, 468-481.

23. Lee, H.; Dellatore, S. M.; Miller, W. M.; Messersmith, P. B., Mussel-Inspired Surface Chemistry for Multifunctional Coatings. *Science* **2007,** *318* (5849), 426-430.

24. Lin, K.-Y.; Wang, D.-M.; Lai, J.-Y., Nonsolvent-Induced Gelation and Its Effect on Membrane Morphology. *Macromolecules* **2002,** *35* (17), 6697-6706.

25. Pinnau, I.; Koros, W. J., Structures and gas separation properties of asymmetric polysulfone membranes made by dry, wet, and dry/wet phase inversion. *J. Appl. Polym. Sci.* **1991,** *43* (8), 1491-1502.

26. Schuhmacher, E.; Soldi, V.; Nunes Pires, A. T., PMMA or PEO in THF/H2O mixture: phase diagram, separation mechanism and application. *J. Membr. Sci.* **2001,** *184* (2), 187-196.

27. Cheng, L.-P.; Shaw, H.-Y., Phase behavior of a water/2-propanol/poly(methyl methacrylate) cosolvent system. *J. Polym. Sci., Part B: Polym. Phys.* **2000,** *38* (5), 747-754.

28. Freeman, B.; Yampolskii, Y.; Pinnau, I., *Materials Science of Membranes for Gas and Vapor Separation*. John Wiley & Sons: 2006.

29. Lau, C. H.; Nguyen, P. T.; Hill, M. R.; Thornton, A. W.; Konstas, K.; Doherty, C. M.; Mulder, R. J.; Bourgeois, L.; Liu, A. C. Y.; Sprouster, D. J.; Sullivan, J. P.; Bastow, T. J.; Hill, A. J.; Gin, D. L.; Noble, R. D., Ending Aging in Super Glassy Polymer Membranes. *Angew. Chem. Int. Ed.* **2014,** *53* (21), 5322-5326.

30. Zhang, J.; Schott, J. A.; Li, Y.; Zhan, W.; Mahurin, S. M.; Nelson, K.; Sun, X.-G.; Paranthaman, M. P.; Dai, S., Membrane-Based Gas Separation Accelerated by Hollow Nanosphere Architectures. *Adv. Mater.* **2017,** *29* (4), 1603797.

31. Zhang, J.; Chai, S.-H.; Qiao, Z.-A.; Mahurin, S. M.; Chen, J.; Fang, Y.; Wan, S.; Nelson, K.; Zhang, P.; Dai, S., Porous Liquids: A Promising Class of Media for Gas Separation. *Angew. Chem. Int. Ed.* **2015,** *54* (3), 932-936.

32. Giri, N.; Del Pópolo, M. G.; Melaugh, G.; Greenaway, R. L.; Rätzke, K.; Koschine, T.; Pison, L.; Gomes, M. F. C.; Cooper, A. I.; James, S. L., Liquids with permanent porosity. *Nature* **2015,** *527*, 216.

33. O'Reilly, N.; Giri, N.; James, S. L., Porous Liquids. *Chemistry – A European Journal* **2007,** *13* (11), 3020-3025.

CHAPTER 3. SUPPORTED BICYCLIC AMIDINE IONIC LIQUIDS AS A POTENTIAL CO_2/N_2 SEPARATION MEDIUM

3.1 Publication Statement

A version of this chapter was originally published by Jennifer A. Schott, Chi-Linh Do-Thanh, Shannon M. Mahurin, Ziqi Tian, Nicole C. Onishi, De-en Jiang, and Sheng Dai in the *Journal of Membrane Science*:

Schott, J. A.; Do-Thanh, C. L.; Mahurin, S. M.; Tian, Z.; Onishi, N. C.; Jiang, D. E.; Dai, S., Supported Bicyclic Amidine Ionic Liquids as a Potential CO_2/N_2 Separation Medium. *J.Membr. Sci.* **2018,** *565*, 203-212.

Jennifer A. Schott provided the primary authorship and contributions to this paper. The experiments, except for those listed below, and data analysis were completed by the author. She completed the physical and chemical characterization of the ionic liquids (ILs), CO_2 solubility measurements, membrane preparation, membrane testing, associated calculations, and wrote the paper. Co-author contributions are as follows: Chi-Linh Do-Thanh synthesized ILs; Ziqi Tian, Nicole C. Onishi, and De-en Jiang completed the COSMOtherm calculations; Shannon M. Mahurin and Sheng Dai discussed the results and edited the manuscript.

3.2 Abstract

Five new room temperature ionic liquids were tested as supported ionic liquid membranes (SILMs) for CO_2/N_2 separation capability. This series of ionic liquids (ILs) contains bicyclic amidine cations of 1,8-diazabicyclo[5.4.0]undec-7-ene (DBU) or 1,5-diazabicyclo[4.3.0]non-5-ene (DBN) with small alkyl chain substituents. These ILs have been synthesized to examine the effects of cation structure on free volume. Relevant physical and chemical properties have been examined, including CO_2 solubility and viscosity. The relationship between fractional free volume and permeability of gases is explored, with an interesting note on solubility. Each cation was paired with two different anions: bis(trifluoromethanesulfonyl)imide and tetracyanoborate, for further investigation

of the cation-anion interaction on SILM permeability and selectivity. Three of these new ILs have exceeded Robeson's upper bound for CO_2/N_2 gas separations.

3.3 Introduction

With the continued rise in atmospheric CO_2 levels and the potential impact on climate, carbon capture and storage (CCS) has gained prominence as a potential technological solution to curb CO_2 emissions, resulting in increased interest in advanced materials to facilitate the extraction of CO_2 from energy-related emissions.[1] However, the eventual commercialization and more widespread implementation of CCS requires a higher efficiency than current techniques can provide.[2] To that end, a variety of new sorbent and membrane materials have been explored for CO_2 separation including metal organic frameworks (MOFs), covalent organic frameworks (COFs), porous carbons, and ionic liquids.[3]

Ionic liquids (ILs) are a class of polar organic salts with melting points near or below room temperature. Due to their ease of functionalization, negligible vapor pressure, as well as high thermal and chemical stability, ILs have been exploited as a replacement for typical solvents[4] and a variety of other uses in developing green technologies.[5] The most prevalent ILs reported in the literature are the salts of imidazolium-based cations,[6-9] but a variety of other room temperature ionic liquids (RTILs) have also been examined, including derivatives of pyridinium, guanidinium, and phosphonium, among others.[10-11]

While RTILs have been proposed as a replacement solvent, application in gas separations can be difficult due to cost and limitations from increased viscosity over traditional organic solvents. Therefore, one approach is incorporating the ionic liquids into porous supports to create supported ionic liquid membranes (SILMs). By immobilizing the ILs in a structural support, limitations like slow mass transfer can be mitigated. In addition, membranes offer the potential for improved energy efficiency compared to adsorbents.[12] SILMs using a variety of ionic liquids and structural supports have been investigated and reviewed.[8-9]

Due to the vast variety of ionic liquids, the relative importance of the anion versus the cation in CO_2 separations has been the subject of much analysis. Through systematic variations of IL composition, previous research suggests that the anion plays an important role in determining gas solubility.[13-14] It is generally accepted that fluorinated anions are desirable due to their enhanced CO_2 solubility,[15] and a survey of the literature shows frequent use of the bis(trifluoromethylsulfonyl)imide (Tf_2N) anion. More recent work, however, has shown that cyano-functionalized ILs,[16] including the tetracyanoborate [$B(CN)_4$] anion,[17-18] can meet or exceed the upper bound due to increased CO_2 interactions and decreased cation–anion interactions. Additional computational and experimental research on cyano-based ions followed these initial reports looking at the anions and mixtures.[19-21] Further investigation has focused on the dynamics between carbon dioxide and the ionic liquid including an analysis of the cation effect, binding energy, free volume, viscosity, and diffusivity.[22-23] Weaker electrostatic interactions between the anion and cation lead to higher gas solubility, as in some pyridinium tetracyanoborate ILs.[24] Some of the best ionic liquids for gas separations are those where ion interactions are minimal. These ion interactions are intrinsically linked to the spacing between ion pairs, and larger internal distances create a greater free volume. Studies have also shown that higher free volumes in ILs due to delocalized anions lead to greater selectivity.[25] When the intramolecular forces within the IL are reduced, the intermolecular interactions between IL and CO_2 can be increased. Therefore, we will explore the changes in solubility and permeability in relation to this variation.

While anion properties have been at the forefront of most discussion, in this work, we investigate the effects of cation structure on carbon dioxide sorption and separation. Much of the previous work on cation variation has simply focused on functionalization of well-known structures such as imidazolium. However, we used a larger cyclic skeleton as a potential way to impart additional free volume of the IL while minimizing interpenetration into other parts of the IL. In this case, derivatives of two bulky bicyclic amidines, 1,8-diazabicyclo[5.4.0]undec-7-ene (DBU) and 1,5-diazabicyclo[4.3.0]non-5-ene (DBN), were selected for study. While most commonly seen as catalysts for organic

reactions, both DBU and DBN are considered superbases. Basic compounds with amino functionality, including amidines and guanidines, are typically highly valued for CO_2 solubility. Jessop noted the interesting relationship between DBU and CO_2 used as a switchable solvent,[26] and others have examined carbon dioxide binding organic liquids.[27] Superbases have been used previously to derive protic ILs[28-29] or as additives[30-31] to increase the capacity of traditional ILs.

Herein, new *N*-alkyl-substituted amidine ionic liquids were synthesized to explore their application in supported ionic liquid membranes for gas separation. There have been only few reports[32-35] of bicyclic ILs, and none of those use DBU or DBN based ionic liquids for CO_2 separations. In this work, we have measured both the physical properties and gas separations of DBU- and DBN-based ionic liquids in order to gain further insight into the effects of the bulky cation structure, substituent, and anion on the intra- and intermolecular interactions, all of which play a role in the solubility of CO_2.

3.4 Experimental

3.4.1 Materials and Ionic Liquid Synthesis

Solvents, reagents, and chemicals were purchased from commercial vendors and used without further purification. A detailed account of the synthetic protocol is provided in the supporting information. (**Figure 3-9**) Generally, ice-chilled solutions of DBU and DBN were alkylated using the corresponding alkyl iodides to form the precursor salts. Subsequent anion metathesis with solutions of lithium bis(trifluoromethanesulfonyl)imide or potassium tetracyanoborate produced the respective ionic liquids. The cation and anion structures for these eight bicyclic ILs are shown in **Figure 3-1**. ^{1}H and ^{13}C NMR spectra of the ILs were recorded at ambient temperature on a Varian VNMRS 500 MHz narrow-bore broadband system, and ^{11}B NMR spectra were recorded at ambient temperature on a Bruker Avance 400 MHz wide-bore spectrometer. ^{1}H and ^{13}C NMR chemical shifts were referenced to the residual solvent, and ^{11}B NMR chemical shifts were referenced to external

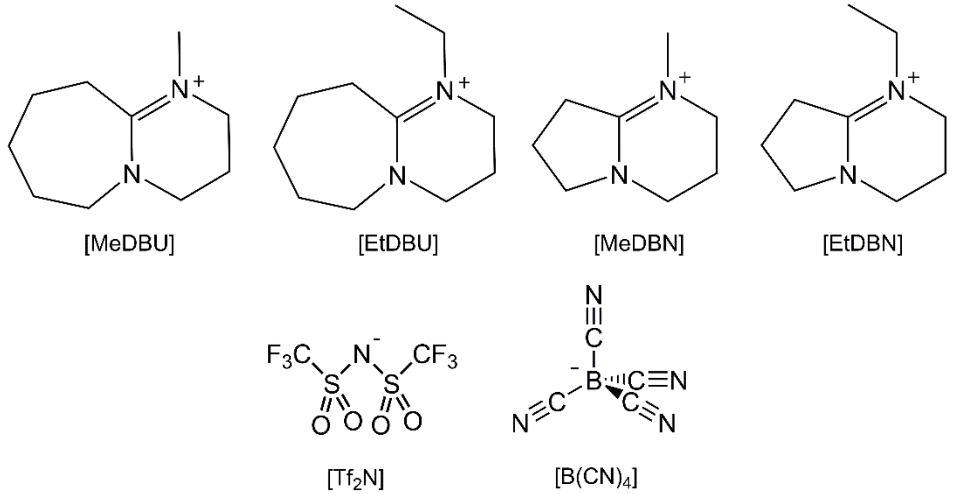

Figure 3-1. Structures and abbreviations of the bicyclic ionic liquid cations and anions

BF_3•Et_2O. Mass spectrometry analyses were performed using a QSTAR Elite quadrupole time-of-flight (QTOF) mass spectrometer with an electrospray ionization source from AB Sciex (Concord, Ontario, Canada).

3.4.2 COSMOtherm Calculations

The COSMO-RS (Conductor-like Screening Model for Real Solvents) method developed by Klamt and coworkers[36-37] was applied to predict the thermodynamic properties of our synthesized ILs for CO_2 capture. Various ILs were considered as equimolar mixtures of cations and anions. The geometry of each ion was first optimized with Turbomole software package[38-39] at the BP86/TZVP level.[40-41] Then the COSMO files were generated from the Turbomole program for ions which were used as the inputs for the COSMOthermX code (Version C3.0-16.01).[42] Statistical thermodynamic calculations were performed to estimate density, fractional free volume (FFV), and CO_2 solubility in each ionic liquid. This process has been validated to predict thermodynamic properties of ILs and gas solubility in solvent.[43-44]

3.4.3 Characterization Methods

Infrared spectra of the four iodide precursors and eight ionic liquids were obtained using a Perkin Elmer Frontier FTIR with attenuated total reflectance set to 2 cm^{-1} resolution, using sixteen scans from 650-4000 cm^{-1}.

Thermal properties were determined via differential scanning calorimetry (DSC) and thermal gravimetric analysis (TGA). Decomposition temperatures were determined under nitrogen flow using a TA Instruments TGA Q50 with heating at a ramp rate of ten degrees per minute up to 750 °C in a platinum pan. Any glass, melting, or crystallization transitions of the ionic liquids were found via two consecutive heating-cooling cycles from -90 °C to 100 °C using a ten degree per minute heating rate on a TA Instruments Q100 DSC. Measurements were completed using hermetically sealed aluminum pans with an

empty aluminum pan as reference. The TA Universal Analysis software was used to determine the onset point of any transitions.

Viscosity measurements were obtained using a Brookfield DVII+ Pro cone-plate viscometer. Prior to measurement, certified viscosity reference standards were analyzed to check performance from 10-1000 centipoise. Approximately 0.75 mL of RTIL was used for the analysis and a recirculating water jacket was used for temperature control with a minimum equilibration of fifteen minutes at each temperature. To ensure accurate readings, the spindle was allowed a minimum of five rotations prior to each measurement.

Isothermal CO_2 absorption measurements were recorded using a Hiden Isochema Intelligent Gravimetric Analyzer. Each sample, approximately 80 milligrams, was heated for a minimum of seven hours at 70 °C under vacuum (4-6 millibar) until reaching a stable weight where the dry mass was recorded. During analysis, a recirculating water bath was used to maintain a constant sample temperature. The uptakes, corrected for buoyancy, were measured as a function of pressure up to 10 atmospheres (atm).

3.4.4 Membrane Preparation and Gas Permeation Measurements

The SILMs were prepared by thoroughly immersing the porous polyethersulfone supports (Supor-100, Pall), pore size 100 nanometers, in approximately one milliliter of IL and placed in a vacuum oven at 40 °C overnight to degas and ensure all pores were filled. The loaded membrane was removed from the excess solution and surface was wiped gently with a lint-free tissue.

To experimentally determine the permeability of the SILMs, a custom built testing apparatus was used to record the single gas permeation measurements.[16] The test chamber is configured with the membrane separating the gaseous feed cell from the permeate cell. Prior to analysis, membranes were inserted into the sample chamber and placed under vacuum to outgas and equilibrate. To minimize any fluctuations in the feed pressure, a ballast with a large volume was maintained on the upstream side of the sample cell. For the results presented here, a single gas was applied on the feed side of the cell and a

Baratron pressure transducer on the downstream side of the membrane recorded the change in permeate pressure over time, which is the amount of gas flux through the membrane.

The permeability of a membrane is a quantification of the analytes ability to pass through the membrane medium, and is calculated using the gas flux through a specific membrane thickness over a certain pressure drop. The permeability of dense polyethersulfone films is minimal, only around 3 Barrer for CO_2.[45-47] Therefore, in the SILMs presented, the preferential mode of transport is through the ionic liquid phase. Similar to polymeric membranes, supported ionic liquid membranes operate on a solution-diffusion mechanism where the gas is first adsorbed into the membrane, diffuses through the bulk according to a concentration gradient, and desorbs on the downstream side.[48] Therefore, the permeability takes into account both the solubility of the analyte in the medium as well as the diffusivity of the gaseous analyte through the membrane.

$$P = \frac{\tau}{\phi} \frac{Vl}{RTA(P' - P'')} \frac{dP''}{dt}$$

The permeability (P) is determined as shown above, where τ is the tortuosity, ϕ is the porosity, V is the volume of the permeate, l is the membrane thickness, R is the gas constant, T is the temperature, A is the area of the membrane, P' is the feed pressure, and P'' is the pressure of the permeate.

$$\alpha_{x/y} = \frac{P_x}{P_y}$$

The selectivity (α) represented here is defined as the ratio of permeabilities of the more permeable species (x) versus the less permeable species (y) also known as the permselectivity.

3.5 Results

3.5.1 Structural and Physical Properties

To confirm the structure of the bicyclic ILs, the infrared spectra are presented in **Figure 3-2** with a standard offset for clarity. A distinctive feature that helps identify the

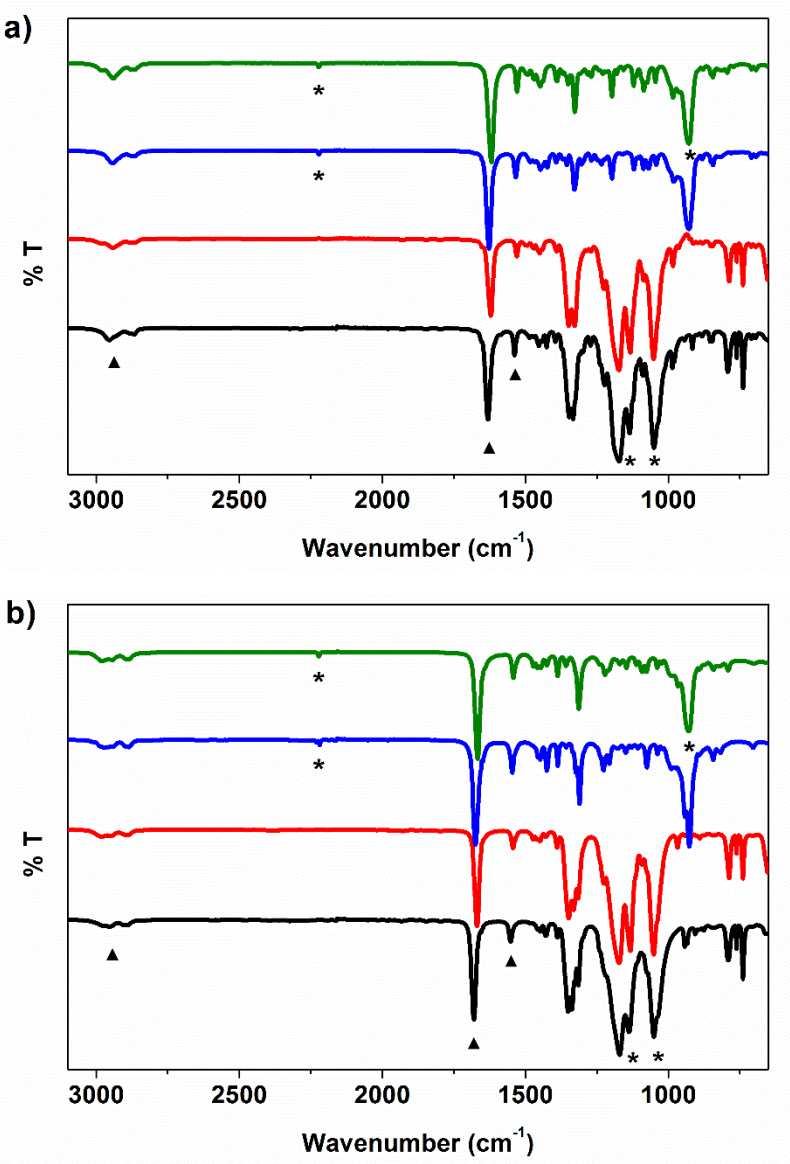

Figure 3-2. FTIR for a) DBU and b) DBN based ILs including labels for some distinctive ▲ cation and * anion features. From top to bottom [Et-][B(CN)$_4$] green, [Me-][B(CN)$_4$] blue, [Et-][Tf$_2$N] red, and [Me-][Tf$_2$N] black.

cation are the set of bands representing the *N,N*-disubstituted amidine. The first band corresponds to the imine C=N stretch in the amidine and appears with strong intensity near 1630 cm^{-1} for DBU ILs versus 1670 cm^{-1} for DBN ILs, a notable difference between the two derivatives.[49] The second band in this set is a medium intensity peak located from 1550–1530 cm^{-1} with variability in position depending on the bicyclic structure and substituent. Also, the peaks in the range ~2850–3000 cm^{-1} represent CH stretching modes which allows for another characteristic fingerprint of the cation. A recent review provides a comprehensive discussion of spectroscopic properties for common ILs, including IR spectra for both anions used here, and confirms the observations from our spectra.[50] For example, the presence of a small peak near 2218 cm^{-1} in the tetracyanoborate ILs is indicative of the nitrile CN asymmetric stretch. There is also a strong peak around 927 cm^{-1} which shows the B–C stretching. As for those with the bis(trifluoromethanesulfonyl)imide anion, the peaks around 1053, 1134, 1176, and 739/788 cm^{-1} are in agreement with those attributed to the cis/trans conformers of $[Tf_2N]$.[51-52] Vibrational spectroscopy allows for further identification of important features of the new ILs. The vibrational modes observed in the IR spectra agree with previous reports and confirm the composition of the ILs.

Decomposition temperatures of the DBU and DBN ILs were determined via thermal gravimetric analysis and are reported in **Table 3-1** along with percent decomposition. The TGA traces for the iodide precursors are given in supporting information (**Figure 3-10)** while the ILs are shown in **Figure 3-3**. Onset temperatures for their degradation range from 379 to 420 °C for $[Tf_2N]$ and 403 to 420 °C for $[B(CN)_4]$, higher than many ammonium and imidazolium ILs.[53] Similar DBU-based thiocyanate substituted triazolium cations which had lower decomposition temperatures than their alkyl triazolium precursors,[54] the bicyclic ionic liquids in this study display excellent thermal stability which could be important in gas separation applications. In this study, the $[Tf_2N]$ derived ILs show complete decomposition, while those with the $[B(CN)_4]$ anion contain crosslinkable nitrile groups which account for the 12–24% residual carbon yield.[55-56]

Table 3-1. Physical properties of bicyclic ILs: glass transition (T_g), solid-solid transition ($T_{s\text{-}s}$), melting transition (T_m), decomposition temperature (T_d), percent decomposition ($\%_d$), viscosity (η), and activation energy for viscous flow (E_a)

	T_g (°C)	$T_{s\text{-}s}$ (°C)	T_m (°C)	T_d (°C)	$\%_d$	η (cP)	E_a (kJ/mol)
[MeDBU][Tf_2N]		-17.3	45.9	420.5	99.3	–	–
[MeDBU][$B(CN)_4$]	-71.9			409.4	76.4	58.9	31.6
[EtDBU][Tf_2N]			17.9	418.5	99.3	167.3	37.2
[EtDBU][$B(CN)_4$]	-68.5			419.5	77.3	81.2	35.1
[MeDBN][Tf_2N]		-55.2, -3.1	98.6	404.8	99.9	–	–
[MeDBN][$B(CN)_4$]		-68.7	65.6	403.2	81.7	–	–
[EtDBN][Tf_2N]		-79.1, -8.9, 9.5	23.4	407.8	99.2	74.0	30.8
[EtDBN][$B(CN)_4$]		-44.5	21.1	410.7	88.2	29.7	26.6

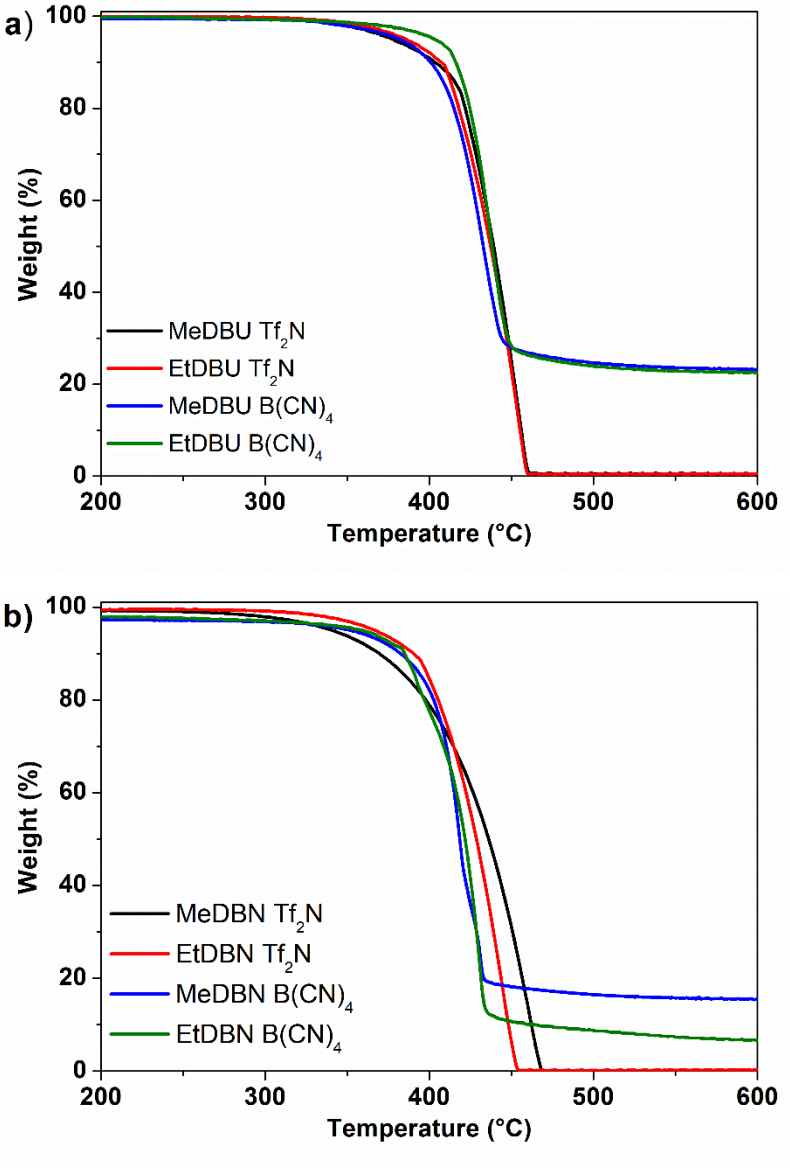

Figure 3-3. TGA traces for a) DBU and b) DBN based ILs. [Me-][Tf_2N] black, [Et-][Tf_2N] red, [Me-][$B(CN)_4$] blue, [Et-][$B(CN)_4$] green

The thermal properties of the eight ionic liquids were examined by differential scanning calorimetry, and the DSC curves for the bulk IL samples are shown in supporting information. (**Figure 3-11**) The corresponding glass or liquid transitions for the bulk ILs are listed in **Table 3-1** and follow the trend: [MeDBU][$B(CN)_4$] < [EtDBU][$B(CN)_4$] < [EtDBN][$B(CN)_4$] < [EtDBN][Tf_2N] < [EtDBU][Tf_2N] < [MeDBU][Tf_2N] < [MeDBN][$B(CN)_4$] < [MeDBN][Tf_2N]. Reports of other ionic liquids have presented thermal profiles which include various combinations of glass, melting, and crystallization transitions.[57] Two types of thermal profiles are seen here, the first exhibiting only a glass transition, while the rest display both endothermic peaks on heating and exothermic peaks on cooling, distinctive of fusion and crystallization respectively. The presence of multiple endothermic transitions are attributed to the polymorphism of the IL, and has been previously reported for ILs containing the [Tf_2N] anion, as it exhibits a transition in the conformers of the ions.[58] A recent paper shows the presence of multiple solid-solid transitions for an analogous [Tf_2N] IL.[59] For this study, the ILs with [Tf_2N] anions have a higher melting point than those with [$B(CN)_4$].

3.5.2 Viscosity

The viscosities of the bicyclic ionic liquids were initially measured at 25 °C and range from approximately 30 to 167 cP increasing from [EtDBN][$B(CN)_4$] to [EtDBU][Tf_2N] respectively, as shown in **Table 3-1**. For common imidazolium-based ILs, many physical properties, such as the viscosity of 1-ethyl-3-methylimidazolium, [emim], [Tf_2N] at 27 cP, are well known. Not surprisingly, there is a significant increase in viscosity when changing from this smaller monocyclic imidazolium to either of the larger bicyclic cations, i.e., the additional ring resulted in a substantial increase in viscosity. Moreover, altering the structure from DBN to DBU, by switching the size of the added ring from five- to seven-members respectively, can have drastic effects. This slight difference between the two bicyclic structures accounts for a significant change in viscosity, such as [EtDBN][Tf_2N] at 74 cP and [EtDBU][Tf_2N] at 167 cP. The five-membered ring in DBN

contributes to having a much lower viscosity, amounting to only 36–44% of its seven-membered ring DBU counterparts. The greater fluidity of the DBN ILs compared to the DBU ILs is one of the most notable differences between the physical properties imparted by these two cations.

Meaningful comparisons to other data available in the literature can be somewhat limited due to the prevalence of non-standard "room temperature" measurements, which can span a range of temperatures more than five degrees Celsius. This large range of temperatures in conjunction with the exponential decay relationship between viscosity and temperature limits the comparability of values. Regardless, previous reports have also shown a significant alteration of viscosity at a constant temperature upon changing the anion.[16] For example, Lethesh[34] reports an ethyl-DBU dicyanamide ionic liquid, the same cation as in this work but a different anion, with viscosity of 168 cP at 20 °C, which seems to fit between the viscosity of [EtDBU][Tf_2N] and [EtDBU][$B(CN)_4$] reported here. From the 25 °C viscosity data collected here, switching the anion from [Tf_2N] to [$B(CN)_4$] results in a reduction in the viscosity by approximately one half. This was previously observed in imidazolium-based ILs where the [$B(CN)_4$] anion exhibited a lower viscosity than the [Tf_2N] congener.[18]

In addition to the measurements at 25 °C, additional data was collected at increasing temperature up to 60 °C. As expected, all ILs show decreasing viscosity upon increasing temperature, and the curves for all five room temperature ionic liquids are presented in **Figure 3-4a**. These temperature dependent viscosity measurements can also be analyzed using the Arrhenius equation to elucidate additional information about the interactions in the ionic liquids. Using this information, the activation energy for viscous flow (E_a) can be determined from the linear regression represented by

$$\ln(\eta) = \left(\frac{E_a}{R}\right)\frac{1}{T} + lnA$$

where η is viscosity, R is the gas constant, T is the temperature in Kelvin, and A is the pre-exponential factor. The linear relationship of the data in **Figure 3-4b** is indicative that the

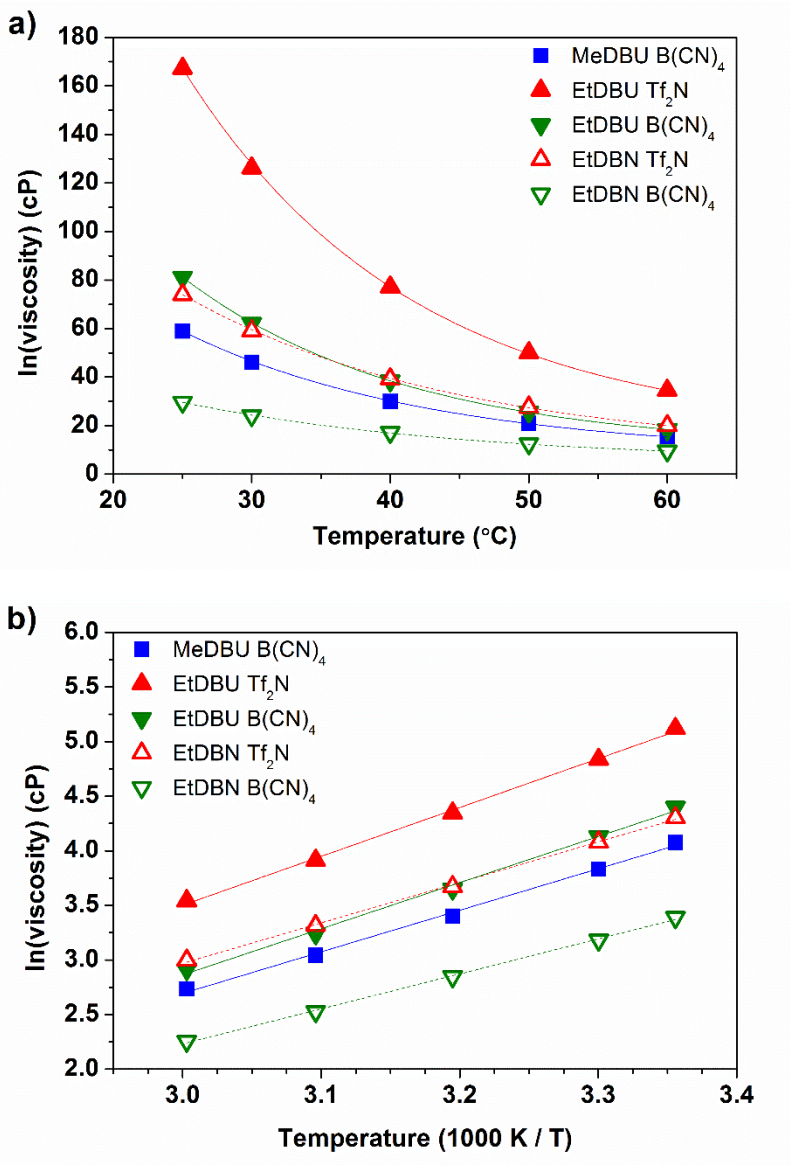

Figure 3-4. a) Temperature dependent viscosity measurements for the RTILs, and b) corresponding Arrhenius plots

ILs follow Arrhenius behavior. The corresponding lines represent the best fit of the temperature-dependent viscosity from which the activation energies for viscous flow are determined.

3.5.3 CO_2 Solubility

Carbon dioxide solubility measurements were completed using isothermal CO_2 absorption at pressures up to 10 atm at both 25 °C and 40 °C for the bicyclic ILs. Results for the room temperature ILs are shown in **Figure 3-5**, no data is shown for those that are solids due to negligible uptake. The ILs in order of increasing carbon dioxide molar uptake are [EtDBU][Tf_2N] < [EtDBN][Tf_2N] < [EtDBU][$B(CN)_4$] < [MeDBU][$B(CN)_4$] < [EtDBN][$B(CN)_4$], with all solubility values tabulated in **Table 3-2**. The experimental values determined from the gravimetric uptake are lower than those predicted by the COSMOtherm model, which has been seen in the past for tetracyanoborate ILs,[18] however, the general trends in the calculated solubility are quite similar. The bicyclic ionic liquids with [Tf_2N] anion showed slightly lower carbon dioxide solubility, at 0.074 and 0.085 mol L^{-1} atm^{-1}, than their analogous imidazolium counterparts like [emim][Tf_2N] at 0.103 mol L^{-1} atm^{-1}. These solubility values are more similar to the triazolium and benzyl functionalized ILs our group has explored previously.[54] However, solubility values for bicyclic ILs with the [$B(CN)_4$] anion, ranging from 0.123 to 0.135 mol L^{-1} atm^{-1}, were more similar in magnitude to the imidazolium analogue, [emim][$B(CN)_4$] at 0.131 mol L^{-1} atm^{-1}. It has been noted that larger carbon dioxide solubility can be, at least in part, attributed to a decrease in electrostatic interactions or binding energy between the cation and anion in ionic liquids.[17, 21, 24] This suggests that there are stronger interactions between the bicyclic cations with the [Tf_2N] anions than the tetracyanoborate anions.

Recent discussion of CO_2 solubility in ILs is often presented in terms of concentration (mol L^{-1} atm^{-1}) to understand the applicability as a solvent or SILM, since volumetric capacity is important in applications of these materials. However, Henry's law

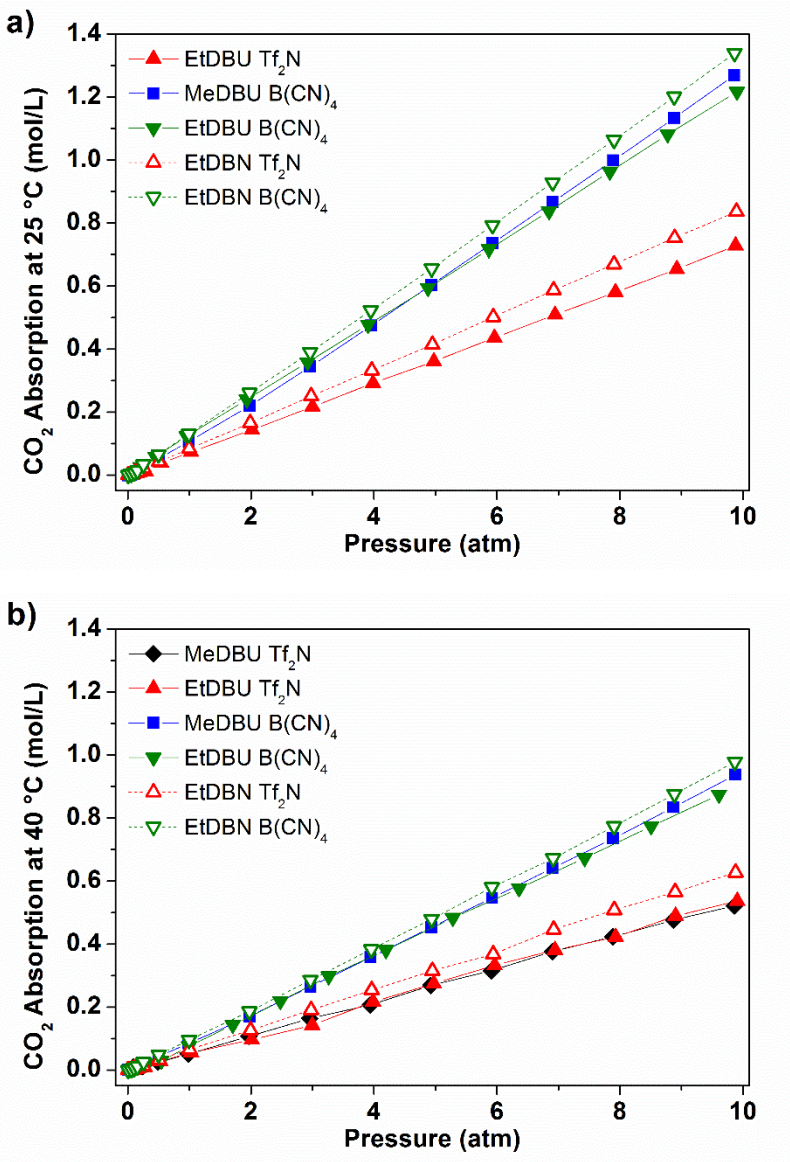

Figure 3-5. Carbon dioxide adsorption isotherms for the bicyclic ionic liquids at a) 25 °C and b) 40 °C

Table 3-2. Calculated values for the IL density (ρ), molar volume (V_m), fractional free volume (FFV). Experimentally determined CO_2 solubility, Henry's constants (HCO_2), gas permeability (P), selectivity (α), and diffusivity (D). All determined at 25 °C unless otherwise noted

	ρ^a	V_m		Solubility (mol/L atm)		
	(g/mL)	(cm^3/mol)	FFV^a	Pred.[a]	25°C	40°C
[MeDBU][Tf_2N]	1.4555	307	0.121	0.102	–	0.053
[MeDBU][$B(CN)_4$]	1.0865	260	0.134	0.260	0.128	0.094
[EtDBU][Tf_2N]	1.4260	323	0.124	0.099	0.074	0.055
[EtDBU][$B(CN)_4$]	1.0736	276	0.137	0.248	0.123	0.092
[MeDBN][Tf_2N]	1.4937	281	0.120	0.102	–	–
[MeDBN][$B(CN)_4$]	1.0905	233	0.135	0.257	–	–
[EtDBN][Tf_2N]	1.4533	298	0.125	0.102	0.085	0.064
[EtDBN][$B(CN)_4$]	1.0704	251	0.139	0.253	0.135	0.099
[emim][Tf_2N][d,e]	1.51	259	0.116	–	0.103	–
[emim][$B(CN)_4$][e]	1.03	219	0.132	–	0.128	–

[a]from COSMOtherm; [b]CO_2/N_2; [c]diffusivity calculated from P/S; [d]from ref.[8,60]; [e]from ref.[16,18]

Table 3-2 (continued)

	H_{CO2} (atm)	P (barrer)		α^b	D^c (cm^2/s)
		CO_2	N_2		
[MeDBU][Tf_2N]	–	–	–	–	–
[MeDBU][$B(CN)_4$]	34.6	834	17	49	2.21×10^{-6}
[EtDBU][Tf_2N]	41.2	432	16	26	1.98×10^{-6}
[EtDBU][$B(CN)_4$]	28.6	672	14	48	1.85×10^{-6}
[MeDBN][Tf_2N]	–	–	–	–	–
[MeDBN][$B(CN)_4$]	–	–	–	–	–
[EtDBN][Tf_2N]	39.6	787	27	29	3.14×10^{-6}
[EtDBN][$B(CN)_4$]	30.0	1583	33	48	3.98×10^{-6}
[emim][Tf_2N][d,e]	35.6	1702	73	23	5.60×10^{-6}
[emim][$B(CN)_4$][e]	38.9	2040	38	53	5.40×10^{-6}

[a]from COSMOtherm; [b]CO_2/N_2; [c]diffusivity calculated from P/S; [d]from ref.[8,60]; [e]from ref.[16,18]

constants are also commonly used to compare different types of sorbents on a mole fraction basis. These values were calculated from the 25 °C isotherms using the following equation

$$H_{CO_2} = \lim_{x \to 0} \frac{p}{\chi}$$

where p is the pressure and x is the mole fraction. The resulting Henry's constants, H_{CO2}, are reported in **Table 3-2**. The lowest Henry's constant corresponds to the highest CO_2 solubility, 28.6 for [EtDBU][$B(CN)_4$]. This represents more CO_2 dissolution than Cadena reported for [emim][Tf_2N].[60] It is important to note, there is some bias in Henry's constants of light gases due to the high molecular weight of most ILs. Hence, substantial differences in mole fraction could represent only small changes in the volumetric capacity and vice versa. As such, the Henry's constants do not always follow the same trends as the per-volume quantities, which is seen in our results here.

3.5.4 Free Volume

The cations were selected with a goal to increase the free volume in the ILs. Organic ring structures have non-planar conformations and vary in ring strain according to size. As such they occupy different space distributions which can change the packing of ions potentially allowing for additional void space between neighbors. The optimized structures for the cations, **Figure 3-6**, shows the added bulk in the DBU and DBN ILs. The free volume can be determined using the the molar volume (V_m) less the COSMO volume (V_{COSMO}) which represents the accessible surface area. However, looking at the free volume alone is not enough, since larger free volumes commonly correspond to higher molecular weights and molar volumes. To account for this possible co-dependence, the fractional free volume (*FFV*) can be used.

$$FFV = \frac{V_m - V_{COSMO}}{V_m}$$

FFV is a normalization of the free volume with respect to the molar volume, and as such it allows for unbiased direct comparisons amongst a variety of structures. The FFV

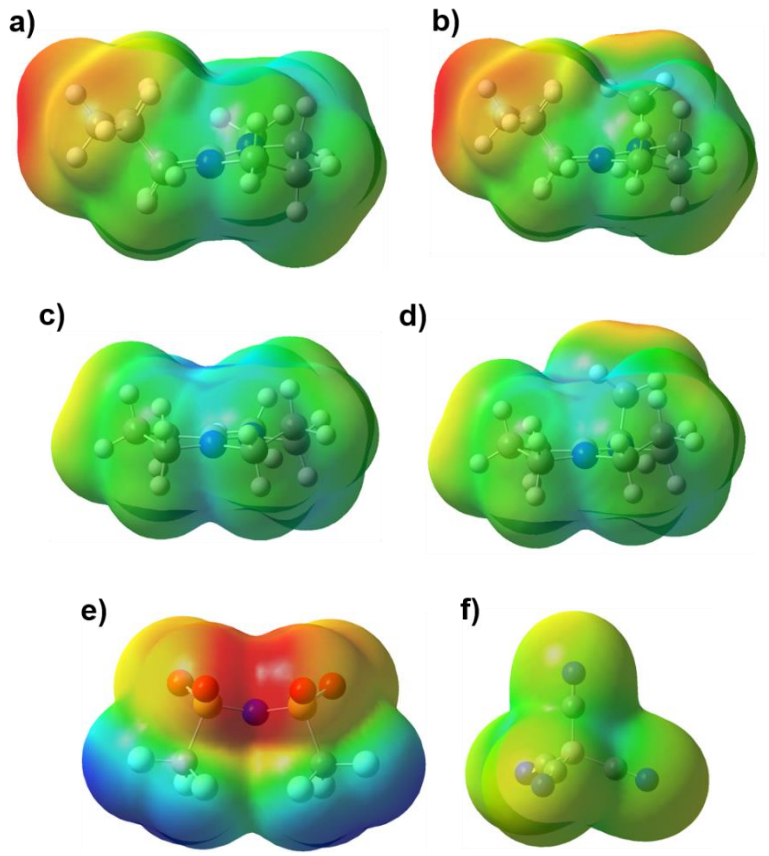

Figure 3-6. Optimized structures of ions a) [MeDBU], b) [EtDBU], c) [MeDBN], d) [EtDBN], e) [Tf_2N], f) [$B(CN)_4$]

values determined for the bicyclic ILs range from 0.120 to 0.139, as reported in **Table 3-2**. Both bicyclic structures exhibit enhanced free volume over imidazolium based ILs. While [emim][Tf_2N] has a FFV value of 0.116, the [EtDBU] and [EtDBN] analogues are significantly enhanced to 0.124 and 0.125, respectively. More modest changes are seen with the tetracyanoborate ILs, where [emim][$B(CN)_4$] has FFV of 0.132, and [EtDBU] and [EtDBN] have 0.134 and 0.137.

With respect to the two different bicyclic cations, both DBU and DBN analogues have nearly identical FFV when comparing ILs with the same substituent and anion. In general, the bicyclic amidine skeletal structure, which varies in size with five- or seven-membered secondary rings for DBN and DBU respectively, accounts for a smaller difference (~0.001 on average) than the alkyl substituent present. The size of the functional group contributes more (~0.003 on average) to the FFV than the torsion of the ring imparted from the bicyclic structure. For example, all bicyclic ILs with an ethyl substituent have slightly greater FFV values than the corresponding structure with methyl substituents. The ILs with the highest FFV contain the [$B(CN)_4$] anion. This is in agreement with previous results and has been attributed to the reduced cation–anion interactions.[17, 20]

3.5.5 SILM Single Gas Measurements

The carbon dioxide permeabilities, **Figure 3-7a**, of the bicyclic ionic liquids range from a low of approximately 430 for [EtDBU][Tf_2N] to a high of 1580 for [EtDBN][$B(CN)_4$]. When comparing the bicyclic ILs in this study, an increase in FFV allowed for enhancement of permeability in most cases. However, the presence of other influential variables, such as viscosity, may also contribute to these changes so no definitive relationship can be deduced. Although switching from an imidazolium to a bicyclic ring enhanced the fractional free volume in these ILs, we do not see an increase in the permeability in relation to some well-known ILs. In fact, the bicyclic IL with the best permeability falls just below the prototypical IL, [emim][Tf_2N], which has a permeability

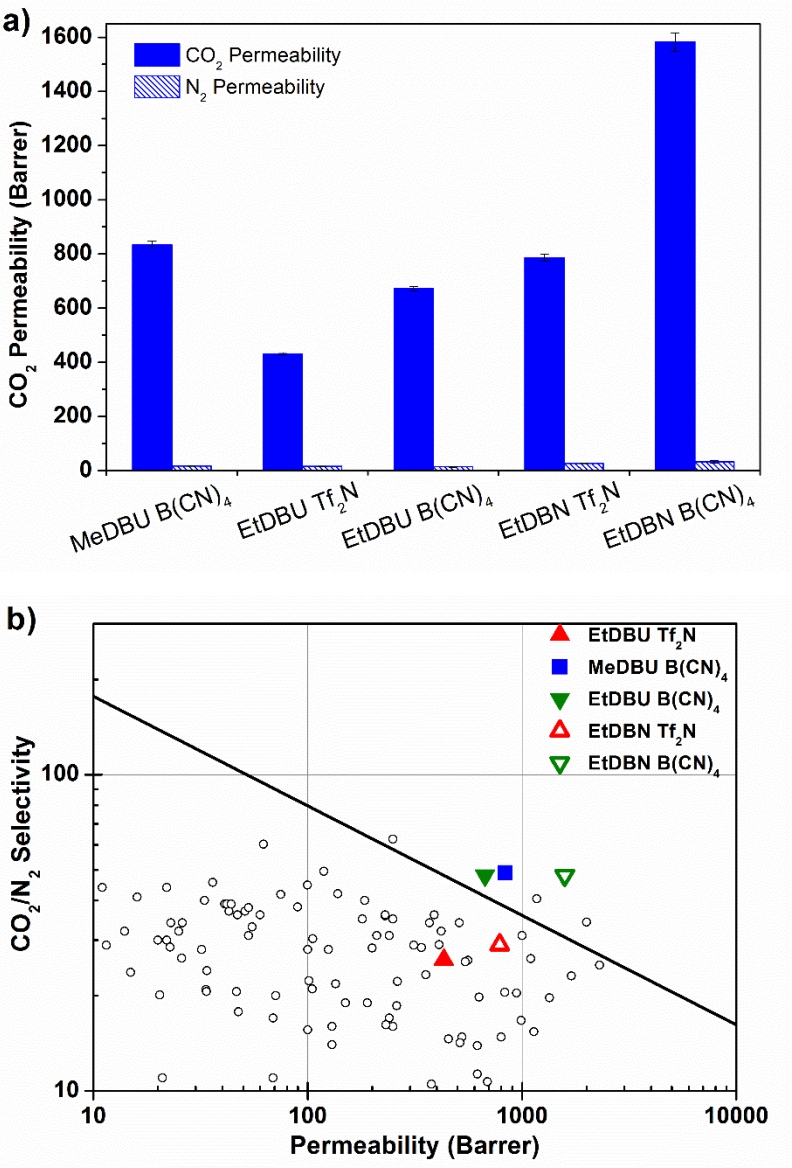

Figure 3-7. a) Carbon dioxide (solid) and nitrogen (stripes) permeability of the SILMs. b) Robeson plot showing a representative sample and five bicyclic ILs from this paper

of 1702 Barrer. The most notable similarities between these two ILs, [emim][Tf_2N] and [EtDBN][$B(CN)_4$], are their values for molar volume and viscosity, both of which are known to be important factors in gas permeability. These ILs diverge from one another with selectivity values of 23 and 48 respectively. The vast changes in values of FFV and solubility, both of which could be interrelated, might contribute to differences in selectivity.

In contrast, the nitrogen permeabilities encompass a much smaller range from 14 to 33 barrer from [EtDBU][$B(CN)_4$] to [EtDBN][$B(CN)_4$]. The nitrogen permeation remains quite low regardless of the anion paired with the bicyclic cation, while the carbon dioxide permeation is more dependent on the cation–anion pair. Using the single gas separation results, ideal selectivities were calculated for SILMs at room temperature, and there is a significant difference in selectivity values depending on the anion. Due to the enhancement of CO_2 permeation with minimal increase in nitrogen permeation, it was found that all three tetracyanoborate ILs [EtDBU][$B(CN)_4$], [MeDBU][$B(CN)_4$], and [EtDBN][$B(CN)_4$] exceeded Robeson's upper bound[61-62] with selectivity values around 48 as seen in **Figure 3-7b**. Computational modeling of other tetracyanoborate ionic liquids[20] has shown very similar diffusivity values for carbon dioxide and nitrogen, which suggests the permselectivity is indeed more greatly influenced by the solubility of these two gases. Experimental studies by Mahurin[18] have shown [emim][BCN_4] to have permeability of 2040 barrer and selectivity of 53, corresponding to a CO_2 solubility of 0.128 mol L^{-1} atm^{-1}. The results found here are similar to these past observations.

3.5.6 Calculated Diffusivity Values

Several approaches have been used to obtain the diffusivity of gases in ILs. Computations using molecular dynamics can be used to determine diffusivities of both the ions and the solute gases.[21] Experimental methods for monitoring the diffusion of gases in ionic liquids commonly use time-lag measurements and thin film procedures or, more recently, dynamic light scattering.[22, 63-64] Also, since permeability is the product of

solubility and diffusivity, the latter can be calculated from known values of the other two characteristics. Here we derived the diffusivity from the experimentally determined values of solubility and permeability at 25 °C. No noticeable patterns arise from the diffusivity values, as seen in **Table 3-2**. The lowest diffusivity value of 1.85×10^{-6} cm^2/s was calculated for [EtDBU][$B(CN)_4$], and in general CO_2 diffuses more slowly through the DBU than the DBN ILs. The highest diffusivity value for the bicyclic ILs was determined to be 3.98×10^{-6} cm^2/s which corresponds to [EtDBN][$B(CN)_4$]. Perhaps not surprisingly, this bicyclic IL also had the highest permeability in this series. The calculated diffusion coefficients found here seem to be reasonable, as evidenced by similar determinations for the imidazolium ILs in the literature. Moganty used a thin film technique to find a value of 5.6×10^{-6} cm^2/s for [emim][Tf_2N].[64] Also, Koller's molecular dynamic simulations of [emim][$B(CN)_4$] yielded a diffusivity of 5.5×10^{-6} cm^2/s.[65] Based on these findings, it seems the values derived from the solubility and permeability provide a reasonable estimate for the diffusivity of CO_2 in the bicyclic ILs.

3.6 Discussion

3.6.1 Permeation Properties

ILs comprised of bulky bicyclic cations were designed to increase the FFV in the ILs, and to examine the effects when allowing greater space between ions for gas absorption and diffusion. While the free space did increase compared to imidazolium-based ILs, fewer changes were observed between the two bicyclic structures. For instance, [EtDBN][Tf_2N] and [EtDBU][Tf_2N] have similar values of CO_2 solubility and FFV, differences of only 0.003 mol L^{-1} atm^{-1} and 0.001 in FFV predictions, however, results show that [EtDBN][Tf_2N] has a much higher permeability, by 355 barrer, than its [EtDBU][Tf_2N] counterpart. This suggests some other factor plays an important role. One possible explanation for the superior performance in permeability could be the significant difference in molar volumes, approximately 25 cm^3 mol^{-1}. The DBN ILs have smaller molar volume which means there are more ions present per unit volume, allowing for

increased CO_2-IL interactions in the same sized membrane. This can allow for enhanced transport into and through the SILM. Another deviation is DBN ILs have a higher CO_2 diffusivity than the DBU derivatives, allowing for faster transfer of gases through the IL. This contributes to the increased permeability between [EtDBN][Tf_2N] and [EtDBU][Tf_2N]. Regardless of specific structure, all the bicyclic ILs have significantly lower rates of CO_2 diffusion compared to the [emim] derivatives with the same anions. It is possible that the additional free space is less accessible to CO_2 leading to reduced diffusivity, or there might be greater solute-solvent interactions between the CO_2 and the IL leading to slower diffusion as well. Several models relate the diffusivity to viscosity, because greater fluidity leads to faster CO_2 mass transfer kinetics.

One of the greatest physical differences among these ILs is their viscosity. For instance, each DBN based IL is less than half the viscosity of the DBU based equivalent. It can be seen from **Table 3-1** that as viscosity decreases, the permeability increases, a trend that has been seen in a variety of other ionic liquids as well.[8] Since other characteristics of DBU and DBN derivatives are quite similar, it is likely this variation in viscosity also contributes to their differences in permeability. Correlations between viscosity and gas solubility have been examined in the past,[66] and have shown dependence of the solubility relies primarily on the solvent–solvent and solute–solute interactions with little dependence on solute–solvent interactions. In some cases, the viscosity of the IL decreases following the sorption of carbon dioxide and increasing mole fraction of CO_2.[22-23] This is due to the decrease in molecular interactions leading to corresponding weakened IL cation–anion interactions, reducing the dynamic viscosity further and increasing diffusivity. While it has been recognized that some of the greatest differences for ionic liquids are based upon their anion, alterations of the cation structure and substituents can also contribute to these differences. However, due to physical characteristics like high melting point some ion pairs with preferential cations are unable to be tested, limiting our scope.

3.6.2 The Role of FFV in Solubility

To our knowledge, there have only been a few previous studies on FFV in ionic liquids, and their primary focus is on solubility. Shannon and coworkers proposed that fractional free volume, rather than molar volume, could be an important factor in gas solubility.[25] Through a systematic analysis of 165 alkyl imidazolium ILs using COSMOtherm, they noticed lengthening the alkyl chain induced a corresponding increase in FFV. However, by modifying only the length of the hydrocarbon substituent, the ILs with the highest fractional free volume also had the highest molar volume. Past experiments have shown that CO_2 dissolution, on a mole per liter basis, is decreased when going from methyl to octyl imidazolium ILs,[66] so the authors suggested a small free volume was favorable for solubility. As a follow up, Horne[67] explored the effects of adding polar R-groups, which are more CO_2-phillic, to the imidazolium cation ring. Regardless of the added functionality, these ILs had smaller FFV than similar alkyl derivatives, seeming to confirm an inverse relationship between FFV and gas solubility and selectivity. Research thus far indicates that ILs with small fractional free volumes tend to exhibit higher CO_2 solubility.

Interestingly, here we see the opposite relationship in the bicyclic ILs, where increasing the free volume maintains or even enhances the solubility and permeability of CO_2. Through methodical variation of both the bicyclic cation and anion, we saw unique IL combinations where the highest FFV does not correspond with the highest molar volume, an important difference from the previous studies. Yet again we are reminded that no single feature can describe this complex system. In past works, the Camper Model has been used to predict the solubility and selectivity of gases in imidazolium ILs using molar volumes.[68] For the gas of interest, CO_2, the model presents a maximum peak of solubility in imidazolium ILs with relatively small molar volumes from 200–300 cm^2/mol as seen in **Figure 3-8**. While this model neglects cation/anion interactions and has not yet been adapted for other systems, it provides an interesting comparison for the bicyclic ILs.

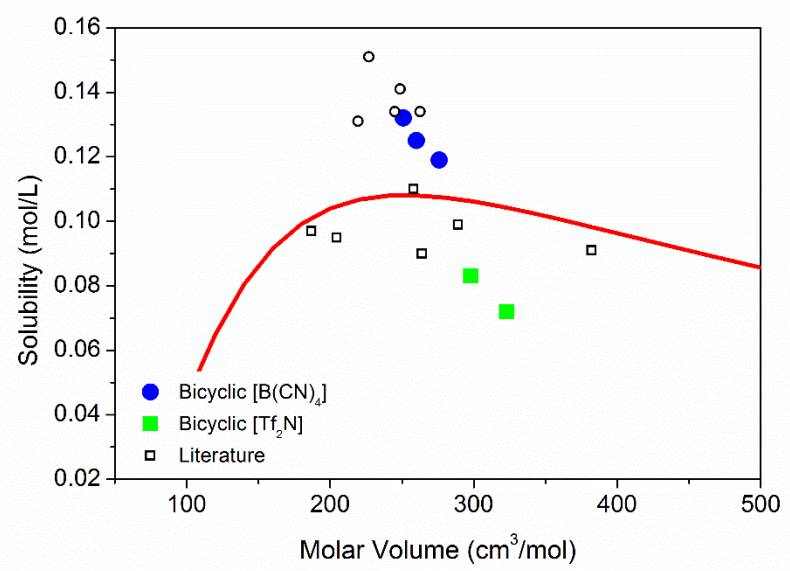

Figure 3-8. Plot of solubility and molar volume with Camper's model (red line), literature values (open squares and circles[18]), and the bicyclic ILs with [Tf_2N] (green squares) and [$B(CN)_4$] (blue circles)

In this series of bicyclic ILs, the largest FFV, 0.139 for [EtDBN] [$B(CN)_4$], corresponds to one of the lowest molar volumes, 250 cc/mol, which is within the optimal region for molar volume predicted by the Camper model. For favorable dissolution, it seems that a large free space in a small molar volume allows for an ideal combination. Neither molar volume nor FFV alone can provide a clear guideline to the optimum IL, but a balance could be realized by accounting for the contributions of both. Our observations in this paper suggest that more consideration should be given to ILs with high FFV in a composition that is beneficial for CO_2 sorption, with a caveat on limiting the molar volume. A three-dimensional rendering of the molar volume, solubility, and FFV for these ionic liquids is provided in supporting information. (**Figure 3-12**)

3.7 Conclusions

SILMs of bicyclic ionic liquids derived from DBU and DBN were characterized and determined to possess excellent thermal stability, and adequate free volume to promote CO_2 solubility, permeability, and selectivity. SILMs of ionic liquids with DBN cations had significantly greater permeability than DBU, at least in part due to the reduction in viscosity by about one half. Three of the ILs with the tetracyanoborate anion surpassed Robeson's upper bound with permeability values from 670–1580 Barrer due to selectivity values of approximately 48. These bicyclic ILs do not represent the maximum potential permeability since their bulky structures, while adding free volume, also imparted higher viscosities and lower diffusivities. Ionic liquids with small molar volume, large fractional free volume, low viscosity, and increased solubility for the gas of interest could allow great permeability and selectivity to be attained. Maximizing free space in a small molar volume can allow for enhanced solubility. When considering FFV, attention must be given to the method in which free volume is achieved, as it cannot sacrifice the solubility of the preferred gas.

3.8 Acknowledgements

This work was supported by the U.S. Department of Energy, Office of Science, Basic Energy Sciences, Chemical Sciences, Geosciences, and Biosciences Division.

3.9 Supporting Information

3.9.1 Synthetic Procedure

8-methyl-1,8-diazabicyclo[5.4.0]undec-7-en-8-ium iodide [MeDBU][I] (1a)

To an ice-cooled solution of 1,8-diazabicyclo[5.4.0]undec-7-ene (DBU) (3.04 g, 19.60 mmol) in ethyl acetate (50 mL) was slowly added iodomethane (1.95 mL, 31.36 mmol), and the mixture was stirred at room temperature overnight. The precipitate was then filtered, washed with petroleum ether, and dried under vacuum to give **1a** as a slightly off-white solid (5.52 g, 96%).

^{1}H NMR ($CDCl_3$, 500 MHz) δ 3.71–3.68 (m, 2H), 3.68–3.61 (m, 4H), 3.33 (s, 3H), 2.94–2.89 (m, 2H), 2.23–2.17 (m, 2H), 1.84–1.77 (m, 6H). ^{13}C NMR ($CDCl_3$, 126 MHz) δ 167.0, 55.9, 49.5, 49.3, 42.2, 29.7, 28.7, 26.3, 22.5, 20.2. MS (ESI positive) *m/z*: $[C_{10}H_{19}N_2]^+$ calcd: 167.15; found: 167.16. MS (ESI negative) *m/z*: $[I]^-$ calcd: 126.91; found: 126.91.

8-ethyl-1,8-diazabicyclo[5.4.0]undec-7-en-8-ium iodide [EtDBU][I] (1b)

This compound was prepared, following the procedure for **1a**, from DBU (3.06 g, 19.71 mmol) and iodoethane (2.53 mL, 31.53 mmol) as a white solid (5.55 g, 91%).

^{1}H NMR ($CDCl_3$, 500 MHz) δ 3.72–3.69 (m, 2H), 3.67 (t, J = 6.0 Hz, 2H), 3.64–3.57 (m, 4H), 2.92–2.87 (m, 2H), 2.21–2.14 (m, 2H), 1.81–1.77 (m, 6H), 1.28 (t, J = 7.3 Hz, 3H). ^{13}C NMR ($CDCl_3$, 126 MHz) δ 166.4, 55.8, 49.7, 49.5, 46.8, 29.0, 28.5, 26.2, 23.2, 20.4, 14.1. MS (ESI positive) *m/z*: $[C_{11}H_{21}N_2]^+$ calcd: 181.17; found: 181.17. MS (ESI negative) *m/z*: $[I]^-$ calcd: 126.91; found: 126.91.

8-methyl-1,8-diazabicyclo[5.4.0]undec-7-en-8-ium bis(trifluoromethanesulfonyl)imide [MeDBU][Tf_2N] (2a)

Iodide **1a** (2.56 g, 8.69 mmol) was dissolved in deionized water (25 mL), and a solution of lithium bis(trifluoromethanesulfonyl)imide ($LiNTf_2$) (2.74 g, 9.56 mmol) in deionized water (5 mL) was added. After stirring the mixture at room temperature overnight, the precipitates were filtered, washed with deionized water, and dried under vacuum to yield **2a** as a slightly off-white solid (3.25 g, 84%). Characterizations matched those reported in the literature.[69]

^{1}H NMR ($CDCl_3$, 500 MHz) δ 3.65–3.60 (m, 2H), 3.55–3.47 (m, 4H), 3.26 (s, 3H), 2.85–2.79 (m, 2H), 2.16–2.10 (m, 2H), 1.83–1.70 (m, 6H). ^{13}C NMR ($CDCl_3$, 126 MHz) δ 167.0, 120.1 (q, $J_{C–F}$ = 321.0 Hz, NTf_2), 55.5, 49.0, 48.9, 41.3, 28.9, 28.8, 26.3, 22.3, 20.0. MS (ESI positive) *m/z*: $[C_{10}H_{19}N_2]^+$ calcd: 167.15; found: 167.16. MS (ESI negative) *m/z*: $[C_2F_6NO_4S_2]^-$ calcd: 279.92; found: 279.93.

8-ethyl-1,8-diazabicyclo[5.4.0]undec-7-en-8-ium bis(trifluoromethanesulfonyl)imide [EtDBU][Tf_2N] (2b)

Iodide **1b** (2.52 g, 8.19 mmol) was dissolved in deionized water (25 mL), and a solution of $LiNTf_2$ (2.59 g, 9.01 mmol) in deionized water (5 mL) was added. After stirring the mixture at room temperature overnight, dichloromethane (30 mL) was added. The organic layer was separated, washed with deionized water (3 × 30 mL), dried over magnesium sulfate, filtered, concentrated, and dried under vacuum to afford **2b** as a slightly light yellow liquid (3.29 g, 87%).

Characterizations matched those reported in the literature.[59]

^{1}H NMR ($CDCl_3$, 500 MHz) δ 3.64–3.61 (m, 2H), 3.57–3.51 (m, 4H), 3.51–3.47 (m, 2H), 2.83–2.79 (m, 2H), 2.14–2.08 (m, 2H), 1.83–1.71 (m, 6H), 1.26 (t, J = 7.3 Hz, 3H). ^{13}C NMR ($CDCl_3$, 126 MHz) δ 166.6, 120.1 (q, $J_{C–F}$ = 321.5 Hz, NTf_2), 55.4, 49.3, 49.2, 46.5, 28.7, 28.3, 26.2, 23.1, 20.2, 13.7. MS (ESI positive) *m/z*: $[C_{11}H_{21}N_2]^+$ calcd: 181.17; found: 181.20. MS (ESI negative) *m/z*: $[C_2F_6NO_4S_2]^-$ calcd: 279.92; found: 279.96.

8-methyl-1,8-diazabicyclo[5.4.0]undec-7-en-8-ium tetracyanoborate [MeDBU][B(CN)$_4$] (3a)

Iodide **1a** (1.03 g, 3.52 mmol) was dissolved in methanol (7 mL), and a solution of potassium tetracyanoborate [KB(CN)$_4$] (0.56 g, 3.52 mmol) in methanol (5 mL) was added. After stirring the mixture at room temperature under N_2 overnight, the solvent was evaporated, and the residue was dissolved in dichloromethane (50 mL), washed with deionized water (6 × 50 mL), dried over magnesium sulfate, filtered, concentrated, and dried under vacuum to provide **3a** as a yellow liquid (0.66 g, 66%). ^{1}H NMR ($CDCl_3$, 500 MHz) δ 3.69–3.65 (m, 2H), 3.57 (t, J = 5.9 Hz, 2H), 3.53 (t, J = 5.9 Hz, 2H), 3.31 (s, 3H), 2.87–2.83 (m, 2H), 2.22–2.17 (m, 2H), 1.89–1.76 (m, 6H). ^{13}C NMR ($CDCl_3$, 126 MHz) δ 167.0, 123.7, 123.1, 122.5, 122.0, 55.8, 49.2, 49.1, 41.5, 29.0, 28.7, 26.4, 22.4, 20.1. ^{11}B NMR ($CDCl_3$, 128 MHz) δ −38.22. MS (ESI positive) *m/z*: $[C_{10}H_{19}N_2]^+$ calcd: 167.15; found: 167.17. MS (ESI negative) *m/z*: $[C_4BN_4]^-$ calcd: 115.02; found: 115.05.

8-ethyl-1,8-diazabicyclo[5.4.0]undec-7-en-8-ium tetracyanoborate [EtDBU][B(CN)$_4$] (3b)

This compound was prepared, following the procedure for **3a**, from **1b** (2.01 g, 6.52 mmol) and KB(CN)$_4$ (1.03 g, 6.52 mmol) as a yellow liquid (1.64 g, 85%). ^{1}H NMR ($CDCl_3$, 500 MHz) δ 3.68–3.64 (m, 2H), 3.62–3.55 (m, 4H), 3.52 (t, J = 5.9 Hz, 2H), 2.85–2.81 (m, 2H), 2.20–2.15 (m, 2H), 1.89–1.75 (m, 6H), 1.32 (t, J = 7.3 Hz, 3H). ^{13}C NMR ($CDCl_3$, 126 MHz) δ 166.6, 123.7, 123.1, 122.5, 122.0, 55.7, 49.5, 49.4, 46.7, 28.6, 28.5, 26.2, 23.2, 20.2, 13.9. ^{11}B NMR ($CDCl_3$, 128 MHz) δ −38.21. MS (ESI positive) *m/z*: $[C_{11}H_{21}N_2]^+$ calcd: 181.17; found: 181.20. MS (ESI negative) *m/z*: $[C_4BN_4]^-$ calcd: 115.02; found: 115.04.

5-methyl-1,5-diazabicyclo[4.3.0]non-5-en-5-ium iodide [MeDBN][I] (4a)

To an ice-cooled solution of 1,5-diazabicyclo[4.3.0]non-5-ene (DBN) (3.02 g, 23.83 mmol) in ethyl acetate (50 mL) was slowly added iodomethane (2.37 mL, 38.12 mmol), and the mixture was stirred at room temperature overnight. The precipitate was then

filtered, washed with petroleum ether, and dried under vacuum to give **4a** as a white solid (6.15 g, 97%).

^{1}H NMR ($CDCl_3$, 500 MHz) δ 3.79 (t, J = 7.4 Hz, 2H), 3.55–3.48 (m, 4H), 3.20 (s, 3H), 3.17 (t, J = 8.1 Hz, 2H), 2.25–2.17 (m, 4H). ^{13}C NMR ($CDCl_3$, 126 MHz) δ 165.5, 54.8, 47.3, 42.5, 41.0, 32.0, 19.3, 18.2. MS (ESI positive) *m/z*: $[C_8H_{15}N_2]^+$ calcd: 139.12; found: 139.13. MS (ESI negative) *m/z*: $[I]^-$ calcd: 126.91; found: 126.91.

5-ethyl-1,5-diazabicyclo[4.3.0]non-5-en-5-ium iodide [EtDBN][I] (4b)

This compound was prepared, following the procedure for **4a**, from DBN (3.02 g, 23.83 mmol) and iodoethane (3.07 mL, 38.13 mmol) as a white solid (5.73 g, 86%).

^{1}H NMR ($CDCl_3$, 500 MHz) δ 3.86–3.80 (m, 2H), 3.55–3.51 (m, 4H), 3.49 (q, J = 7.3 Hz, 2H), 3.17 (t, J = 8.0 Hz, 2H), 2.27–2.19 (m, 4H), 1.31 (t, J = 7.3 Hz, 3H). ^{13}C NMR ($CDCl_3$, 126 MHz) δ 164.7, 54.9, 48.8, 44.4, 42.8, 31.5, 19.4, 18.4, 13.3. MS (ESI positive) *m/z*: $[C_9H_{17}N_2]^+$ calcd: 153.14; found: 153.14. MS (ESI negative) *m/z*: $[I]^-$ calcd: 126.91; found: 126.90.

5-methyl-1,5-diazabicyclo[4.3.0]non-5-en-5-ium bis(trifluoromethanesulfonyl)imide [MeDBN][Tf_2N] (5a)

This compound was prepared, following the procedure for **2a**, from **4a** (2.03 g, 7.62 mmol) and $LiNTf_2$ (2.19 g, 7.62 mmol) as a white solid (2.74 g, 86%). ^{1}H NMR ($CDCl_3$, 500 MHz) δ 3.74 (t, J = 7.4 Hz, 2H), 3.46–3.38 (m, 4H), 3.16 (s, 3H), 3.00 (t, J = 7.9 Hz, 2H), 2.24–2.12 (m, 4H). ^{13}C NMR ($CDCl_3$, 126 MHz) δ 165.1, 120.1 (q, $J_{C–F}$ = 321.4 Hz, NTf_2), 54.6, 46.8, 42.1, 40.2, 30.8, 19.0, 18.0. MS (ESI positive) *m/z*: $[C_8H_{15}N_2]^+$ calcd: 139.12; found: 139.12. MS (ESI negative) *m/z*: $[C_2F_6NO_4S_2]^-$ calcd: 279.92; found: 279.92.

5-ethyl-1,5-diazabicyclo[4.3.0]non-5-en-5-ium bis(trifluoromethanesulfonyl)imide [EtDBN][Tf_2N] (5b)

This compound was prepared, following the procedure for **2b**, from **4b** (2.53 g, 9.03 mmol) and $LiNTf_2$ (2.59 g, 9.03 mmol) as a slightly light yellow liquid (3.51 g, 90%). Characterizations matched those reported in the literature.[2]

^{1}H NMR ($CDCl_3$, 500 MHz) δ 3.74 (t, J = 7.3 Hz, 2H), 3.47–3.38 (m, 6H), 3.00 (t, J = 7.9 Hz, 2H), 2.26–2.10 (m, 4H), 1.27 (t, J = 7.3 Hz, 3H). ^{13}C NMR ($CDCl_3$, 126 MHz) δ 164.3, 120.1 (q, $J_{C–F}$ = 321.6 Hz, NTf_2), 54.4, 48.4, 43.9, 42.4, 30.3, 19.0, 18.1, 12.7. MS (ESI positive) *m/z*: $[C_9H_{17}N_2]^+$ calcd: 153.14; found: 153.14. MS (ESI negative) *m/z*: $[C_2F_6NO_4S_2]^-$ calcd: 279.92; found: 279.92.

5-methyl-1,5-diazabicyclo[4.3.0]non-5-en-5-ium tetracyanoborate [MeDBN][B(CN)$_4$] (6a)

This compound was prepared, following the procedure for **3a**, from **4a** (3.00 g, 11.29 mmol) and $KB(CN)_4$ (1.79 g, 11.29 mmol) as a light yellow solid (2.36 g, 82%). ^{1}H NMR ($CDCl_3$, 500 MHz) δ 3.79 (t, J = 7.4 Hz, 2H), 3.50–3.43 (m, 4H), 3.22 (s, 3H), 3.03 (t, J = 8.0 Hz, 2H), 2.31–2.17 (m, 4H). ^{13}C NMR ($CDCl_3$, 126 MHz) δ 164.9, 123.6, 123.1, 122.5, 121.9, 54.7, 47.0, 42.3, 40.5, 30.9, 19.1, 18.2. ^{11}B NMR ($CDCl_3$, 128 MHz) δ −38.29. MS (ESI positive) *m/z*: $[C_8H_{15}N_2]^+$ calcd: 139.12; found: 139.11. MS (ESI negative) *m/z*: $[C_4BN_4]^-$ calcd: 115.02; found: 115.01.

5-ethyl-1,5-diazabicyclo[4.3.0]non-5-en-5-ium tetracyanoborate [EtDBN][B(CN)$_4$] (6b)

This compound was prepared, following the procedure for **3a**, from **4b** (2.02 g, 7.23 mmol) and $KB(CN)_4$ (1.15 g, 7.23 mmol) as a yellow liquid (1.70 g, 88%). ^{1}H NMR ($CDCl_3$, 500 MHz) δ 3.81–3.76 (m, 2H), 3.52–3.43 (m, 6H), 3.03 (t, J = 8.0 Hz, 2H), 2.32–2.15 (m, 4H), 1.33 (t, J = 7.3 Hz, 3H). ^{13}C NMR ($CDCl_3$, 126 MHz) δ 164.2, 123.6, 123.1, 122.5, 121.9, 54.6, 48.7, 44.1, 42.6, 30.4, 19.1, 18.2, 13.0. ^{11}B NMR ($CDCl_3$, 128 MHz) δ −38.28. MS (ESI positive) *m/z*: $[C_9H_{17}N_2]^+$ calcd: 153.14; found: 153.14. MS (ESI negative) *m/z*: $[C_4BN_4]^-$ calcd: 115.02; found: 115.02.

3.9.2 Supporting Figures

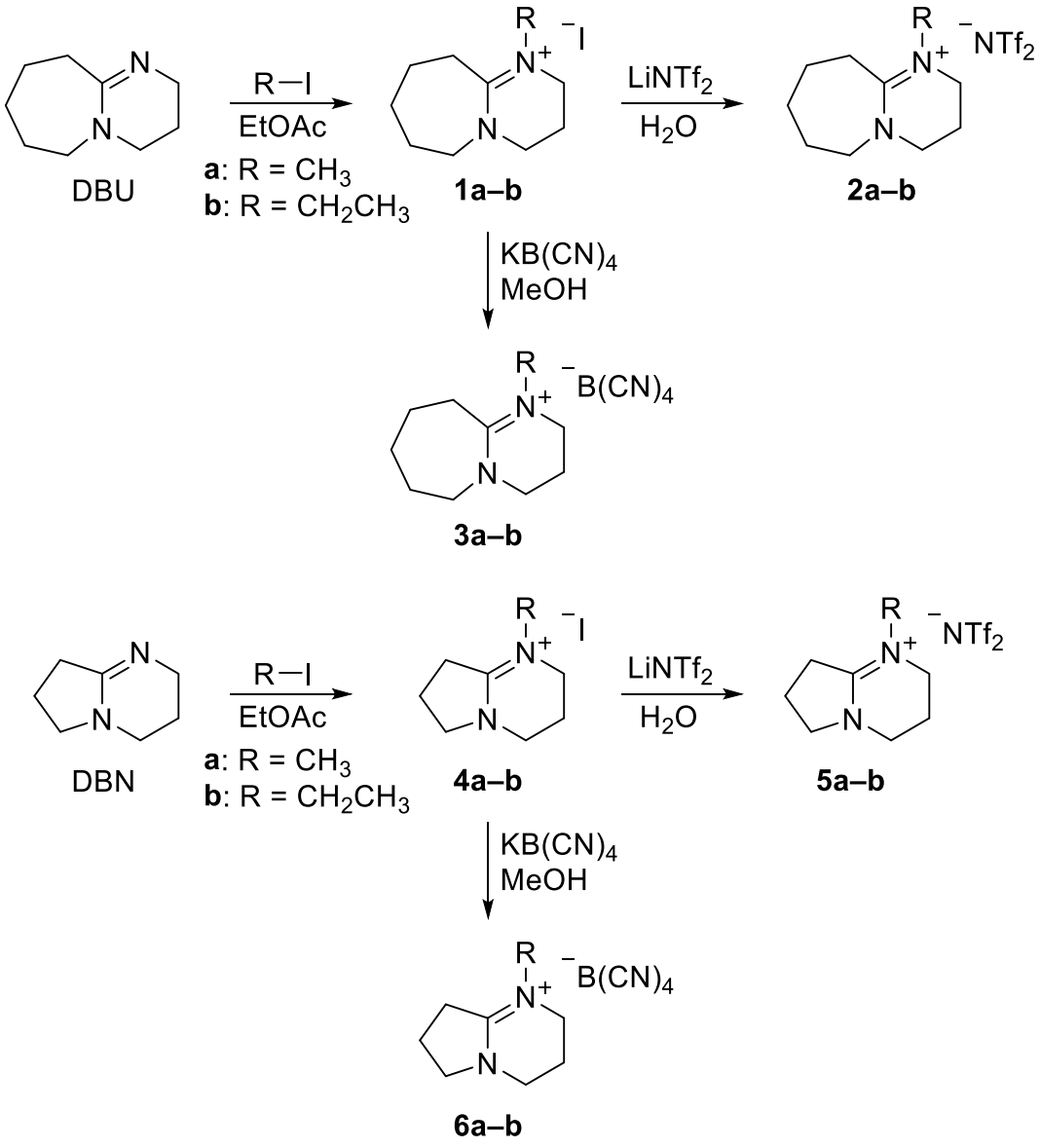

Figure 3-9. Synthesis scheme for bicyclic ionic salts and liquids

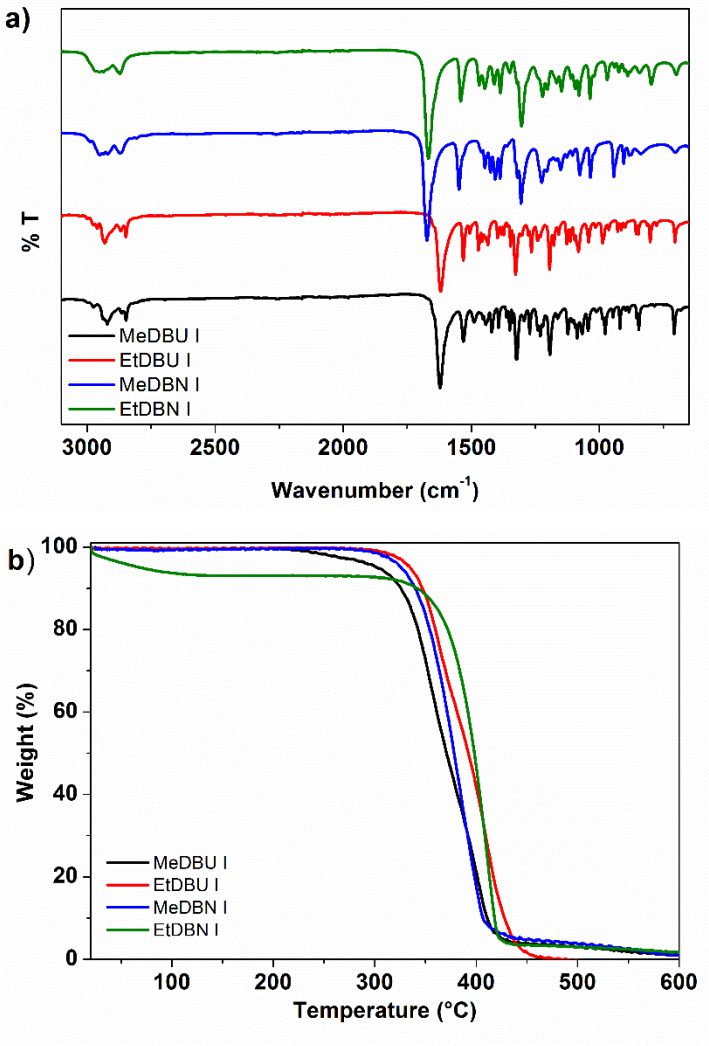

Figure 3-10. a) FTIR and b) TGA for bicyclic iodide precursors

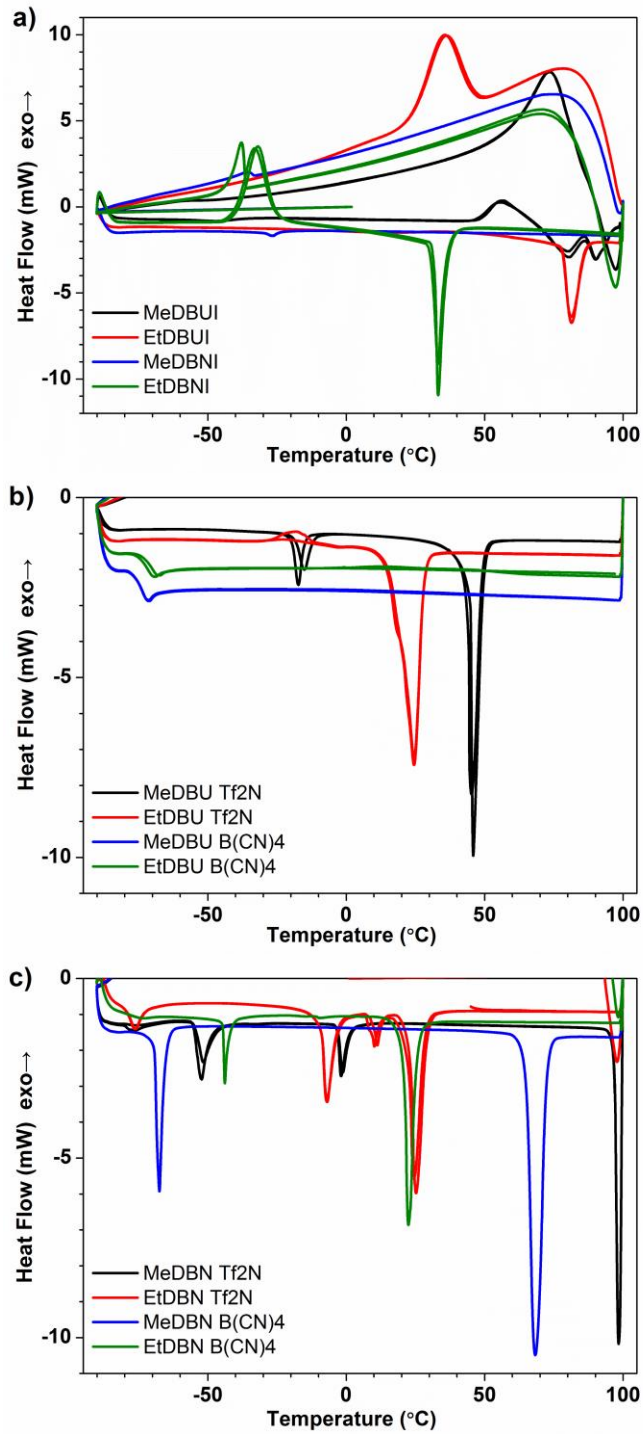

Figure 3-11. DSC curves for a) bicyclic iodide precursors b) $[DBU]^+$ based ILs c) $[DBN]^+$ based ILs

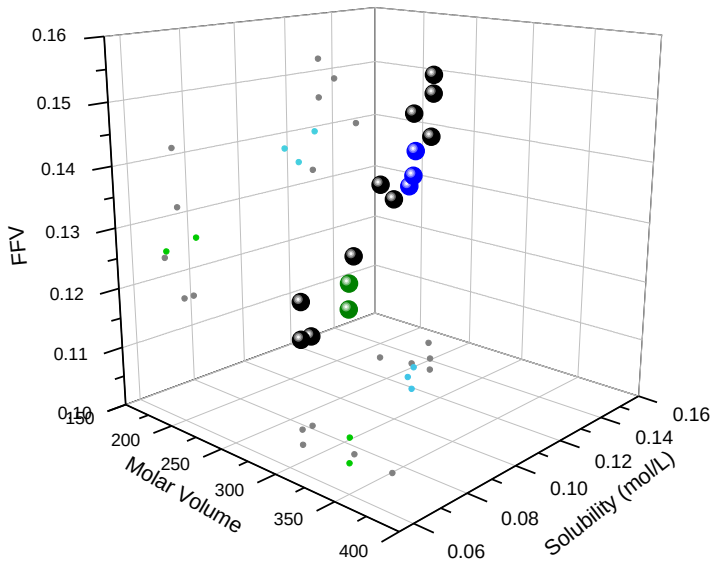

Figure 3-12. 3-D plot showing the relationship between molar volume, fractional free volume, and solubility. Bicyclic ILs with [Tf_2N] (green spheres) and [$B(CN)_4$] (blue spheres), and literature ILs [18, 54] (black spheres), with projections onto the xy and yz planes for clarity

3.10 References

1. Boot-Handford, M. E.; Abanades, J. C.; Anthony, E. J.; Blunt, M. J.; Brandani, S.; Mac Dowell, N.; Fernandez, J. R.; Ferrari, M. C.; Gross, R.; Hallett, J. P.; Haszeldine, R. S.; Heptonstall, P.; Lyngfelt, A.; Makuch, Z.; Mangano, E.; Porter, R. T. J.; Pourkashanian, M.; Rochelle, G. T.; Shah, N.; Yao, J. G.; Fennell, P. S., Carbon capture and storage update. *Energy & Environmental Science* **2014,** *7* (1), 130-189.

2. Markewitz, P.; Kuckshinrichs, W.; Leitner, W.; Linssen, J.; Zapp, P.; Bongartz, R.; Schreiber, A.; Muller, T. E., Worldwide innovations in the development of carbon capture technologies and the utilization of CO_2. *Energy & Environmental Science* **2012,** *5* (6), 7281-7305.

3. Youn-Sang, B.; Q., S. R., Development and Evaluation of Porous Materials for Carbon Dioxide Separation and Capture. *Angew. Chem. Int. Ed.* **2011,** *50* (49), 11586-11596.

4. Freemantle, M., *An introduction to ionic liquids*. Royal Society of Chemistry: Cambridge, 2010.

5. Ionic Liquids: Industrial Applications for Green Chemistry. In *ACS Symp. Ser.* [Online] Robin, D. R.; Kenneth, R. S., Eds. American Chemical Society: 2002; p. 492. http://dx.doi.org/10.1021/bk-2002-0818.

6. Xiong, Y. B.; Wang, H.; Wang, Y. J.; Wang, R. M., Novel imidazolium-based poly(ionic liquid)s: preparation, characterization, and absorption of CO_2. *Polym. Adv. Technol.* **2012,** *23* (5), 835-840.

7. Zhang, X.; Zhang, X.; Dong, H.; Zhao, Z.; Zhang, S.; Huang, Y., Carbon capture with ionic liquids: overview and progress. *Energy & Environmental Science* **2012,** *5* (5), 6668-6681.

8. Scovazzo, P., Determination of the upper limits, benchmarks, and critical properties for gas separations using stabilized room temperature ionic liquid membranes (SILMs) for the purpose of guiding future research. *J. Membr. Sci.* **2009,** *343* (1–2), 199-211.

9. Dai, Z.; Noble, R. D.; Gin, D. L.; Zhang, X.; Deng, L., Combination of ionic liquids with membrane technology: A new approach for CO_2 separation. *J. Membr. Sci.* **2016,** *497*, 1-20.

10. Shannon, M. S.; Bara, J. E., Reactive and Reversible Ionic Liquids for CO_2 Capture and Acid Gas Removal. *Sep. Sci. Technol.* **2012,** *47* (2), 178-188.

11. Kumar, S.; Cho, J. H.; Moon, I., Ionic liquid-amine blends and CO_2BOLs: Prospective solvents for natural gas sweetening and CO_2 capture technology-A review. *Int. J. Greenh. Gas Control* **2014,** *20*, 87-116.

12. Koros, W. J.; Kratochvil, A.; Shu, S.; Husain, S., Energy and Environmental Issues and Impacts of Membranes in Industry. In *Membrane Operations: Innovative Separations and Transformations*, Drioli, E.; Giorno, L., Eds. Wiley-VCH: Weinheim, 2009.

13. Brennecke, J. E.; Gurkan, B. E., Ionic Liquids for CO_2 Capture and Emission Reduction. *J. Phys. Chem. Lett.* **2010,** *1* (24), 3459-3464.

14. Tome, L. C.; Patinha, D. J. S.; Freire, C. S. R.; Rebelo, L. P. N.; Marrucho, I. M., CO_2 separation applying ionic liquid mixtures: the effect of mixing different anions on gas permeation through supported ionic liquid membranes. *RSC Advances* **2013,** *3* (30), 12220-12229.

15. Ramdin, M.; de Loos, T. W.; Vlugt, T. J. H., State-of-the-Art of CO_2 Capture with Ionic Liquids. *Ind. Eng. Chem. Res.* **2012,** *51* (24), 8149-8177.

16. Mahurin, S. M.; Lee, J. S.; Baker, G. A.; Luo, H.; Dai, S., Performance of nitrile-containing anions in task-specific ionic liquids for improved CO_2/N_2 separation. *J. Membr. Sci.* **2010,** *353* (1-2), 177-183.

17. Babarao, R.; Dai, S.; Jiang, D.-e., Understanding the High Solubility of CO_2 in an Ionic Liquid with the Tetracyanoborate Anion. *The Journal of Physical Chemistry B* **2011,** *115* (32), 9789-9794.

18. Mahurin, S. M.; Hillesheim, P. C.; Yeary, J. S.; Jiang, D. E.; Dai, S., High CO_2 solubility, permeability and selectivity in ionic liquids with the tetracyanoborate anion. *Rsc Advances* **2012,** *2* (31), 11813-11819.

19. Tome, L. C.; Florindo, C.; Freire, C. S. R.; Rebelo, L. P. N.; Marrucho, I. M., Playing with ionic liquid mixtures to design engineered CO_2 separation membranes. *PCCP* **2014,** *16* (32), 17172-17182.

20. Liu, H.; Dai, S.; Jiang, D.-e., Structure and dynamics of CO_2 and N_2 in a tetracyanoborate based ionic liquid. *PCCP* **2014,** *16* (5), 1909-1913.

21. Liu, H.; Dai, S.; Jiang, D.-e., Molecular Dynamics Simulation of Anion Effect on Solubility, Diffusivity, and Permeability of Carbon Dioxide in Ionic Liquids. *Ind. Eng. Chem. Res.* **2014,** *53* (25), 10485-10490.

22. Rausch, M. H.; Heller, A.; Herbst, J.; Koller, T. M.; Bahlmann, M.; Schulz, P. S.; Wasserscheid, P.; Fröba, A. P., Mutual and Thermal Diffusivity of Binary Mixtures of the Ionic Liquids [BMIM][$C(CN)_3$] and [BMIM][$B(CN)_4$] with Dissolved CO_2 by Dynamic Light Scattering. *The Journal of Physical Chemistry B* **2014,** *118* (17), 4636-4646.

23. Bi, S.; Koller, T. M.; Rausch, M. H.; Wasserscheid, P.; Fröba, A. P., Dynamic Viscosity of Tetracyanoborate- and Tricyanomethanide-Based Ionic Liquids by Dynamic Light Scattering. *Ind. Eng. Chem. Res.* **2015,** *54* (11), 3071-3081.

24. Gupta, K. M., Tetracyanoborate based ionic liquids for CO_2 capture: From ab initio calculations to molecular simulations. *Fluid Phase Equilib.* **2016,** *415*, 34-41.

25. Shannon, M. S.; Tedstone, J. M.; Danielsen, S. P. O.; Hindman, M. S.; Irvin, A. C.; Bara, J. E., Free Volume as the Basis of Gas Solubility and Selectivity in Imidazolium-Based Ionic Liquids. *Ind. Eng. Chem. Res.* **2012,** *51* (15), 5565-5576.

26. Jessop, P. G.; Heldebrant, D. J.; Li, X.; Eckert, C. A.; Liotta, C. L., Green chemistry: Reversible nonpolar-to-polar solvent. *Nature* **2005,** *436* (7054), 1102-1102.

27. Koech, P. K.; Zhang, J.; Kutnyakov, I. V.; Cosimbescu, L.; Lee, S. J.; Bowden, M. E.; Smurthwaite, T. D.; Heldebrant, D. J., Low viscosity alkanolguanidine and alkanolamidine liquids for CO_2 capture. *Rsc Advances* **2013,** *3* (2), 566-572.

28. Wang, C.; Luo, H.; Jiang, D.-e.; Li, H.; Dai, S., Carbon Dioxide Capture by Superbase-Derived Protic Ionic Liquids. *Angewandte Chemie-International Edition* **2010,** *49* (34), 5978-5981.

29. Zhu, X.; Song, M.; Xu, Y., DBU-Based Protic Ionic Liquids for CO_2 Capture. *ACS Sustainable Chemistry & Engineering* **2017,** *5* (9), 8192-8198.

30. Wang, C.; Luo, H.; Luo, X.; Li, H.; Dai, S., Equimolar CO_2 capture by imidazolium-based ionic liquids and superbase systems. *Green Chemistry* **2010,** *12* (11), 2019-2023.

31. Blath, J.; Deubler, N.; Hirth, T.; Schiestel, T., Chemisorption of carbon dioxide in imidazolium based ionic liquids with carboxylic anions. *Chem. Eng. J.* **2012,** *181*, 152-158.

32. Yu, B.; Zhang, H. Y.; Zhao, Y. F.; Chen, S.; Xu, J. L.; Hao, L. D.; Liu, Z. M., DBU-Based Ionic-Liquid-Catalyzed Carbonylation of o-Phenylenediamines with CO_2 to 2-Benzimidazolones under Solvent-Free Conditions. *ACS Catal.* **2013,** *3* (9), 2076-2082.

33. Lethesh, K. C.; Shah, S. N.; Mutalib, M. I. A., Synthesis, Characterization, and Thermophysical Properties of 1,8-Diazobicyclo[5.4.0]undec-7-ene Based Thiocyanate Ionic Liquids. *Journal of Chemical & Engineering Data* **2014,** *59* (6), 1788-1795.

34. Lethesh, K. C.; Shah, S. N.; Mutalib, M. I. A., Synthesis, characterization, physical and thermodynamic properties of diazobicyclo undecene based dicyanamide ionic liquids. *J. Mol. Liq.* **2015,** *208*, 253-258.

35. Wang, B.; Luo, Z.; Elageed, E. H. M.; Wu, S.; Zhang, Y.; Wu, X.; Xia, F.; Zhang, G.; Gao, G., DBU and DBU-Derived Ionic Liquid Synergistic Catalysts for the Conversion of Carbon Dioxide/Carbon Disulfide to 3-Aryl-2-oxazolidinones/[1,3]Dithiolan-2-ylidenephenyl- amine. *ChemCatChem* **2016,** *8* (4), 830-838.

36. Klamt, A., Conductor-like Screening Model for Real Solvents: A New Approach to the Quantitative Calculation of Solvation Phenomena. *The Journal of Physical Chemistry* **1995,** *99* (7), 2224-2235.

37. Klamt, A.; Jonas, V.; Bürger, T.; Lohrenz, J. C. W., Refinement and Parametrization of COSMO-RS. *The Journal of Physical Chemistry A* **1998,** *102* (26), 5074-5085.

38. Ahlrichs, R.; Bär, M.; Häser, M.; Horn, H.; Kölmel, C., Electronic structure calculations on workstation computers: The program system turbomole. *Chem. Phys. Lett.* **1989,** *162* (3), 165-169.

39. Schafer, A.; Klamt, A.; Sattel, D.; Lohrenz, J. C. W.; Eckert, F., COSMO Implementation in TURBOMOLE: Extension of an efficient quantum chemical code towards liquid systems. *PCCP* **2000,** *2* (10), 2187-2193.

40. Becke, A. D., Density-functional exchange-energy approximation with correct asymptotic behavior. *Physical Review A* **1988,** *38* (6), 3098-3100.

41. Perdew, J. P., Density-functional approximation for the correlation energy of the inhomogeneous electron gas. *Physical Review B* **1986,** *33* (12), 8822-8824.

42. Eckert, F.; Klamt, A., Fast solvent screening via quantum chemistry: COSMO-RS approach. *AlChE J.* **2002,** *48* (2), 369-385.

43. Gonzalez-Miquel, M.; Palomar, J.; Omar, S.; Rodriguez, F., CO_2/N_2 Selectivity Prediction in Supported Ionic Liquid Membranes (SILMs) by COSMO-RS. *Ind. Eng. Chem. Res.* **2011,** *50* (9), 5739-5748.

44. Palomar, J.; Gonzalez-Miquel, M.; Polo, A.; Rodriguez, F., Understanding the Physical Absorption of CO_2 in Ionic Liquids Using the COSMO-RS Method. *Ind. Eng. Chem. Res.* **2011,** *50* (6), 3452-3463.

45. Ge, L.; Zhu, Z.; Rudolph, V., Enhanced gas permeability by fabricating functionalized multi-walled carbon nanotubes and polyethersulfone nanocomposite membrane. *Sep. Purif. Technol.* **2011,** *78* (1), 76-82.

46. Kumazawa, H.; Wang, J. S.; Sada, E., Gas transport through homogeneous and asymmetric polyethersulfone membranes. *J. Polym. Sci., Part B: Polym. Phys.* **1993,** *31* (7), 881-886.

47. Yong, W. F.; Chung, T.-S.; Weber, M.; Maletzko, C., New polyethersulfone (PESU) hollow fiber membranes for CO_2 capture. *J. Membr. Sci.* **2018,** *552*, 305-314.

48. Tomé, L.; Marrucho, I., Poly(ionic liquid)s: Designing CO_2 Separation Membranes. In *Applications of Ionic Liquids in Polymer Science and Technology*, Mecerreyes, D., Ed. Springer Berlin Heidelberg: 2015; pp 267-295.

49. Socrates, G., *Infrared and Raman characteristic group frequencies: tables and charts*. 3rd ed.; Wiley: Chichester, New York, 2001.

50. Paschoal, V. H.; Faria, L. F. O.; Ribeiro, M. C. C., Vibrational Spectroscopy of Ionic Liquids. *Chem. Rev.* **2017,** *117* (10), 7053-7112.

51. Vyas, S.; Dreyer, C.; Slingsby, J.; Bicknase, D.; Porter, J. M.; Maupin, C. M., Electronic Structure and Spectroscopic Analysis of 1-Ethyl-3-methylimidazolium Bis(trifluoromethylsulfonyl)imide Ion Pair. *The Journal of Physical Chemistry A* **2014,** *118* (34), 6873-6882.

52. Vitucci, F. M.; Trequattrini, F.; Palumbo, O.; Brubach, J. B.; Roy, P.; Paolone, A., Infrared spectra of bis(trifluoromethanesulfonyl)imide based ionic liquids: Experiments and DFT simulations. *Vib. Spectrosc* **2014,** *74*, 81-87.

53. Maton, C.; De Vos, N.; Stevens, C. V., Ionic liquid thermal stabilities: decomposition mechanisms and analysis tools. *Chem. Soc. Rev.* **2013,** *42* (13), 5963-5977.

54. Hillesheim, P. C.; Singh, J. A.; Mahurin, S. M.; Fulvio, P. F.; Oyola, Y.; Zhu, X.; Jiang, D.-e.; Dai, S., Effect of alkyl and aryl substitutions on 1,2,4-triazolium-based ionic liquids for carbon dioxide separation and capture. *RSC Advances* **2013,** *3* (12), 3981-3989.

55. Lee, J. S.; Wang, X.; Luo, H.; Dai, S., Fluidic Carbon Precursors for Formation of Functional Carbon under Ambient Pressure Based on Ionic Liquids. *Adv. Mater.* **2010,** *22* (9), 1004-1007.

56. Paraknowitsch, J. P.; Zhang, J.; Su, D.; Thomas, A.; Antonietti, M., Ionic Liquids as Precursors for Nitrogen-Doped Graphitic Carbon. *Adv. Mater.* **2010,** *22* (1), 87-92.

57. Fredlake, C. P.; Crosthwaite, J. M.; Hert, D. G.; Aki, S. N. V. K.; Brennecke, J. F., Thermophysical Properties of Imidazolium-Based Ionic Liquids. *Journal of Chemical & Engineering Data* **2004,** *49* (4), 954-964.

58. Verma, Y. L.; Singh, R. K., Conformational States of Ionic Liquid 1-Ethyl-3-methylimidazolium Bis(trifluoromethylsulfonyl)imide in Bulk and Confined Silica Nanopores Probed by Crystallization Kinetics Study. *The Journal of Physical Chemistry C* **2015,** *119* (43), 24381-24392.

59. Wang, Z.; Li, Z.; Jin, Y.; Liu, W.; Jiang, L.; Zhang, Q., Organic superbase derived ionic liquids based on the TFSI anion: synthesis, characterization, and electrochemical properties. *New J. Chem.* **2017,** *41* (12), 5091-5097.

60. Cadena, C.; Anthony, J. L.; Shah, J. K.; Morrow, T. I.; Brennecke, J. F.; Maginn, E. J., Why Is CO_2 So Soluble in Imidazolium-Based Ionic Liquids? *J. Am. Chem. Soc.* **2004,** *126* (16), 5300-5308.

61. Robeson, L. M., Correlation of separation factor versus permeability for polymeric membranes. *J. Membr. Sci.* **1991,** *62* (2), 165-185.

62. Robeson, L. M., The upper bound revisited. *J. Membr. Sci.* **2008,** *320* (1–2), 390-400.

63. Grunauer, J.; Shishatskiy, S.; Abetz, C.; Abetz, V.; Filiz, V., Ionic liquids supported by isoporous membranes for CO_2/N_2 gas separation applications. *J. Membr. Sci.* **2015,** *494*, 224-233.

64. Moganty, S. S.; Baltus, R. E., Diffusivity of Carbon Dioxide in Room-Temperature Ionic Liquids. *Ind. Eng. Chem. Res.* **2010,** *49* (19), 9370-9376.

65. Koller, T. M.; Heller, A.; Rausch, M. H.; Wasserscheid, P.; Economou, I. G.; Fröba, A. P., Mutual and Self-Diffusivities in Binary Mixtures of [EMIM][$B(CN)_4$] with Dissolved Gases by Using Dynamic Light Scattering and Molecular Dynamics Simulations. *The Journal of Physical Chemistry B* **2015,** *119* (27), 8583-8592.

66. Kilaru, P. K.; Scovazzo, P., Correlations of Low-Pressure Carbon Dioxide and Hydrocarbon Solubilities in Imidazolium-, Phosphonium-, and Ammonium-Based Room-Temperature Ionic Liquids. Part 2. Using Activation Energy of Viscosity. *Ind. Eng. Chem. Res.* **2008,** *47* (3), 910-919.

67. Jeffrey Horne, W.; Shannon, M. S.; Bara, J. E., Correlating fractional free volume to CO_2 selectivity in [Rmim][Tf_2N] ionic liquids. *The Journal of Chemical Thermodynamics* **2014,** *77*, 190-196.

68. Camper, D.; Bara, J.; Koval, C.; Noble, R., Bulk-Fluid Solubility and Membrane Feasibility of Rmim-Based Room-Temperature Ionic Liquids. *Ind. Eng. Chem. Res.* **2006,** *45* (18), 6279-6283.

69. Thomas, C.; Milet, A.; Peruch, F.; Bibal, B., Activation of carbonyl bonds by quaternary ammoniums and a (Na+:crown-ether) complex: investigation of the ring-opening polymerization of cyclic esters. *Polymer Chemistry* **2013,** *4* (12), 3491-3498.

CHAPTER 4. NEW CLASS OF TYPE III POROUS LIQUIDS: A PROMISING PLATFORM FOR RATIONAL ADJUSTMENT OF GAS SORPTION BEHAVIOR

4.1 Publication Statement

A version of this chapter was originally published by Weida Shan, Pasquale F. Fulvio, Liyun Kong, Jennifer A. Schott, Chi-Linh Do-Thanh, Tao Tian, Xunxiang Hu, Shannon M. Mahurin, Huabin Xing, and Sheng Dai, in *ACS Applied Materials and Interfaces*. Reproduced in part with permission from:

Shan, W.; Fulvio, P. F.; Kong, L.; Schott, J. A.; Do-Thanh, C.-L.; Tian, T.; Hu, X.; Mahurin, S. M.; Xing, H.; Dai, S., New Class of Type III Porous Liquids: A Promising Platform for Rational Adjustment of Gas Sorption Behavior. *ACS Appl. Mater. Interfaces* **2018,** *10* (1), 32-36.

Jennifer A. Schott provided major contributions to this paper including sample characterization and data analysis for the ionic liquids and porous liquids, and writing. Co-author contributions are as follows: Weida Shan, Pasquale F. Fulvio, and Jennifer A. Schott wrote and edited the paper; Liyun Kong, Chi-Linh Do-Thanh, and Tao Tian synthesized the materials; Xunxiang Hu completed PALS; Shannon M. Mahurin assisted with X-ray and microscopy; Huabin Xing and Sheng Dai discussed the results and edited the paper.

4.2 Abstract

Porous materials have already manifested their unique properties in a number of fields. Generally, porous materials are in a solid state rather than liquid, in which molecules are closely packed without porosity. “Porous” and “liquid” seem like antonyms. Herein, we report a new class of Type III porous liquids based on rational coupling of microporous framework nanoparticles as porous hosts with a bulky ionic liquid as the fluid media. Positron annihilation lifetime spectroscopy (PALS) and CO_2 adsorption measurements

confirm the successful engineering of permanent porosity into these liquids. Compared to common porous solid materials, as-synthesized porous liquids exhibited pronounced hysteresis loops in the CO_2 sorption isotherms even at ambient conditions (298 K, 1 bar). The unique features of these novel porous liquids could bring new opportunities in many fields including gas separation and storage, air separation and regeneration, gas transport, and permanent gas storage at ambient conditions.

4.3 Introduction

Porosity is normally considered a central feature of porous solids such as metal-organic frameworks (MOFs), zeolites, and porous carbon.[1-3] These solid materials with high porosity and diverse functionality have shown great potential in numerous applications including gas separation and storage[3-4], catalysis[5], sensors[6], energy conversion and storage[7]. However, the solid nature of these materials limits their further processing and integration into conventional flow processes.[8-10] In contrast, conventional liquids with high fluidity are generally considered non-porous or merely having transient porosity with small pores generated between the molecules due to random thermal motion.[11-12] Porous liquids have only recently been successfully synthesized[2, 11] and can be regarded as a new, emerging class of porous materials that couple the features of porous solids such as permanent porosity and molecular sieving with the fluidity and fast mass transfer of liquids. As a result, such porous materials are of great interest because of their unique physicochemical characteristics that can offer great opportunities in the development of size-selective adsorption and storage, homogeneous catalysis, and novel reaction media.[2, 9-10]

Porous liquids have been categorized into three types by James et al.[1]: Type I are neat liquids with constituent molecules that maintain permanent pores in the liquid state; Type II are essentially empty molecular hosts that are dissolved in a solvent where the solvent molecules are sterically hindered to occupy the molecular host cavity; Type III refer to porous framework materials that are dispersed in a in the fluid media where the

fluid molecules are excluded from the pore networks. However, only a few successful examples of porous liquids have been reported. The first example of a Type II porous liquid was synthesized by Cooper et al.[2] where a tetrahedral organic imine cage functionalized with six crown ether substituents was dissolved into the sterically hindered solvent, 15-crown-5, forming a Type II porous liquid. This porous liquid possessed permanent porosity (ca. 5 Å) substantially enhancing the solubility of methane molecules compared to that of the pure solvent. Additionally, successful preparation of a Type I porous liquid was achieved by Dai et al.[11] via rational surface engineering of hollow silica spheres with ionic attachment of suitable ionic corona and canopy species resulting in accelerated gas diffusion because of the hollow cavities. Moreover, Wang et al.[13] reported a slurry system that can be synthesized by suspending zeolitic imidazolate framework-8 (ZIF-8) nanoparticles in bulky organic solvent where the pore channels can remain empty in the slurry state, which can be classified into Type III porous liquids. In spite of some remarkable properties, these materials still have important issues such as limited types of porous liquids due to complex synthesis route, easy collapse or decomposition of organic porous hosts, and difficulties in functionalizing porous liquids, which could impede further development.

4.4 Experimental

4.4.1 Materials Characterization

Herein, we report a new family of Type III porous liquids that can be facilely synthesized by a simple solution mixing of suitable porous hosts and rationally designed ionic liquids (ILs). Two common types of porous framework materials, metal-organic framework (ZIF-8) and zeolite (ZSM-5, Silicalite-1), with well-defined microporous networks that could block bulky solvent molecules were prepared and adopted as the porous hosts (see Supporting Information for details). ZIF-8 is a thermally and chemically stable MOF in which zinc ions are tetrahedrally coordinated by the nitrogen atoms from 2-methylimidazolate in a sodalite (SOD) topology, and thus possess large SOD cages (~11.6

Å) connected with a small flexible cage window (~3.4 Å).[4, 14] ZSM-5, a typical zeolite, has well-defined micropores with sinusoidal channels of 0.55 nm x 0.51 nm and straight channels of 0.56 nm x 0.53 nm, and has been widely used as solid catalyst in various industry processes.[5, 15] An all-silica version of ZSM-5, Silicalite-1, with similar channel dimensions of 0.51 nm x 0.56 nm and 0.53 nm x 0.56 nm was also synthesized and used as the porous host.[16]

To maintain permanent, accessible porosity within these frameworks, it is essential to prevent the solvent molecules or ions from accessing the pore channels within the frameworks while simultaneously maintaining a stable and uniform dispersion of the porous framework nanoparticles in the solvent without any aggregation. Toward this end, ionic liquids (ILs) are excellent candidates for fabricating porous liquids due to their unique properties such as negligible vapor pressure, tailored ion structure, and good capability of dissolving various organic/inorganic materials.[17-18] Therefore, through rational design and judicious selection, the [DBU-PEG][Tf_2N]$_2$ IL, **Figure 4-1**, was synthesized and employed as the fluid solvent. To more precisely characterize the structure of the IL, the lowest-energy conformation for the ion pair was calculated at the B3LYP/6-31+G (d, p) level, as shown in **Figure 4-1 b**. This specific [DBU-PEG]$^{2+}$ cation (molecular size of ca. of 1.9 nm x 0.77 nm x 0.40 nm) with bulky cationic heads is much larger than the channel dimensions of the porous frameworks, and thus can be completely blocked from entering the pores through size exclusion.

Experimentally, the porous framework nanoparticles dispersed into the ionic liquid (see Supporting Information for synthesis details) can create stable and homogeneous porous liquids at room temperature. **Figure 4-2** illustrates the formation of ZIF-8-based porous liquids. The resultant porous liquids are extremely stable over long time periods without any aggregation because of the formation of stable chemical bonding between the solvent ions and solute nanoparticles at the solute-solvent interface.[19] For example, the

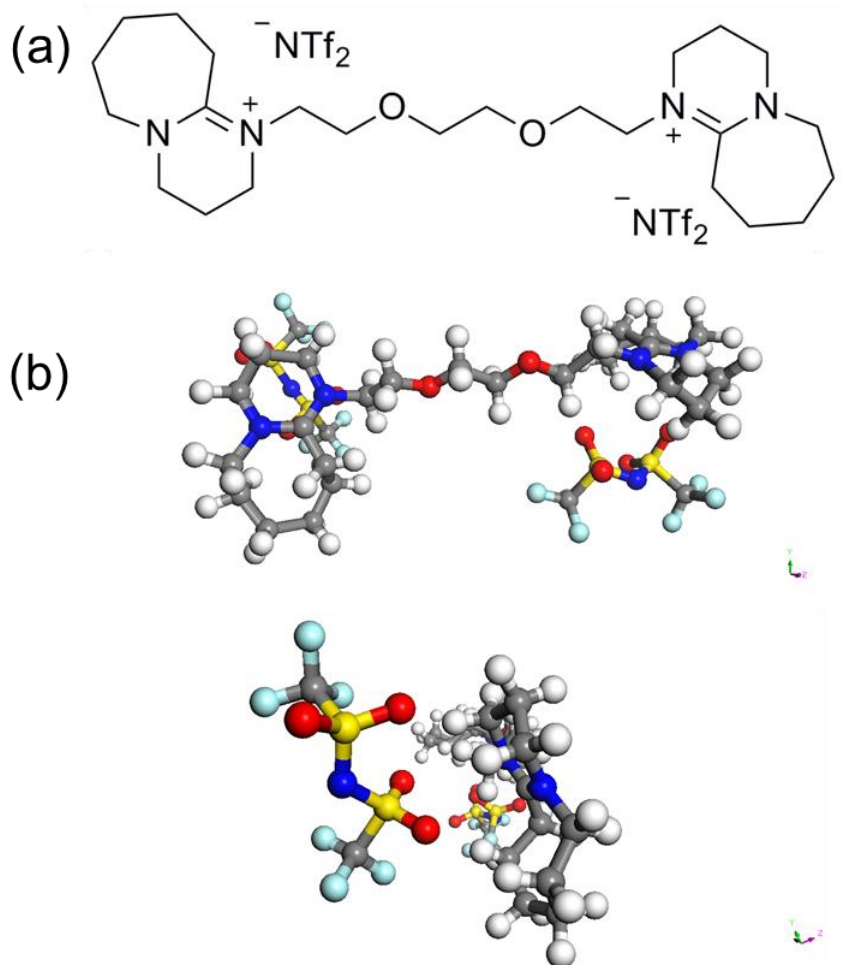

Figure 4-1. a) molecular formula of [DBU-PEG][Tf_2N]$_2$ ILs and b) top- and side- view of optimized molecular conformation of [DBU-PEG][Tf_2N]$_2$ ILs at the B3LYP/6-31+G(d, p) level

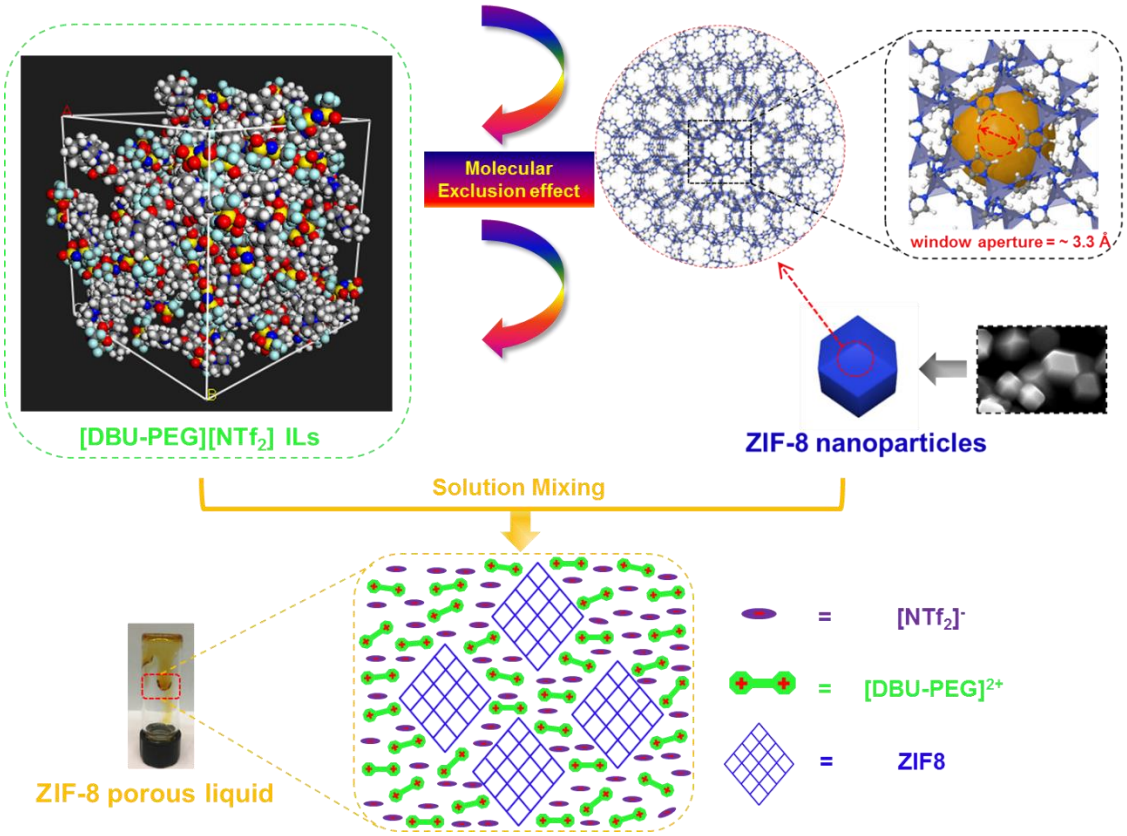

Figure 4-2. A Schematic illustration of the formation of ZIF-8 porous liquids

electron-rich nitrogen atoms on the cation can interact with the exposed Zn^{2+} atoms on the surface of the ZIF-8 nanoparticles, promoting the formation of a stable and homogeneous nanoparticle suspension. To obtain a precise mass ratio of porous host to fluid solvent, thermogravimetric analysis (TGA) was used to determine the final content of porous framework solids in the porous liquids. The porous liquids are denoted by the porous host name and its corresponding mass fraction in the porous liquids. For example, ZIF-8 porous liquid (3.2 wt%) (denoted as ZIF-8-PL (3.2 wt%)) represent a porous liquid in which the mass fraction of ZIF-8 nanoparticles in the ZIF-8/[DBU-PEG][Tf_2N]$_2$ liquid nanocomposite is 3.2%.

Positron annihilation lifetime spectroscopy (PALS) was used to investigate the permanent cavities in the porous liquids. PALS is an *in-situ* pore-/void-volume characterization technique where the ortho-positronium (o-Ps), a parallel spin complex of a positron and an electron, can be generated within low electron density regions of the insulating material such as empty cavities by exposing the material to a positron source such as ^{22}Na.[20-21] The o-Ps lifetime for the ZIF-8 porous liquid (3.2 wt%) extracted from the measured positron lifetime spectrum, **Figure 4-3**, is ~2.21 ns, equivalent to an average cavity diameter of 6.1 Å between the size of the window aperture (3.4 Å) and SOD cage (11.6 Å), implying that permanent micropores have been successfully incorporated into the liquid-state.

Density measurements of the samples were completed using a custom-made pycnometer, created from a cut-off EPR tube that was calibrated with a variety of known liquids (deionized water, density standards, common ILs). During calibration, the volume of the cell was determined to be ~60 microliters with a volume uncertainty of less than 1 microliter (1.48% variability). This variation can be attributed to the difficulty of obtaining a perfect fill without a displacement cap such as those provided with commercially available pyncometers. Calibration checks were completed with commercially available ILs and values matched literature values within 1.2 % error.

Density values, the arithmetic average and standard deviations from 5 replicate

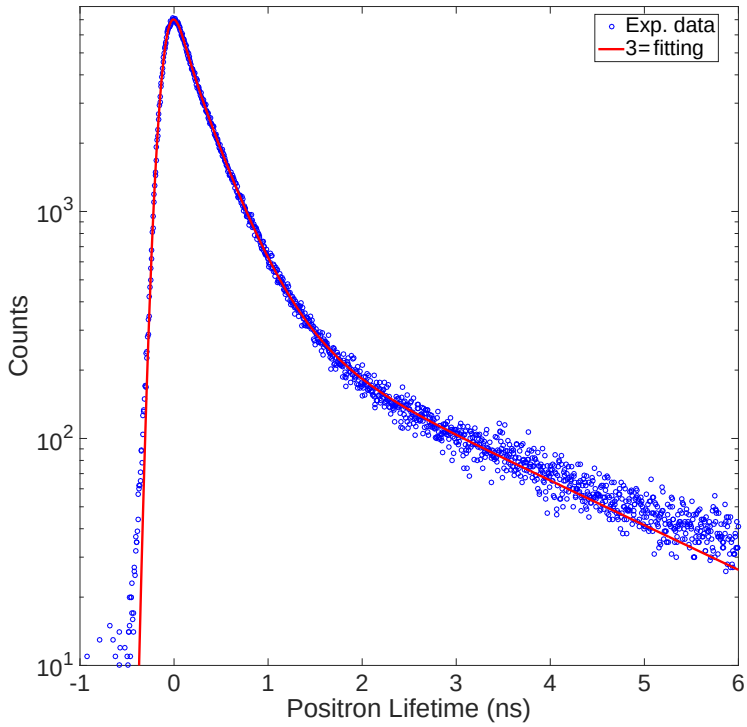

Figure 4-3. Positron annihilation lifetime spectroscopy (PALS) of ZIF-8 porous liquid (9.1 wt%). The annihilation lifetime of o-Ps (refer to the period between the generation and annihilation of o-Ps) can be correlated to the average pore size in the materials by the Tao-Eldrup model as following:

$$\tau_3 = 0.5 \times \left[1 - \frac{R}{R + \Delta R} + \frac{1}{2\pi} \sin\left(\frac{2\pi R}{R + \Delta R}\right)\right]^{-1}$$

Where τ_3 refer to the o-Ps lifetime (ns), and ΔR is the empirical electron thickness that is generally taken to be 1.66 Å.

measurements, for the new ILs and PLs are presented in **Table 4-1.** A significant decrease in density is seen for the porous liquids, which can be attributed to the successful incorporation of free volume in the liquid phase. The magnitude of density change seen here is far greater than values reported by Gomes and coauthors who suspended ZIF-8 in a common phosphonium ionic liquid.[22] The long chain phosphonium cations $[P_{6,6,6,14}]^+$ are likely incorporated into the framework to varying degree, as represented in simulations by the same group. The significant density changes in the ZIF-8-PLs with respect to pure [DBU-PEG][Tf_2N]$_2$ confirms the exclusion of the IL from the ZIF-8 pores.

4.5 Results and Discussion

For preliminary trials, two different ionic liquids were tested as the fluidic precursor. The common 1-butyl-3-methylimidazolium bis(trifluoromethylsulfonyl)imide, [Bmim][Tf_2N], and the new 8,8′-(3,6-dioxaoctane-1,8-diyl)bis(1,8-Diazabicyclo[5.4.0]undec-7-en-8-ium) bis(trifluoromethanesulfonyl)imide, [DBU-PEG][NTf_2]$_2$, were chosen as suitable candidates since their ionic diameters exceed the size of the cavity windows in the porous substrates. Therefore, it was expected that the ionic liquids would be completely excluded from the pore network. Porous liquids were obtained by independently mixing each of the three porous hosts ZIF-8, ZSM-5, and Silcalite-1 with the respective ILs in a similar mass ratio.

To further assess the potential permanent cavities in the porous liquids, CO_2 adsorption-desorption measurements were carried out at ambient temperature as shown in **Figure 4-4**. Pronounced enhancement of CO_2 adsorption capacities were detected for all three [DBU-PEG][NTf_2]$_2$-based porous liquids compared to the pure IL, whereas little change in CO_2 adsorption capacity was observed for the [Bmim][Tf_2N]-based liquid analogues. Such significant differences can be attributed to the fact that the small-sized $[Bmim]^+$ cation can pass through the window apertures of the porous hosts and occupy the cavities, whereas the bulky $[DBU\text{-}PEG]^{2+}$ cations are excluded from the pores, thus

Table 4-1. Summary of high-pressure experimental and theoretical CO_2 adsorption capacities for as-synthesized porous liquids, pure IL, and porous solids

	porous particle content (wt%)	Density (g/mL)	N_2 capacity (mmol/g) 8 bar, 298 K	CO_2 capacity (mmol/g) 10 bar, 298 K		
				Exp.	Theo.	$\%_{theo}$
ZIF-8-PL	3.2	1.43	-	0.50	0.52	95%
	10.0	1.39	-	0.81	0.91	88%
	20.0	1.34	-	1.17	1.48	79%
	30.0	1.29	0.04	1.57	2.05	76%
ZSM-5-PL	5.4	-	-	0.46	0.48	96%
Silicalite-1-PL	2.1	-	-	0.38	0.39	99%
[DBU-PEG][Tf_2N]$_2$	0	1.45	-	0.34	-	-
ZIF-8	100	0.35	1.16	6.04	-	-
ZSM-5	100	1.78	0.83	2.80	-	-
Silicalite-1	100	1.76	0.62	2.30	-	-

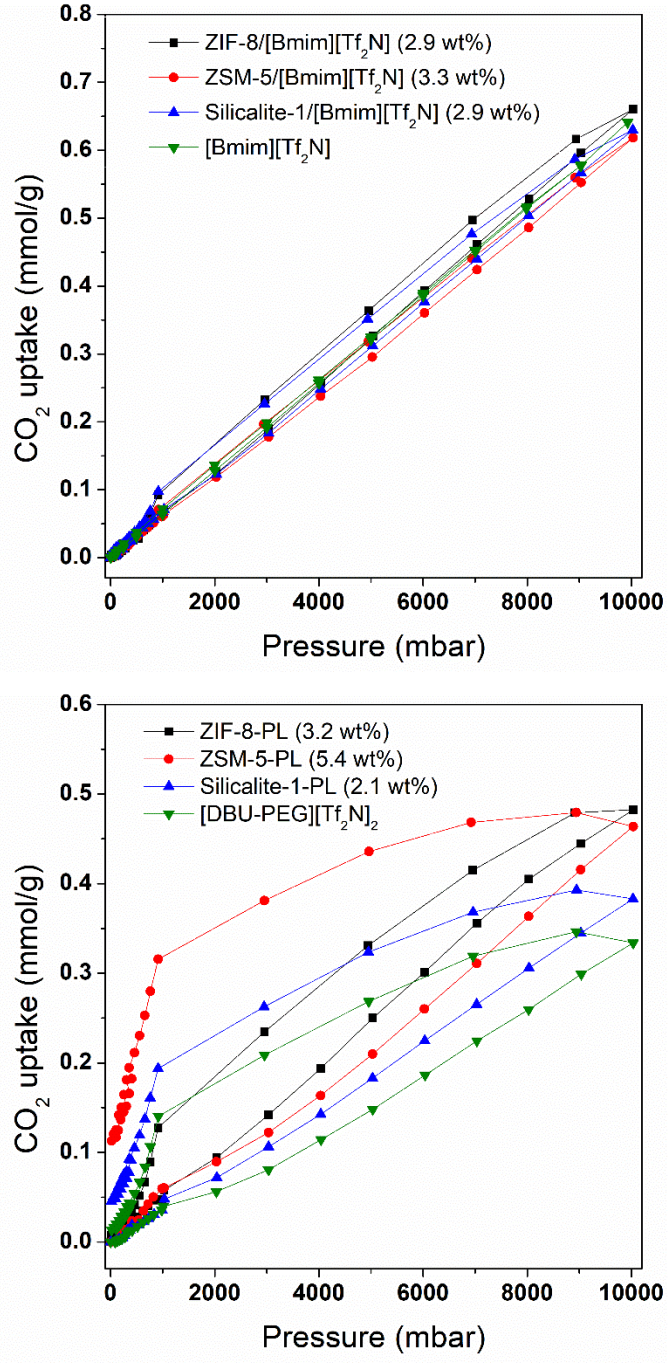

Figure 4-4. High-pressure CO_2 adsorption-desorption isotherms at 298 K of ZIF-8, ZSM-5, and Silicalite-1 incorporated into: a) [Bmim][Tf_2N] based liquid mixtures with pure [Bmim][Tf_2N] included for comparison, b) [DBU-PEG][Tf_2N]$_2$ based porous liquids, with pure [DBU-PEG][Tf_2N]$_2$ IL included for comparison.

preserving the micropores and providing extra CO_2 adsorption sites. Intuitively, ZIF-8, with a pore size of ~3.4 Å that is smaller than the reported ionic diameter of $[Bmim]^+$ (6.6 Å),[23-24] should also exclude the [Bmim][Tf_2N] IL from the pore network; however, recent reports[25-27] of successful incorporation of [Bmim]-based ILs into the cage space of ZIF-8 frameworks which are supposed to arise from a combination of the conformation transition of the $[Bmim]^+$ cation and the flexible pore architecture of ZIF-8, are in good agreement with the almost invariant CO_2 adsorption results observed in the [Bmim][Tf_2N]-based liquid mixtures.

Moreover, it can be seen that under the same content of porous framework solids, ZIF-8 porous liquids could exhibit the highest enhancement of CO_2 adsorption capacity among these porous liquids. This is likely due to the fact that the ZIF-8 has the highest CO_2 capacity due to the largest microporous surface area (1297 m^2/g) and largest micropore volume (0.58 cm^3/g) among the three porous hosts, most of which is preserved in the ionic liquid media and functions as active CO_2 adsorption sites. **Figure 4-5** and **Table 4-2** contain additional porosity properties of the three microporous materials. Both ZSM-5 and Silicalite-1 perform quite well, even with smaller micropore surface area and volume.

ZIF-8 was chosen for additional study, due to its potential to reach the highest overall capacity. Subsequently, the porous liquid concentration was further examined by varying the ratio of microporous particles in relation to the fluid media. Nanoparticle content was gradually increased to a maximum of 30 wt% in the porous liquids which correlates to the enhancement of CO_2 sorption is seen in **Figure 4-6.** From the isotherms, it can be seen that the ZIF-8-PL (30 wt%) sample exhibits the highest CO_2 adsorption capacity (1.54 mmol/g), which is approximately 4.7 times the CO_2 adsorption capacity of pure [DBU-PEG][Tf_2N]$_2$ IL. When weighted to the amount of microporous material in the porous liquids, the CO_2 uptake is comparable to that of pristine solids. Theoretical CO_2 capacities for porous liquids were calculated by the following equation:

$$n_{PL} = \omega_{IL} n_{IL} + \omega_{NP} n_{NP}$$

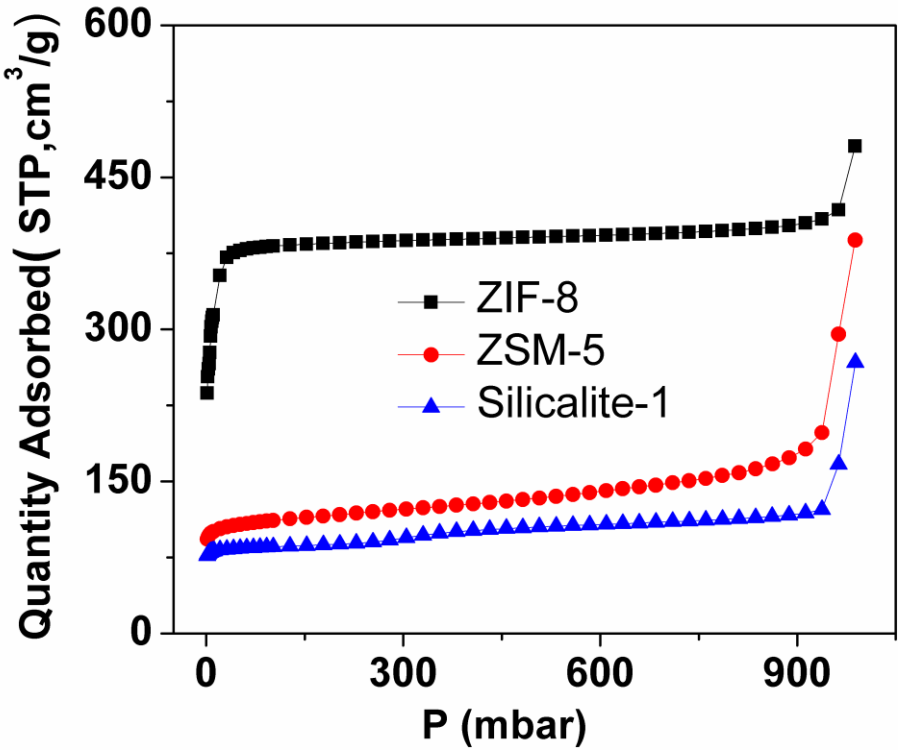

Figure 4-5. N_2 adsorption isotherms (77 K) for the as-synthesized porous framework solids

Table 4-2. Textural Properties of as-synthesized porous frameworks

	S_{BET}[a] (m^2g^{-1})	S_m[b] (m^2g^{-1})	V_t[c] (cm^3g^{-1})	V_m[d] (cm^3g^{-1})
ZIF-8	1335	1297	0.72	0.58
ZSM-5	408	289	0.57	0.13
Silicalite-1	304	208	0.38	0.10

[a] Surface area calculated from the BET equation in the relative pressure range of 0.05–0.20. [b] Micropore surface area calculated using the t-plot method. [c] Single point total pore volume calculated at a relative pressure of 0.97. [d] Micropore volume calculated by the t-plot method

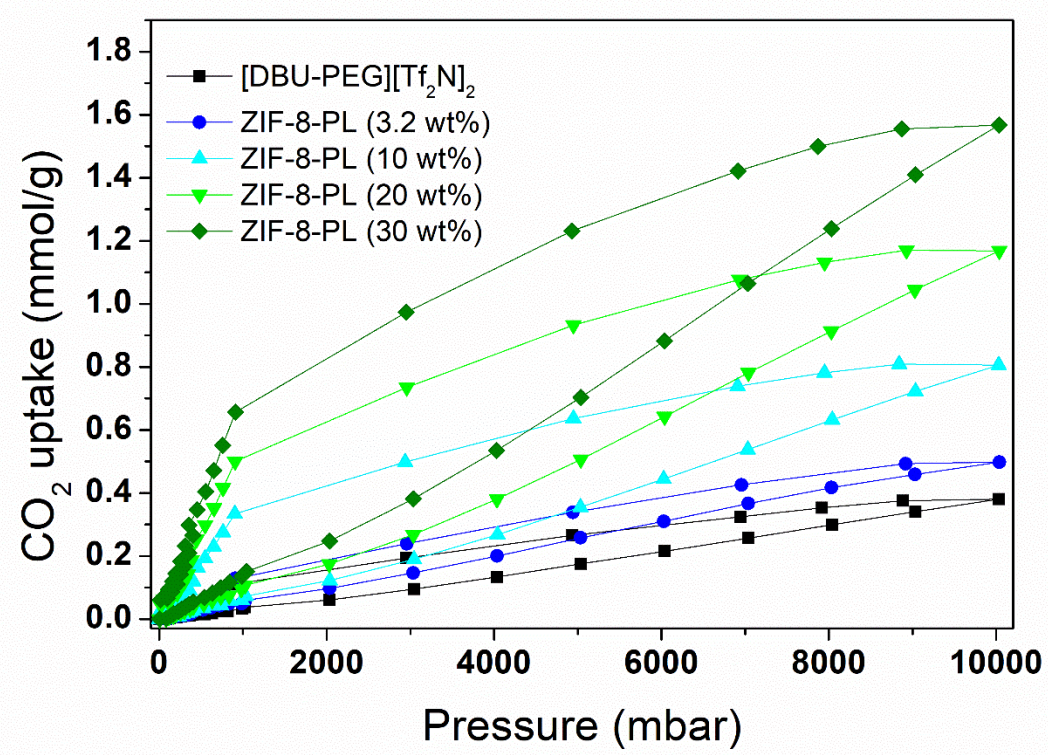

Figure 4-6. CO_2 adsorption-desorption isotherms of ZIF-8 porous liquids at 25 °C, [DBU-PEG][Tf_2N]$_2$ IL included for comparison.

where ω_{IL} and ω_{NP} refer to the mass content of ILs and microporous nanoparticles in the porous liquids, and n_{IL} and n_{NP} are the experimental CO_2 adsorption capacities at 10 bar (**Figure 4-4 & 4-7)** for the pure IL and microporous solid nanoparticles, respectively. The experimentally determined capacities are quite similar the theoretical values, especially at low concentrations (**Table 4-1**). The deviations at higher concentration arise from the slow equilibration of the gas transport from the liquid phase into the porous particles. The CO_2 adsorption capacities of these porous liquids can be correlated with the mass content of the microporous nanoparticles, indicating that facile adjustment of gas adsorption performance can be achieved by altering the mass ratio of the microporous nanoparticles to ILs.

The CO_2 desorption isotherms were also measured and are summarized in **Figure 4-4** and **Figure 4-6**. The slight increase in gas uptake during desorption process may result from buoyancy effects due to changes in the density or swelling of the porous liquids during the CO_2 adsorption step. In contrast to the highly reversible Type-I isotherms observed in the pure porous solids (see **Figure 4-7**) and the slight hysteresis loop on the pure [DBU-PEG][Tf_2N]$_2$ ILs, the [DBU-PEG][Tf_2N]$_2$-based porous liquids exhibit marked desorption hysteresis loops indicating that the adsorbed CO_2 molecules are not immediately released as the pressure was reduced and remain trapped in the ionic liquid matrix and the vacant pore channels within the porous liquids. This is mostly likely due to a combination of stronger interaction of the former with CO_2 and CO_2-accessible micropores residing in the porous liquids. To the best of our knowledge, such broad sorption hysteresis has not been previously observed in pure imidazolium-based ionic liquids,[28-29] or for the solid microporous sorbents tested, with exception of few sorbents with flexible pores.[30-32] This suggests the possibility of bestowing various MOFs or zeolites with rigid frameworks hysteresis desorption behavior while retaining their intrinsic microporous network. Electron microscopy was used to further characterize the microscopic structure of the porous framework nanoparticles and porous liquids, and the results are summarized in **Figure 4-8** and supporting information **Figures 4-13** through **4-15.**

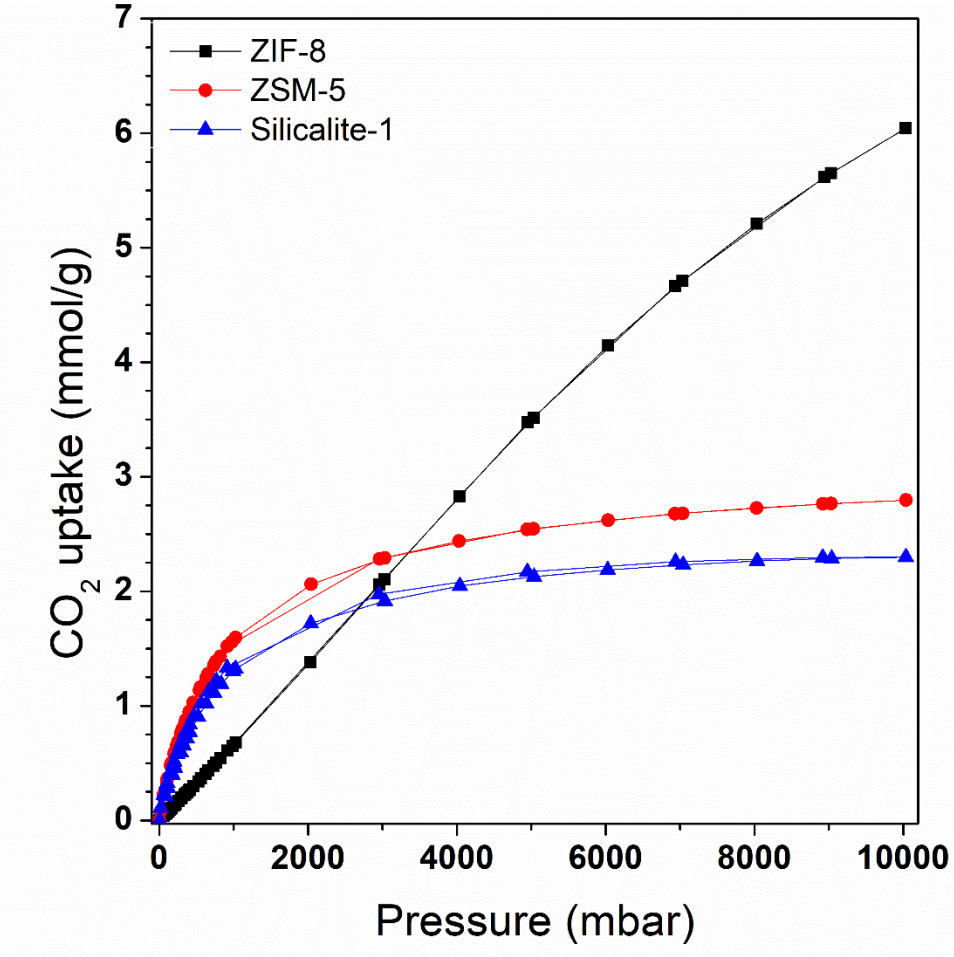

Figure 4-7. High-pressure (10 bar) CO_2 adsorption-desorption isotherms for pure framework solids.

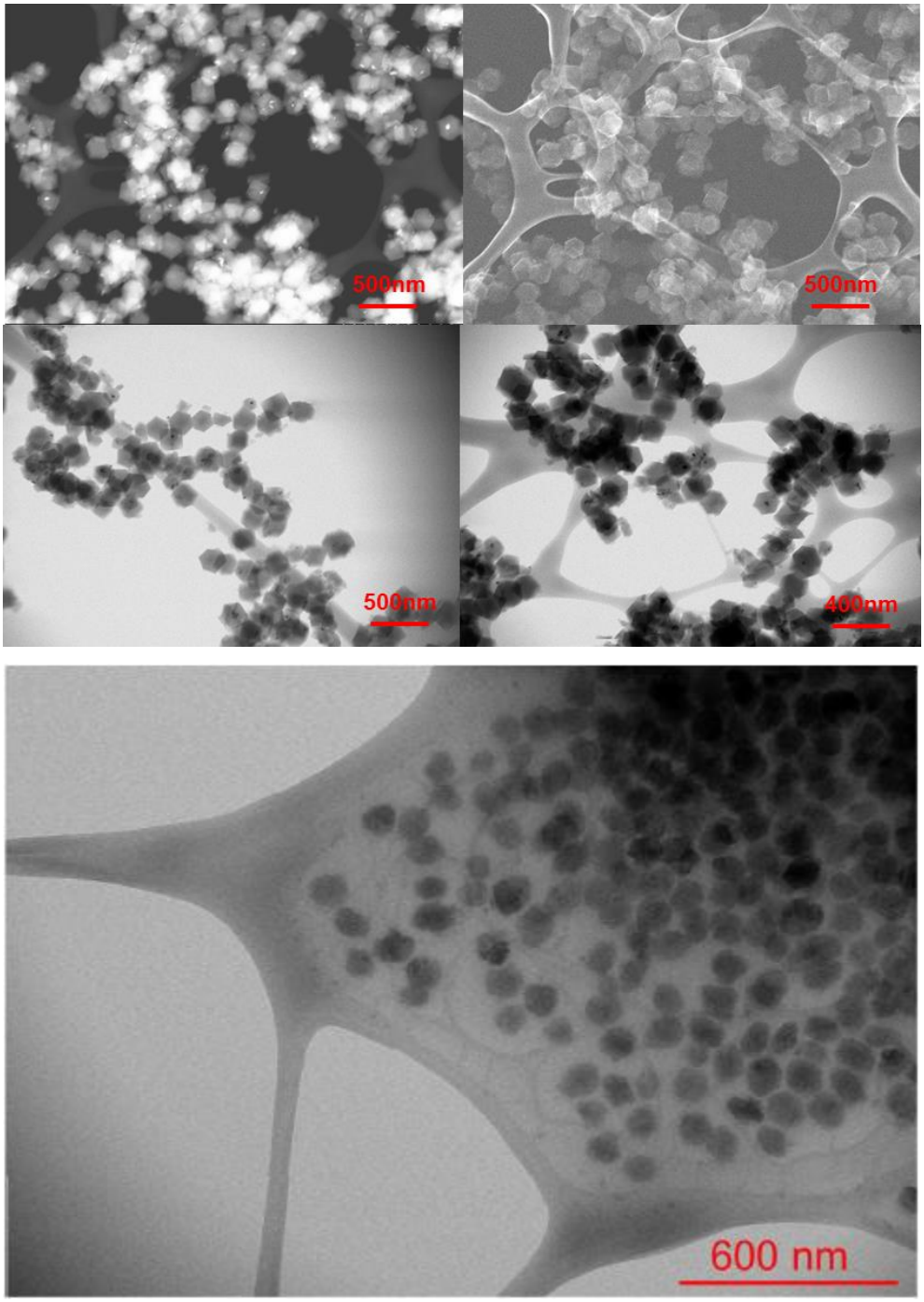

Figure 4-8. TEM images of a) as-synthesized ZIF-8 nanoparticles, and b) as-synthesized ZIF-8 porous liquids (30 wt%)

The differences in absorption above 1 bar are likely due to the multifaceted chemical domains in this system. At relatively low pressure, the CO_2 is quickly sorbed into the liquid phase and transported into the vacant porous materials due to a large concentration gradient in which the ZIF-8 acts as a trap quickly removing the first volumes of CO_2 dosed into the system. However, at higher pressures are thermodynamically limited by both porous liquid components. The sorption into the ionic liquid slows due to a smaller gradient since the initial CO_2 likely adsorbs to the ZIF-8 apertures prior to filling the cavities, retarding the further sorption of gases into the structure. There could also be effects imparted from a solvation shell or immobilized layer of IL on or near the surface of the porous particles.

While enhancing capacity is important, it is not the only factor. In real separations a mixture of gases will need to be isolated, requiring a selective sorbent. Here, ideal selectivity values were calculated from the single gas solubilities at various pressures. The nitrogen solubility in the pure ILs and the low concentration porous liquids is below the detection limit of the instrument, so selectivity values for these materials could not be determined. However, results for ZIF-8 and ZIF-8-PL (30 wt%) are plotted in **Figure 4-9**. The carbon dioxide to nitrogen selectivity of pure ZIF-8 is only 4 but is increased to an average of about 25 for the 30 wt% porous liquid. This accounts for an enhancement of approximately 6 times the selectivity of the solid porous precursor. Not only has the addition of porous materials enhanced the capacity of the liquid, the liquid has increased the selectivity of the porous materials. So, while neither capacity or selectivity alone is greater than the sum of its precursors, the composite of these two materials is synergistic in its combined features.

4.6 Conclusions

In summary, we report a new family of Type III porous liquids that can be facilely synthesized by rational combination of suitable porous frameworks (ZIF-8, ZSM-5, and

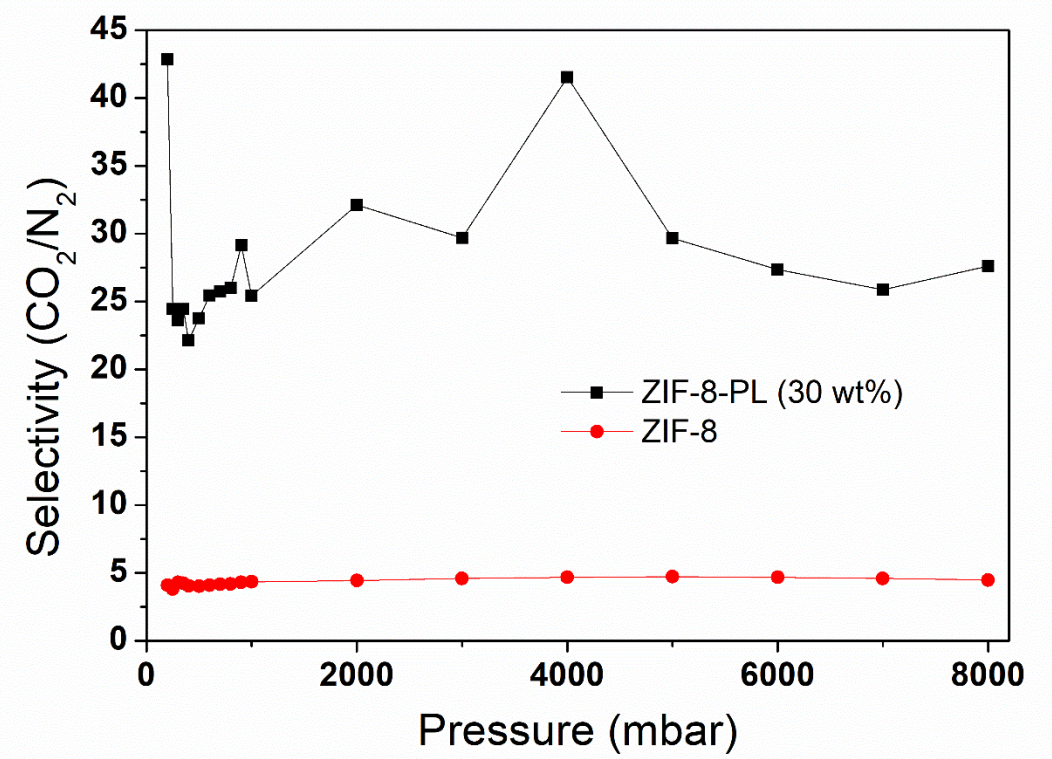

Figure 4-9. Selectivity values for the 30 wt% porous liquid show significant enhancement over those of pure ZIF-8

Silicalite-1) with a bulky ionic liquid ([DBU-PEG][Tf_2N]$_2$ IL). The existence of permanent porosity in these porous liquids was confirmed by PALS and CO_2 sorption measurements. The porous liquids exhibit tailorable and enhanced CO_2 adsorption capacities due to the successful preservation of intrinsic porosity of the microporous ZIF-8, ZSM-5 and Silicalite-1 nanoparticles. Notably, pronounced hysteresis loops in the CO_2 desorption were observed for these porous liquids at ambient conditions. This combination of the tailorable adsorption and hysteresis desorption behavior of these porous liquids demonstrate their potential as a new platform to rationally control or gate the gas sorption behavior in porous liquids. Therefore, fluid sorbents with CO_2 hysteresis effect are desirable for safe, short and long-term storage, and transportation. While the nanoparticles allow for high CO_2 adsorption capacity, the selected ionic liquid displays high CO_2 selectivity and negligible permeability for N_2 which is highly desirable for carbon sequestration in industrial gas emissions.

The intrinsic pore channels and active functional sites such as uncoordinated metal sites and basic amino groups in the porous hosts can be preserved even after fabrication into porous liquids. Furthermore, fine control of thermodynamic factors such as adsorbate concentration and kinetic factors such as diffusion rate, two vital factors that influence the adsorption behavior of porous materials, could be achieved through rational selection of suitable ionic liquid as the fluid solvent. Such novel porous liquids could bring new opportunities in many fields including gas separations and storage, air regeneration, gas transport, and permanent storage at ambient conditions. Additionally, given the vast number of microporous framework materials and nearly infinite ionic liquids species, a series of Type III porous liquids can be rationally designed and fabricated in the future, opening up new opportunities in many important domains.

4.7 Supporting Information

4.7.1 Chemicals and Reagents

Tetraethyl orthosilicate (98%), aluminum isopropoxide (99.99%), tetrapropylammonium hydroxide (1 M aqueous solution), 2-methylimidazole (99%), ZnO nanoparticles, triethylene glycol, 1,8-diazabicyclo[5.4.0]undec-7-ene (98%), *p*-toluenesulfonyl chloride (99%) were all purchased from Aldrich. Potassium hydroxide powder, lithium bis(trifluoromethanesulfonyl)imide ($LiNTf_2$) were purchased from Fischer Scientific. Common solvents, reagents, and chemicals were purchased from other commercial vendors and used without further purification.

4.7.2 Analytical Techniques

^{1}H and ^{13}C NMR spectra were recorded at ambient temperature on a Varian VNMRS 500 MHz narrow-bore broadband system. ^{1}H and ^{13}C NMR chemical shifts were referenced to the residual solvent.

Mass spectrometry analyses were performed using a QSTAR Elite quadrupole time-of-flight (QTOF) mass spectrometer with an electrospray ionization source from AB Sciex (Concord, Ontario, Canada).

The N_2 sorption isotherms at 77 K were measured on a Micromeritics Gemini 2390t system to determine the textural properties of synthesized porous solids. Before gas measurement, the ZIF-8 samples were pretreated at 200 °C under flowing N_2 for 12 h, and the ZSM-5 and Silicalite-1 samples were pre-treated at 300 °C under flowing N_2 for 12 h. The total surface area was calculated from the N_2 adsorption isotherms using the BET equation in the relative pressure range of 0.05–0.20.

Scanning electron microscope (SEM) images were taken on a Zeiss Auriga Crossbeam SEM at an acceleration voltage of 5 kV. Transmission scanning electron microscope (STEM) images were acquired with a Hitachi HD-2000 operating at 200 kV.

Powder X-ray diffraction (XRD) patterns were collected on a PANalytical Empyrean diffractometer with Ni-filtered Cu Kα (λ = 1.54 A) radiation operating at 45 kV and 40 mA.

CO_2 absorption measurements were acquired using an Intelligent Gravimetric Analyzer (Hiden Isochema, UK). Approximately 50 mg of sample was loaded into a quartz holder and evacuated to 5 mbar at 60 °C to degas and dry the sample. The mass uptake (corrected for buoyancy) was then measured as a function of pressure up to a final pressure of 10 bar. The temperature was controlled by a recirculating bath.

4.7.3 Positron Annihilation Lifetime Spectroscopy (PALS)

The sample was measured at room temperature, using a conventional sample-source-sample sandwich geometry. The positron source (20μCi) was made from a ^{22}NaCl solution evaporated onto the surface of the sample placed on a thin Al foil. Then the sample placed on the other Al foil will cover the sample with positron source with the objective of containing all emitted positrons within the sample. The 1.274 MeV gamma ray indicates a positron emission event, and the 0.511 MeV annihilation gamma rays were detected using a fast scintillator (BaF_2), coupled with photomultiplier tubes (PMT). Different from the traditional experimental setup, a double-stop setup[33] was employed in this work, as shown in Scheme S1. A pair of 0.511 MeV gamma rays is detected by two PMTs which are placed face to face on the opposite sides of the source-sample assembly. The positron lifetime is defined as the average value of the time intervals between the birth gamma ray and the two annihilation gamma rays for a coincidence event. Data were obtained using a digital oscilloscope with a timing resolution of 199 ps.

4.7.4 Synthesis of Ionic Liquids, Porous Materials, and Porous Liquids

1,8-ditosyl-3,6-dioxaoctane ($TsPEG_{150}Ts$) (1) To a solution of triethylene glycol (5.72 g, 38.07 mmol) in dichloromethane (40 mL) was added *p*-toluenesulfonyl chloride (14.52 g, 76.14 mmol), and the mixture was cooled to 0 °C. While stirring, potassium

hydroxide powder (17.09 g, 304.56 mmol) was added in portions. The reaction continued stirring and was allowed to warm to room temperature overnight. Deionized water (80 mL) was then added, and the mixture was extracted with chloroform (2 × 50 mL). The combined chloroform extracts were dried over magnesium sulfate, filtered, concentrated, and dried under vacuum to give **1** as an off-white solid (16.99 g, 97%).Characterizations matched those reported in the literature.[34-35]

^{1}H NMR ($CDCl_3$, 500 MHz) δ 7.78 (d, J = 8.4 Hz, 4H), 7.34 (d, J = 7.9 Hz, 4H), 4.15–4.12 (m, 4H), 3.66–3.63 (m, 4H), 3.52 (s, 4H), 2.44 (s, 6H). ^{13}C NMR ($CDCl_3$, 126 MHz) δ 145.0, 133.2, 130.0, 128.1, 70.9, 69.4, 68.9, 21.8.

8,8′-(3,6-dioxaoctane-1,8-diyl)bis(1,8-Diazabicyclo[5.4.0]undec-7-en-8-ium) ditosylate (TsODBUPEG$_{150}$DBUOTs) (2) Following a modified general procedure from the literature,[36] 1,8-diazabicyclo[5.4.0]undec-7-ene (DBU) (1.80 mL, 11.80 mmol) was added to a solution of **1** (2.39 g, 5.22 mmol) in dry toluene (20 mL), and the mixture was stirred at 115 °C under N_2 for 24 h. After cooling to room temperature and storing at −10 °C overnight, the excess toluene layer was decanted. The oily residue was then washed with dry ethyl ether (3 × 15 mL) and dried under vacuum to afford **2** as a dark yellow viscous oil (3.36 g, 84%).

^{1}H NMR (DMSO-d_6, 500 MHz) δ 7.48 (d, J = 8.0 Hz, 4H), 7.12 (d, J = 7.8 Hz, 4H), 3.71 (t, J = 5.2 Hz, 4H), 3.63–3.59 (m, 4H), 3.58–3.50 (m, 8H), 3.48–3.43 (m, 8H), 2.87–2.83 (m, 4H), 2.29 (s, 6H), 1.94 (t, J = 5.2 Hz, 4H), 1.70–1.63 (m, 4H), 1.63–1.56 (m, 8H). ^{13}C NMR (DMSO-d_6, 126 MHz) δ 166.5, 145.8, 137.5, 128.0, 125.4, 69.8, 67.9, 53.9, 52.6, 48.5, 46.9, 27.6, 27.3, 25.3, 22.6, 20.8, 19.5. MS (ESI positive) *m/z*: $[C_{24}H_{44}N_4O_2]^{2+}$ calcd: 210.17; found: 210.16. MS (ESI negative) *m/z*: $[C_{14}H_{14}O_6S_2]^{2-}$ calcd: 171.01; found: 171.01.

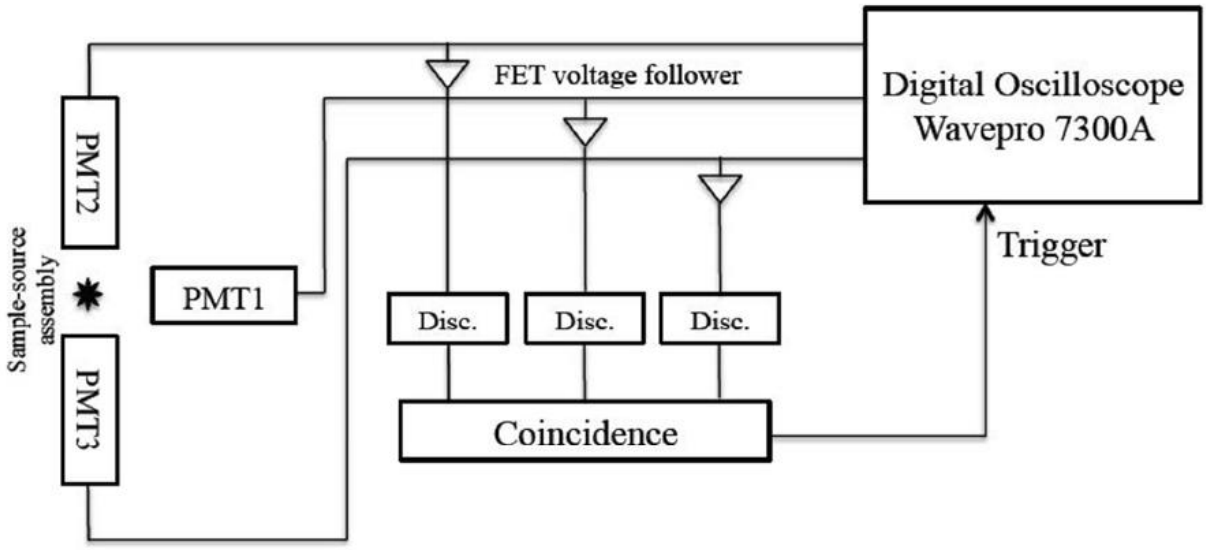

Figure 4-10. Schematic diagram of the positron annihilation lifetime spectroscopy (PALS) system

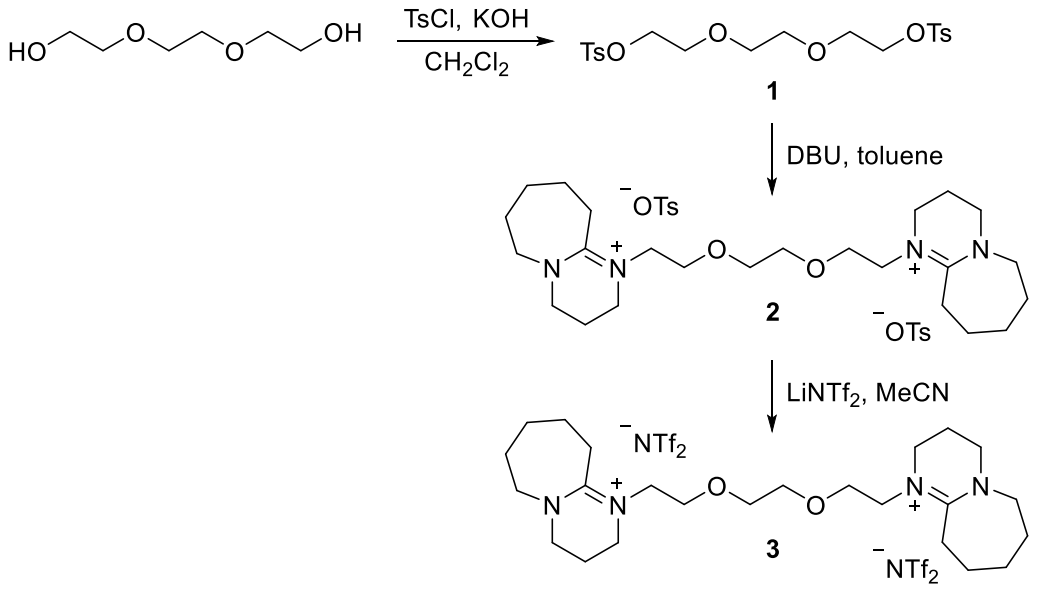

Figure 4-11. General synthetic scheme for synthesis of [DBU–PEG][Tf_2N]$_2$ ionic liquid

8,8′-(3,6-dioxaoctane-1,8-diyl)bis(1,8-Diazabicyclo[5.4.0]undec-7-en-8-ium) bis(trifluoromethanesulfonyl)imide (Tf_2NDBUPEG150DBUNTf_2) (3) Ditosylate **2** (3.31 g, 4.34 mmol) was dissolved in acetonitrile (30 mL), and lithium bis(trifluoromethanesulfonyl)imide ($LiNTf_2$) (2.74 g, 9.56 mmol) was added. The mixture was stirred at room temperature overnight and then diluted with dichloromethane (30 mL), washed with deionized water (3 × 40 mL), dried over magnesium sulfate, filtered, concentrated, and dried under vacuum to yield **3** as a yellow oil (2.29 g, 54%).

^{1}H NMR (DMSO-d_6, 500 MHz) δ 3.72 (t, J = 5.2 Hz, 4H), 3.66–3.61 (m, 4H), 3.60–3.53 (m, 8H), 3.50–3.44 (m, 8H), 2.89–2.83 (m, 4H), 1.96 (t, J = 5.2 Hz, 4H), 1.72–1.65 (m, 4H), 1.65–1.58 (m, 8H). ^{13}C NMR (DMSO-d_6, 126 MHz) δ 166.6, 119.5 (q, $J_{C–F}$ = 322.0 Hz, NTf_2), 69.8, 67.8, 53.9, 52.6, 48.5, 46.9, 27.6, 27.3, 25.3, 22.6, 19.5. MS (ESI positive) *m/z*: $[C_{24}H_{44}N_4O_2]^{2+}$ calcd: 210.17; found: 210.16. MS (ESI negative) *m/z*: $[C_4F_{12}N_2O_8S_4]^{2-}$ calcd: 279.92; found: 279.91.

Synthesis of ZIF-8 nanoparticles[37-38] In 50 mL centrifuge vial, a solution of 2.0 g 2-methylimidazole in 20 mL methanol was added into a 20 mL methanol solution of ZnO nanoparticles (2.0 g) ethanol dispersion solution with the concentration being 40%). After the mixture was stirred for 48 hours at room temperature, white product was separated by centrifugation and washed with ethanol for three times. The product was further dried under vacuum at 60 ^{o}C overnight before further use.

Synthesis of ZSM-5 nanoparticles[39-40] The chemical composition is: 9TPAOH:0.25Al2O3:25SiO2:599H2O. The initial solutions were prepared by mixing tetraethyl orthosilicate (TEOS, 98%, Aldrich), aluminum isopropoxide (99.99%, Aldrich), and tetrapropylammonium hydroxide (TPAOH, 1 M aqueous solution, Aldrich). The silica and alumina alkoxydes were hydrolyzed under slow stirring (50 rpm) for 24 h at room temperature. The alcohols issued from the silica and alumina sources were evaporated for 5 h at 40 °C under stirring. The water weight loss due to the evaporation process was compensated by adding distilled water in the initial solution. The obtained clear solutions

were transferred in polypropylene (PP) bottles and subjected to hydrothermal (HT) treatment in a conventional oven. The syntheses were performed at 90 °C for 18 h. After the treatment, the zeolite suspensions were purified in a series of four steps consisting of high-speed centrifugation (10000 rpm, 20 min), removal of the mother liquor, and washed by water for several times.

Synthesis of Silicalite-1 nanoparticles[41] The chemical composition is: 9TPAOH:25SiO2:480H2O. The initial solutions were prepared by mixing tetraethyl orthosilicate (TEOS, 98%, Aldrich) and tetrapropylammonium hydroxide (TPAOH, 1 M aqueous solution, Aldrich). The silica alkoxydes was hydrolyzed under slow stirring (50 rpm) for 24 h at room temperature. The obtained clear solutions were transferred in polypropylene (PP) bottles and subjected to hydrothermal (HT) treatment in a conventional oven. The syntheses were performed at 90 °C for 96 h. After the treatment, the zeolite suspensions were purified in a series of steps consisting of high-speed centrifugation (10000 rpm, 20min), removal of the mother liquor, and washed by water for several times.

Synthesis route of porous liquids The fabrication of porous liquids in this work was conducted by a solution blending method. In a typical synthesis of ZIF-8 porous liquid (3.2 wt%), as-synthesized ZIF-8 nanocrystals (0.05 g) were first dispersed in 10 ml fresh methanol, after which it was vigorously stirred for 2 h and sonicated for another 2 h to disperse the ZIF-8 nanoparticles. The [DBU-PEG][Tf_2N]$_2$ ionic liquid (1.0 g) was first diluted with methanol (9.0 g) and sonicated for 20 min. The as-prepared [DBU-PEG][Tf_2N]$_2$ dilute solution was then added into collected ZIF-8 suspension solution (1 mL), and then sonicated for 2h to obtain a homogeneous suspension of ZIF-8 nanoparticles in the liquid. After thorough mixing, the resultant solution was air-dried at 80 ℃ overnight. The obtained colloidal ZIF-8 porous liquids was then kept at 40 ℃ under vacuum for further use. The other porous liquids used in this work were synthesized by a similar simple procedure by varying the type of porous solids (ZIF-8, ZSM-5 and Silicalite-1) and ILs, as well as the rough mass ratio of porous solids to ILs. To obtain a precise mass ratio of porous

solid to ionic liquid, thermo-gravimetric analysis (TGA) was adopted to determine the final content of porous framework solids in the porous liquids.

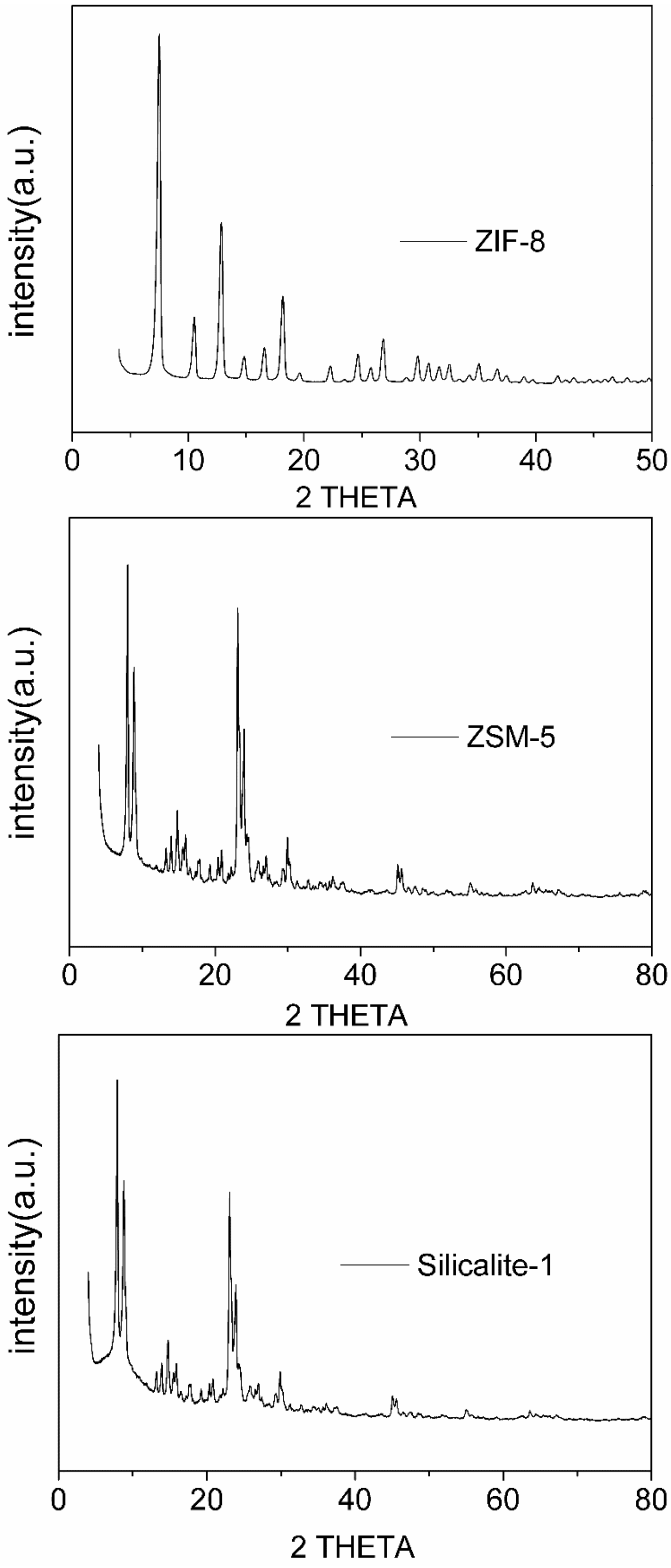

Figure 4-12. XRD of synthesized ZIF-8, ZSM-5, and Silicalite-1 nanoparticles

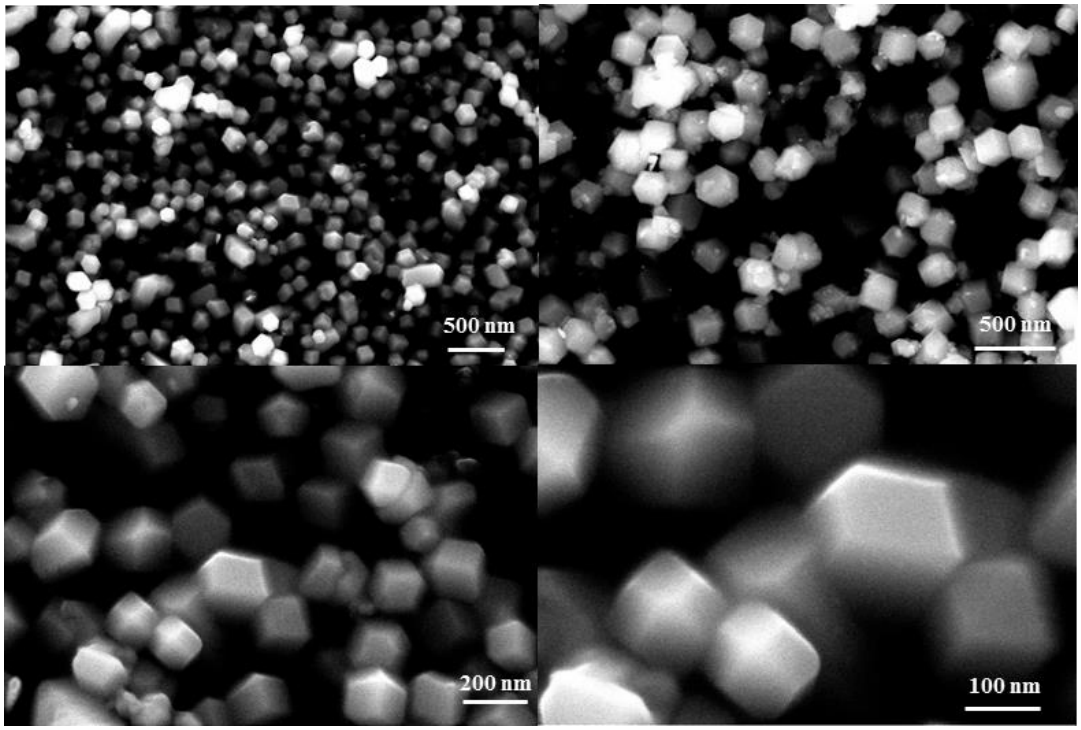

Figure 4-13. SEM images of as-synthesized ZIF-8 nanoparticles

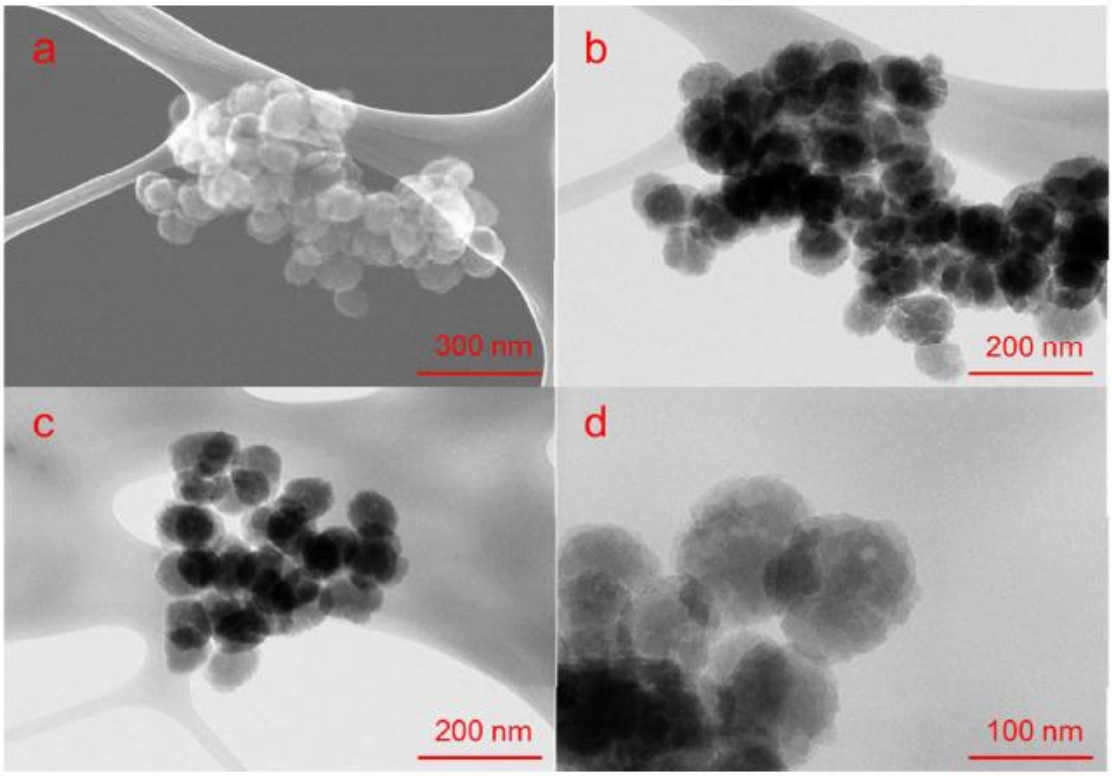

Figure 4-14. a) SEM and b-d) TEM images of as-synthesized ZSM-5 nanoparticles

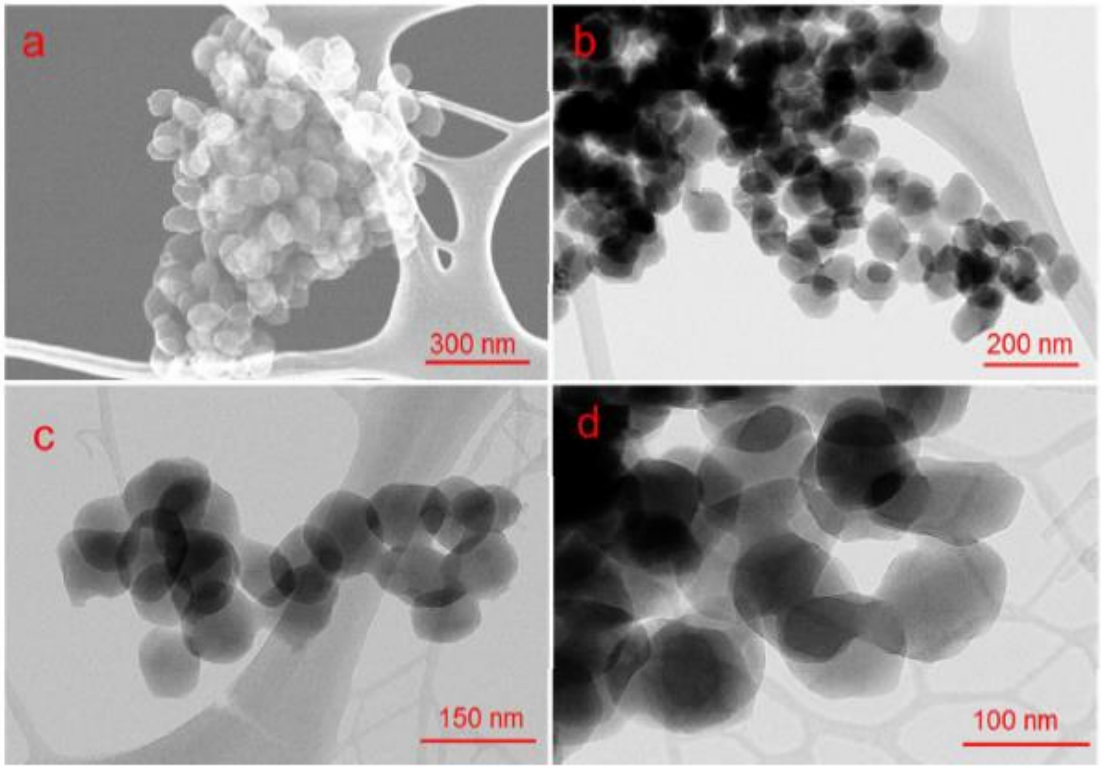

Figure 4-15. a) SEM and b-d) TEM images of as-synthesized Silicalite-1 nanoparticles

4.8 References

1. O'Reilly, N.; Giri, N.; James, S. L., Porous liquids. *Chem. - Eur. J.* **2007,** *13*, 3020.

2. Giri, N.; Del Popolo, M. G.; Melaugh, G.; Greenaway, R. L.; Ratzke, K.; Koschine, T.; Pison, L.; Gomes, M. F.; Cooper, A. I.; James, S. L., Liquids with permanent porosity. *Nature* **2015,** *527*, 216.

3. Li, J. R.; Kuppler, R. J.; Zhou, H. C., Selective gas adsorption and separation in metal-organic frameworks. *Chem. Soc. Rev.* **2009,** *38*, 1477.

4. Banerjee, R.; Phan, A.; Wang, B.; Knobler, C.; Furukawa, H.; O'keeffe, M.; Yaghi, O. M., High-throughput synthesis of zeolitic imidazolate frameworks and application to CO2 capture. *Science* **2008,** *319*, 939.

5. Cundy, C. S.; Cox, P. A., The hydrothermal synthesis of zeolites: history and development from the earliest days to the present time. *Chem. Rev.* **2003,** *103*, 663.

6. Chen, B.; Wang, L.; Zapata, F.; Qian, G.; Lobkovsky, E. B., A luminescent microporous metal– organic framework for the recognition and sensing of anions. *J. Am. Chem. Soc.* **2008,** *130*, 6718.

7. Wang, L.; Han, Y.; Feng, X.; Zhou, J.; Qi, P.; Wang, B., Metal–organic frameworks for energy storage: Batteries and supercapacitors. *Coord. Chem. Rev.* **2016,** *307*, 361.

8. Zhang, F.; Yang, F.; Huang, J.; Sumpter, B. G.; Qiao, R., Thermodynamics and Kinetics of Gas Storage in Porous Liquids. *J. Phys. Chem. B* **2016,** *120*, 7195.

9. James, S. L., The Dam Bursts for Porous Liquids. *Adv. Mater.* **2016,** *28*, 5712.

10. Greenaway, R. L.; Holden, D.; Eden, E. G. B.; Stephenson, A.; Yong, C. W.; Bennison, M. J.; Hasell, T.; Briggs, M. E.; James, S. L.; Cooper, A. I., Understanding gas capacity, guest selectivity, and diffusion in porous liquids. *Chem. Sci.* **2017,** *8*, 2640.

11. Zhang, J.; Chai, S. H.; Qiao, Z. A.; Mahurin, S. M.; Chen, J.; Fang, Y.; Wan, S.; Nelson, K.; Zhang, P.; Dai, S., Porous liquids: a promising class of media for gas separation. *Angew. Chem., Int. Ed.* **2015,** *54*, 932.

12. Giri, N.; Davidson, C. E.; Melaugh, G.; Del Pópolo, M. G.; Jones, J. T. A.; Hasell, T.; Cooper, A. I.; Horton, P. N.; Hursthouse, M. B.; James, S. L., Alkylated organic cages: from porous crystals to neat liquids. *Chem. Sci.* **2012,** *3*, 2153.

13. Liu, H.; Liu, B.; Lin, L. C.; Chen, G.; Wu, Y.; Wang, J.; Gao, X.; Lv, Y.; Pan, Y.; Zhang, X.; Zhang, X.; Yang, L.; Sun, C.; Smit, B.; Wang, W., A hybrid absorption–adsorption method to efficiently capture carbon. *Nat. Commun.* **2014,** *5*, 5147.

14. Huang, X. C.; Lin, Y. Y.; Zhang, J. P.; Chen, X. M., Ligand-Directed Strategy for Zeolite-Type Metal–Organic Frameworks: Zinc(II) Imidazolates with Unusual Zeolitic Topologies. *Angew. Chem.* **2006,** *118*, 1587.

15. Shen, K.; Qian, W.; Wang, N.; Su, C.; Wei, F., Centrifugation-free and high yield synthesis of nanosized H-ZSM-5 and its structure-guided aromatization of methanol to 1,2,4-trimethylbenzene. *J. Mater. Chem. A* **2014,** *2*, 19797.

16. Yang, J.; Li, J.; Wang, W.; Li, L.; Li, J., Adsorption of CO2, CH4, and N2 on 8-, 10-, and 12-Membered Ring Hydrophobic Microporous High-Silica Zeolites: DDR, Silicalite-1, and Beta. *Ind. Eng. Chem. Res.* **2013,** *52*, 17856.

17. Armand, M.; Endres, F.; MacFarlane, D. R.; Ohno, H.; Scrosati, B., Ionic-liquid materials for the electrochemical challenges of the future. *Nat. Mater.* **2009,** *8*, 621.

18. Wang, C.; Luo, X.; Luo, H.; Jiang, D. E.; Li, H.; Dai, S., Tuning the basicity of ionic liquids for equimolar CO2 capture. *Angew. Chem., Int. Ed.* **2011,** *50*, 4918.

19. Zhang, H.; Dasbiswas, K.; Ludwig, N. B.; Han, G.; Lee, B.; Vaikuntanathan, S.; Talapin, D. V., Stable colloids in molten inorganic salts. *Nature* **2017,** *542*, 328.

20. Geise, G. M.; Doherty, C. M.; Hill, A. J.; Freeman, B. D.; Paul, D. R., Free volume characterization of sulfonated styrenic pentablock copolymers using positron annihilation lifetime spectroscopy. *J. Membr. Sci.* **2014,** *453*, 425.

21. Liu, M.; Wong-Foy, A. G.; Vallery, R. S.; Frieze, W. E.; Schnobrich, J. K.; Gidley, D. W.; Matzger, A. J., Evolution of nanoscale pore structure in coordination polymers during thermal and chemical exposure revealed by positron annihilation. *Adv. Mater.* **2010,** *22*, 1598.

22. Costa Gomes, M.; Pison, L.; Červinka, C.; Padua, A., Porous Ionic Liquids or Liquid Metal–Organic Frameworks? *Angew. Chem.* **2018,** *130* (37), 12085-12088.

23. Tokuda, H.; Hayamizu, K.; Ishii, K.; Susan, M. A. B. H.; Watanabe, M., Physicochemical properties and structures of room temperature ionic liquids. 1. Variation of anionic species. *J. Phys. Chem. B* **2004,** *108*, 16593.

24. Bester-Rogac, M.; Stoppa, A.; Hunger, J.; Hefter, G.; Buchner, R., Association of ionic liquids in solution: a combined dielectric and conductivity study of [bmim][Cl] in water and in acetonitrile. *Phys. Chem. Chem. Phys.* **2011,** *13*, 17588.

25. Kinik, F. P.; Altintas, C.; Balci, V.; Koyuturk, B.; Uzun, A.; Keskin, S., [BMIM][PF6] Incorporation Doubles CO2 Selectivity of ZIF-8: Elucidation of Interactions and Their Consequences on Performance. *ACS Appl. Mater. Interfaces* **2016,** *8*, 30992.

26. Koyuturk, B.; Altintas, C.; Kinik, F. P.; Keskin, S.; Uzun, A., Improving Gas Separation Performance of ZIF-8 by [BMIM][BF4] Incorporation: Interactions and Their Consequences on Performance. *J. Phys. Chem. C* **2017,** *121*, 10370.

27. Li, H.; Tuo, L.; Yang, K.; Jeong, H. K.; Dai, Y.; He, G.; Zhao, W., Simultaneous enhancement of mechanical properties and CO2 selectivity of ZIF-8 mixed matrix membranes: Interfacial toughening effect of ionic liquid. *J. Membr. Sci.* **2016,** *511*, 130.

28. Anthony, J. L.; Maginn, E. J.; Brennecke, J. F., Solubilities and thermodynamic properties of gases in the ionic liquid 1-n-butyl-3-methylimidazolium hexafluorophosphate. *J. Phys. Chem. B* **2002,** *106*, 7315.

29. Andreu, J. S.; Vega, L. F., Modeling the solubility behavior of CO2, H2, and Xe in [Cn-mim][Tf2N] ionic liquids. *J. Phys. Chem. B* **2008,** *112*, 15398.

30. Culp, J. T.; Smith, M. R.; Bittner, E.; Bockrath, B., Hysteresis in the physisorption of CO2 and N2 in a flexible pillared layer nickel cyanide. *J. Am. Chem. Soc.* **2008,** *130*, 12427.

31. Rabone, J.; Yue, Y. F.; Chong, S.; Stylianou, K.; Bacsa, J.; Bradshaw, D.; Darling, G.; Berry, N.; Khimyak, Y.; Ganin, A., An adaptable peptide-based porous material. *Science* **2010,** *329*, 1053.

32. Yang, S.; Lin, X.; Lewis, W.; Suyetin, M.; Bichoutskaia, E.; Parker, J. E.; Tang, C. C.; Allan, D. R.; Rizkallah, P. J.; Hubberstey, P., A partially interpenetrated metal-organic framework for selective hysteretic sorption of carbon dioxide. *Nat. Mater.* **2012,** *11*, 710.

33. Hu, X.; Xu, D.; Wirth, B. D., Quantifying He-point defect interactions in Fe through coordinated experimental and modeling studies of He-ion implanted single-crystal Fe. *J. Nucl. Mater.* **2013,** *442* (1, Supplement 1), S649-S654.

34. Zhao, Y. N.; Yang, Z. Z.; Luo, S. H.; He, L. N., Design of task-specific ionic liquids for catalytic conversion of CO2 with aziridines under mild conditions. *Catal. Today* **2013,** *200*, 2-8.

35. Bednarova, E.; Hybelbauerova, S.; Jindrich, J., Optimized methods for preparation of 6(I)-(omega-sulfanyl-alkylene-sulfanyl)-beta-cyclodextrin derivatives. *Beilstein J Org Chem* **2016,** *12*, 349-52.

36. Yang, Z.-Z.; Zhao, Y.-N.; He, L.-N.; Gao, J.; Yin, Z.-S., Highly efficient conversion of carbon dioxide catalyzed by polyethylene glycol-functionalized basic ionic liquids. *Green Chemistry* **2012,** *14* (2), 519.

37. Song, Q.; Nataraj, S. K.; Roussenova, M. V.; Tan, J. C.; Hughes, D. J.; Li, W.; Bourgoin, P.; Alam, M. A.; Cheetham, A. K.; Al-Muhtaseb, S. A.; Sivaniah, E., Zeolitic imidazolate framework (ZIF-8) based polymer nanocomposite membranes for gas separation. *Energy Environ. Sci.* **2012,** *5* (8), 8359.

38. Fujie, K.; Yamada, T.; Ikeda, R.; Kitagawa, H., Introduction of an ionic liquid into the micropores of a metal-organic framework and its anomalous phase behavior. *Angew Chem Int Ed Engl* **2014,** *53* (42), 11302-5.

39. Wirawan, S. K.; Creaser, D., CO2 adsorption on silicalite-1 and cation exchanged ZSM-5 zeolites using a step change response method. *Microporous and Mesoporous Materials* **2006,** *91* (1-3), 196-205.

40. Ghezini, R.; Sassi, M.; Bengueddach, A., Adsorption of carbon dioxide at high pressure over H-ZSM-5 type zeolite. Micropore volume determinations by using the Dubinin–Raduskevich equation and the “t-plot” method. *Microporous and Mesoporous Materials* **2008,** *113* (1-3), 370-377.

41. Yang, J.; Li, J.; Wang, W.; Li, L.; Li, J., Adsorption of CO2, CH4, and N2on 8-, 10-, and 12-Membered Ring Hydrophobic Microporous High-Silica Zeolites: DDR, Silicalite-1, and Beta. *Ind. Eng. Chem. Res.* **2013,** *52* (50), 17856-17864.

CHAPTER 5. INVESTIGATING THE MODE OF GAS SORPTION IN POROUS LIQUIDS VIA IN-SITU FTIR STUDY OF CARBON DIOXIDE ISOTHERMS

5.1 Abstract

Porous liquids are a new class of fluid sorbents that combine the attributes of porous materials into a nonvolatile liquid matrix, creating permanent cavities in the liquid phase. The addition of free spaces into the liquid can promote gas sorption and transport through the medium. Attenuated total reflectance Fourier transform infrared spectroscopy (ATR-FTIR) was used to analyze a type III porous liquid created from a bulky ionic liquid and zeolitic imidazolate framework-8 (ZIF-8). A high-pressure ATR cell was used to record in situ measurements of carbon dioxide sorption. The ionic liquid phase shows no significant differences, while the ZIF-8 displays peak shifts upon incorporation of CO_2. At pressures below 1 bar, CO_2 uptake proceeds via physisorption as seen by the antisymmetric stretching mode of dissolved carbon dioxide. Upon increasing pressures from 2 to 7 bar, free gaseous CO_2 modes become apparent. Relative quantitation and preliminary concentration calculations were also completed.

5.2 Introduction

Many materials have been proposed for use in carbon capture and storage. Traditional porous absorbents such as activated carbons, zeolites, and framework materials have a high surface area and high capacity but are limited by low selectivity. Ionic liquids (ILs) with negligible vapor pressure and tunable solubility are also capable of physisorption. ILs have a more limited capacity but are highly selective and easily regenerated via pressure swing or nominal heating. This tradeoff between a highly selective or highly efficient separation is one of the primary limitations of gas separation and storage. With the development of advanced materials, perhaps a synergistic relationship between these two features could be achieved through the proper combination.

Free volume has long been a point of interest in the field of polymer membrane materials. Mass transport is enhanced in the void spaces comparted to the dense bulk phase. However, even in the solid phase of rigid glassy polymers, the long-term stability of these voids is a challenge still being investigated. In traditional liquids, free volume is

predominately extrinsic porosity which occurs due to the intermolecular spacing between molecules. In contrast, traditional porous materials have high free volumes and varying stability based on their composition. These range from rigid matrices like zeolites and carbons, to flexible but relatively resilient frameworks like MOFs and COFs.

In 2007 O'Reilly et al proposed porous liquids as a new class of fluid adsorbents that combine the attributes of porous materials with a nonvolatile liquid matrix.[1] Incorporation of intrinsic porosity into the liquid phase has been suggested via three different strategies: type I as a neat liquid and type II/III as a host or framework material respectively in a bulky solvent. With the proper selection of components, permanent cavities can be achieved in the liquid phase. In 2015, Zhang created the first type I porous liquid with permanent cavities in a neat liquid by functionalizing hollow silica spheres through grafting long chains.[2] The addition of free spaces into the liquid have been theorized to promote gas transport through the medium. Indeed, the incorporation of the hollow moiety was found to enhance the gas permeability through membranes created using the HS-liquids.[2] While more synthetically demanding, these neat liquids lend themselves to inherent stability.

In contrast, proper design of type II or III liquids generally rely on size and weaker noncovalent interactions. The primary concern is the chemical structure of the solvent, finding a composition which is capable of creating a homogeneous solution that is solvating but non-saturating. In other words, the goal is to create a solvation shell around the porous material, without intrusion of the liquid into pores. A straightforward answer to this problem is the use of size exclusion, where every dimension of the solvent is larger than the smallest dimension of the solute. Therefore, the solvent ILs must be carefully designed with bulky ions larger than the apertures in the porous material to retain the intrinsic porosity. Additionally, the porous particle size must remain small to avoid phase separation where the solids could precipitate out of solution. Nanoscale materials can be used to generate a more stable colloidal suspension with better longevity.

Recently, our group reported on a type III porous liquid[3] using a new dicationic liquid from glycol-linked DBU heterocycles, with $[DBU\text{-}PEG]^{2+}$ dimensions large enough

to be excluded from 3.4 Å apertures[4] of zeolitic imidazolate framework-8 (ZIF-8). The resulting mixture yielded stable type III porous liquids at various concentrations from 3 to 30 wt%. Investigation of the gravimetric adsorption properties of the [DBU-PEG][Tf_2N]$_2$ ZIF-8 porous liquids (PL) showed they have 77-96% of theoretical capacity based on their composition and approximately 5 times greater CO_2/N_2 selectivity compared to ZIF-8. The presence of unique hysteresis seen in PL and pure IL was an interesting observation which prompted further investigation.

In situ attenuated total reflectance Fourier transform infrared spectroscopy (ATR-FTIR) was chosen to better understand the structure, interfacial properties, and gas adsorption mechanism of these new materials. Both ionic liquids and polymers have been the subject of in situ supercritical fluid spectroscopy in the past.[5-6] In addition, some composite materials have been previously examined by IR to probe the interfacial interactions.[7] Thus far, porous liquids in the literature have been primarily examined for their synthesis and stability, with some limited applications. Herein, we intend to explore both the interfacial chemical properties and gas adsorption mechanism through FTIR. The resulting datasets were used to quantify the amount of CO_2 sorption using integrated peak areas. The concentration calculations from IR will be compared to gravimetric analysis of gas sorption. Additional analysis of the structure will be examined through x-ray scattering.

5.3 Experimental

Carbon dioxide (99.999 %) and nitrogen (UHP) were purchased from Airgas. Additionally, an in-line Agilent moisture trap was added to remove any residual moisture from the incoming gases. Ionic liquids and porous liquids were synthesized based on previously reported procedures.[3] **Figure 5-1** depicts structures of [DBU-PEG][Tf_2N]$_2$ and zeolitic imidazolate framework-8 (ZIF-8) and a graphical representation of the combination resulting in a porous liquid.

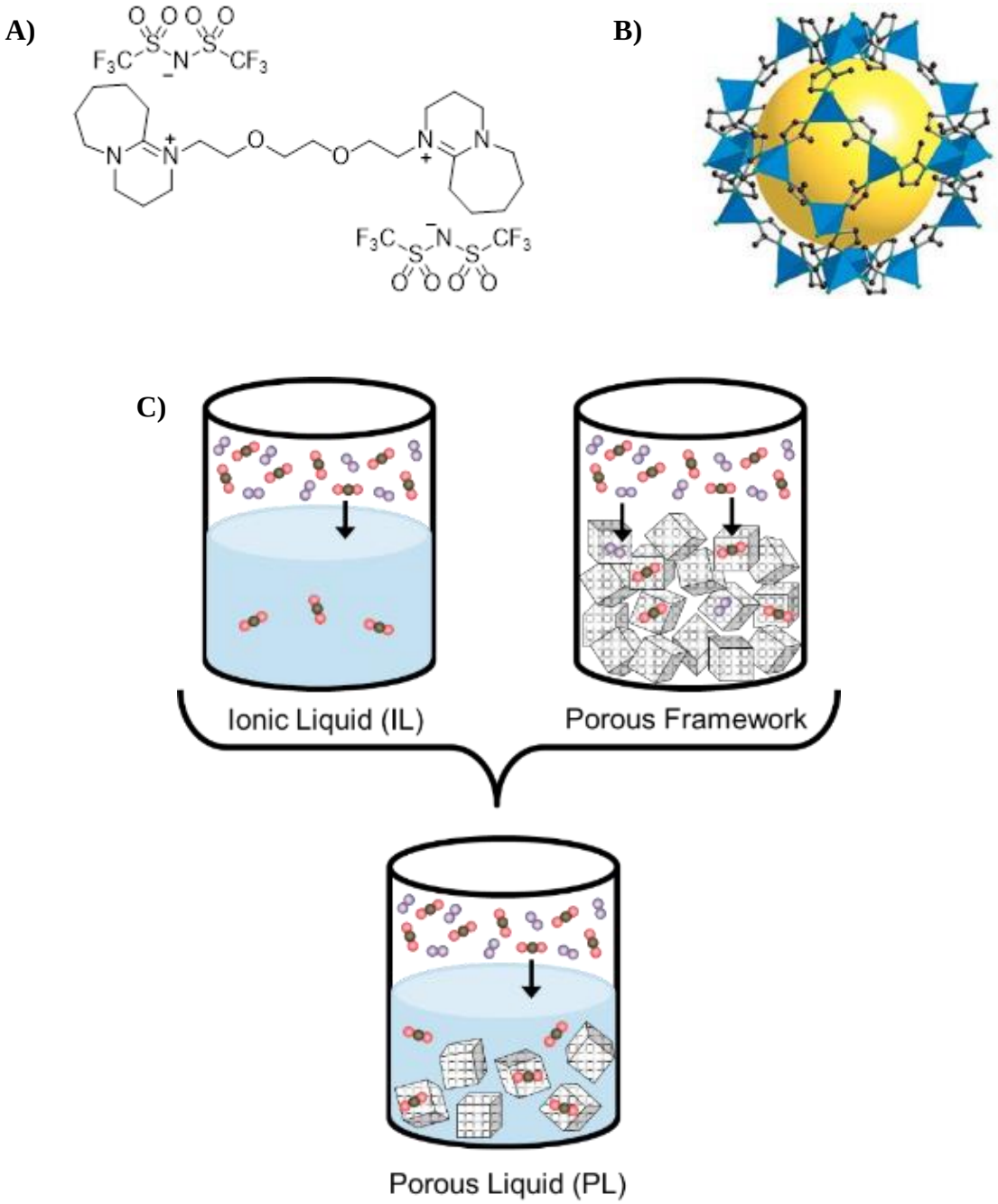

Figure 5-1. The chemical structures of a) [DBU-PEG][Tf_2N]$_2$ IL; b) ZIF-8 porous framework with tetrahedrons showing the coordination of zinc to 2-methylimidazolate;[4] and c) a graphical schematic depicting the porous liquid.

Fourier transform infrared spectroscopy was completed using a Perkin Elmer Frontier FTIR with LiTaO3 detector. In order to achieve a consistent background throughout the entire series of measurements, both the detector and sample compartments were constantly purged using a Parker Balston generator which provided dry air flow with less than 1 ppm CO_2. A Golden Gate Attenuated Total Reflectance (ATR) accessory was purchased from Specac with a diamond crystal and custom high-pressure sample cell. This supercritical fluid cell ATR top plate was modified from the original 1/16" to 1/8" stainless steel tubing. A 4000 series temperature controller for the ATR top plate was also obtained from Specac.

Following the addition of each new sample, the pressure cell was sealed with a new graphite gasket. The temperature-controlled ATR stage allowed for in-situ preparation of the liquid samples. Each sample was heated under vacuum at 60 °C overnight to outgas prior to measurement. An inline pressure gauge and needle valve allowed for precise dosing of pressures. A schematic of the cell and instrument setup is provided in **Figure 5-2**. Scans were taken with 2 cm^{-1} resolution. Sample equilibration at each pressure was checked at 5-minute intervals until the peak intensity remained constant. The total equilibration time was sample dependent and varied from 10 to 40 minutes.

5.4 Results

5.4.1 Preliminary Spectroscopic Investigation – Precursors vs. Composite

Pure IL. To begin, the pure ionic liquid was characterized since the cation, to the best of our knowledge, has not previously been reported in the literature except in our former work. The common [Tf_2N] anion used here has been previously studied by other groups, and numerous predominant peaks in the fingerprint region correspond well to its known vibrations.[8-9] The peaks at 1618, 1528 cm^{-1} are most likely contributions from the substituted amidine from DBU. Some vibrational frequencies of interest are reported in **Table 5-1**.

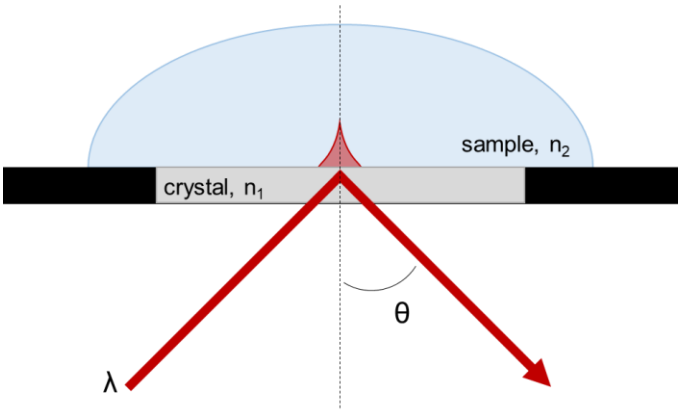

Figure 5-2. a) Image of the setup for in-situ measurements, and b) a graphical representation of the evanescent wave

Table 5-1. IR peaks of interest for pure CO_2, IL, and ZIF-8

	Vibrational Frequencies (cm^{-1})	
	Literature	**Experimental**
CO_2		
bending ν_2	667	
antisymmetric ν_3	2349	2385-2300
IL $[Tf_2N]^-$		
CF_3 antisymmetric bending	571	568
SO_2 antisymmetric bending(in-, out-of-plane)	602, 619	599, 613
S-N-S bending	651	653
S-N-S symmetric stretching	741, 762	740, 762
C-S stretching	790, 1058	788, 1051
SO_2 symmetric stretching (in-plane)	1139, 1195, 1231	1132, 1174, 1226
SO_2 antisymmetric stretching (out-of-plane)	1333, 1352	1328, 1348
ZIF-8		
imidazole aromatic C-H stretch[10]	3136	
Ring out-of-plane bending[10]	759	
C=N stretch[11]	1580	
Zn-N bond[12]	421	
transmission[4]		

Pure ZIF-8. To ensure a conformal coating of the diamond ATR crystal was maintained for the duration of the preparation and analysis, the ZIF-8 powder was dispersed in ethanol in an ultrasonic bath and the resulting suspension was used to coat the crystal via a drop-casting method. Small quantities of the solution were subsequently added and dried to form an opaque layer that covered and surrounded the entire crystal. As additional verification that the drop-cast method provided sufficient coating of material, the Universal ATR accessory from Perkin Elmer was used with pressure anvil and yielded similar results. Specific peaks that have previously been reported in the literature are listed in **Table 5-1**.

Porous Liquid. When comparing the two fluids, the porous liquid reveals similar features to the individual components, as seen in **Figure 5-3**. As expected, the porous liquid shows incorporation of ZIF-8 yields peaks from the framework material[10, 13] (denoted by asterisks) while maintaining very similar features to the pure IL. In general, the absorbance of the porous liquid is less than that of the ionic liquid, this could be due to reduced intermolecular interactions in the ionic liquid phase due to the incorporation of the porous material. Reduced intensity of the liquid peaks can be attributed to the IL lower concentration of the IL as fewer ions persist in the path of the IR beam. Interestingly, there are a few peaks that show higher relative absorbance in the PL, 1651, 1450, and 759 cm^{-1}; yet two other PL peaks that have lower relative absorbance than their respective IL peaks, 1329 and 599 cm^{-1}.

5.4.2 In-situ CO_2 Adsorption Monitored via FTIR

It is well known that carbon dioxide is considered a greenhouse gas since it is a strong infrared absorber. CO_2 is a linear molecule with $D_{\infty h}$ symmetry which has four vibrational modes: symmetric stretching, asymmetric stretching, and two degenerate bending modes. Of these modes, all but one result in a change of dipole moment and are therefore IR active. Carbon dioxide is ubiquitous and can be a common "contaminant" seen

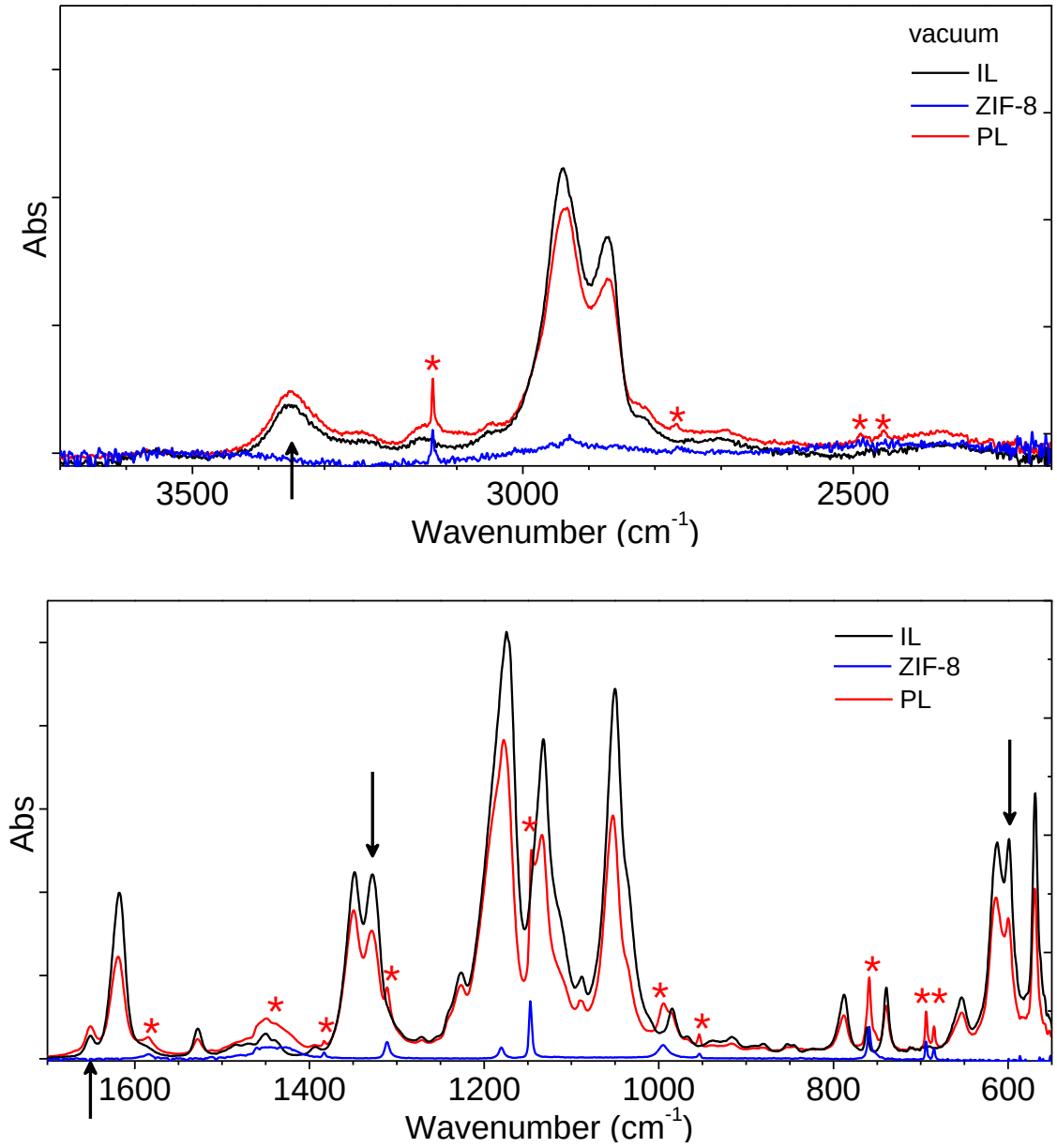

Figure 5-3. Spectra of the two precursors, [DBU-PEG][Tf_2N]$_2$ and ZIF-8, and resultant 20 wt% ZIF-8-PL in the evacuated sample chamber. Points of interest included increased resolution of ZIF-8 features in the PL (marked by *) and changes in relative intensity of IL (marked by arrows).

in routine infrared analysis, along with atmospheric water. This problem is so common, in fact, that most instrument manufacturers have devised an algorithm to minimize and suppress these spectral features.

Atmospheric CO_2 yields a significant signal and is prone to fluctuations due to differences in air flow in the laboratory, which can lead to variability between background and sample measurements. For these experiments, all CO_2 and H_2O suppression features have been deactivated, and scrupulous attention was given to adequately purging the sample environment. To ensure a consistent background throughout the duration of the measurement, a constant purge of the optical and sample compartments was maintained. As a frame of reference, the prominent features in the spectra of CO_2 gas are shown in **Figure 5-4**. The antisymmetric stretching mode ν_3 (2285-2385) seen as two primary branches due to the rotational-vibrational coupling yielding the P and R branches at 2337 and 2362. The other distinctive feature is the bending mode ν_2 at 668.

5.4.3 CO_2 and Ionic Liquid, [DBU-PEG][Tf_2N]$_2$.

Real time in-situ measurements with FTIR allow for insight into the adsorption process. Initially, the pure IL was examined independently to determine method of CO_2 sorption. At pressures up to 5 bar, there are no major changes in IL peaks, the only signal changes come from the incorporation of the CO_2 gas, as seen in **Figure 5-5**. At low pressures a new peak emerges from the CO_2 antisymmetric stretching band at 2340.5 cm^{-1} (shoulder 2328) and the IL peak at 653.5 cm^{-1} increases in absorbance, both of these peaks increase absorbance with increasing pressure. At 1.5 bar, we begin seeing deviation from the baseline near 2361 cm^{-1} and 667.5 cm^{-1} both of which become more substantial peaks at 4 bar. These primary differences can be attributed to the dissolution of free CO_2. In comparison we also see slight decreases in the absorbance of other peaks with increasing pressure. This has previously been attributed to the swelling of the structure upon gas incorporation into the sample and has been seen in both ionic liquids and polymers.

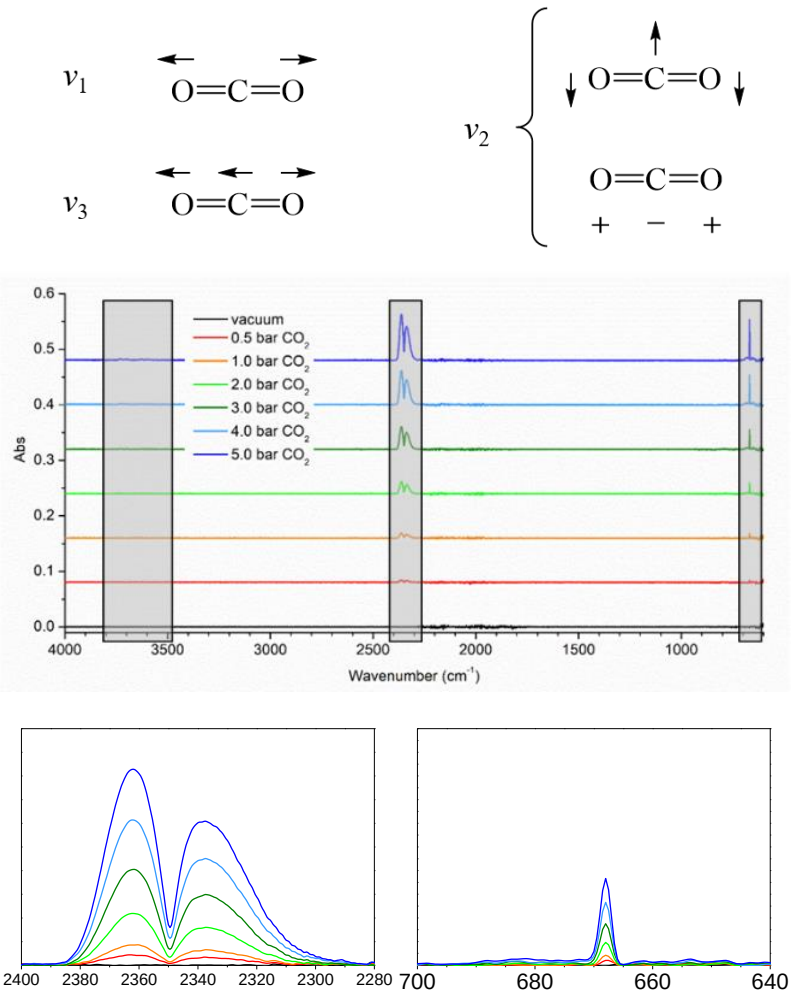

Figure 5-4. Stretching and bending modes of carbon dioxide and representative spectra from empty ATR cell with increasing pressures of CO_2 gas

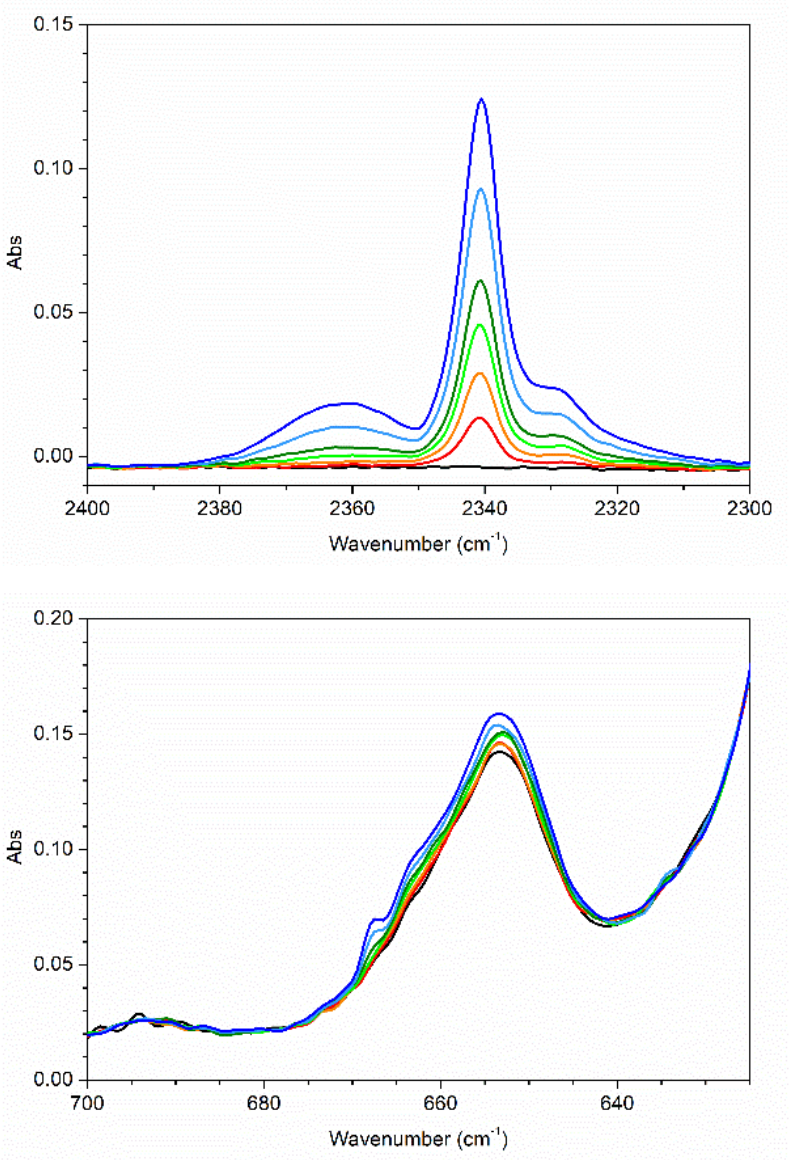

Figure 5-5. In-situ FTIR of [DBU-PEG][Tf_2N]$_2$. Changes in IR absorption with increasing pressure in pure ionic liquid, [DBU-PEG][Tf_2N]$_2$, from vacuum up to 4 bar CO_2.

Minimal interactions have been reported for other [Tf_2N]-based ILs in the past. For example, Seki found that dissolved CO_2 in [bmim][Tf_2N] retained features most similar to the two pure components compared to other imidazolium ILs with fluorinated anions, with only slight shifts in the SO_2 and CF_3 bands.[14]

Kazarian and coworkers have previously studied the bending mode of supercritical CO_2 in [bmim][PF_6] and [bmim][BF_4] and observed the broadening and different magnitudes of peak splitting in the ν_2 band due to the removal of the double degeneracy as the gas molecule interacts with the IL.[5] The increase in magnitude of the [DBU-PEG][Tf_2N]$_2$ in **Figure 5-5** is likely due to an overlapping signal from the CO_2, and the appearance of a small shoulder near 660 cm^{-1} could signify slight bending of the CO_2 as it interacts with Lewis base sites in the IL. Unfortunately, precise analysis of the bending modes in this system is complicated due to interference from an intrinsic peak of the IL.

Previously in ionic liquids and polymers the antisymmetric stretching mode of dissolved CO_2 has been identified in the same region seen here, with peak maxima occurring anywhere from 2336-2344 cm^{-1} and a shoulder on the low wavenumber side of the main band.[5-6, 15-19] Interestingly, in addition to the dissolved CO_2 peak near 2340 cm^{-1}, in the pure IL we begin to see contributions from free CO_2 at 2360 cm^{-1} at pressures above one bar. This is a unique observation compared to other published ILs which only show the dissolved CO_2 peak. In some ways, this more closely resembles spectra of dissolved gases in saline aqueous environments. For example, Schadle and coworkers observed the equilibration of both the 2360 cm^{-1} gaseous CO_2 peak and the 2340 cm^{-1} dissolved CO_2 peak as brine samples came to equilibrium.[20]

5.4.4 CO_2 and Porous Solid, ZIF-8.

While in-situ measurements of the ionic liquid only show changes from incorporation of the known CO_2 bands, the gas incorporation into pure ZIF-8 causes slight peak shifts suggesting there is some structural variation upon sorption (**Figure 5-6**). Ania

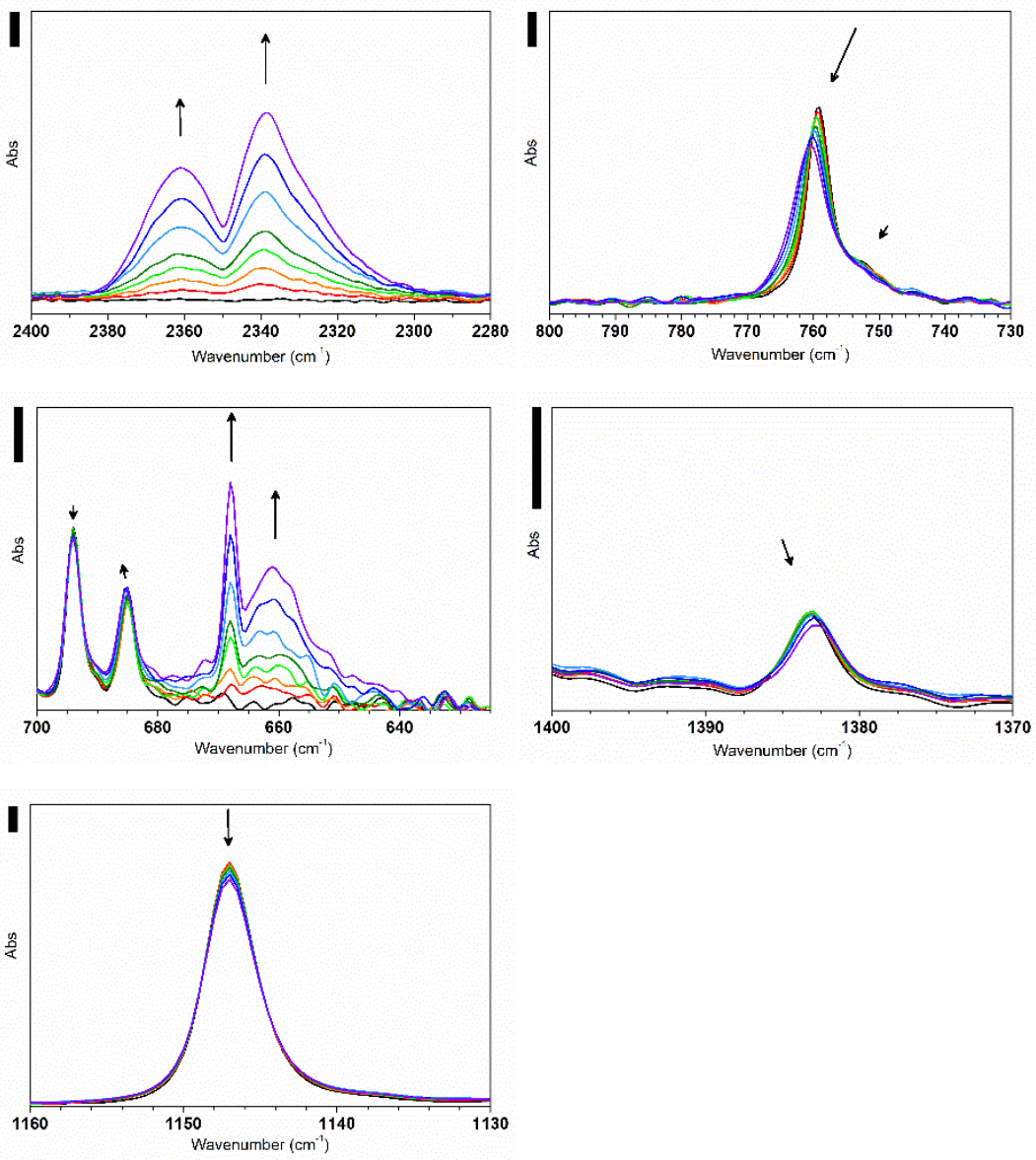

Figure 5-6. In-situ FTIR of ZIF-8. Intensity changes in IR absorption with increasing pressure in pure porous solid, ZIF-8, from vacuum up to 5 bar CO_2. Arrows indicate the direction of intensity change with increasing pressure. Scale bars represent 0.01 arbitrary units of absorbance.

et al performed a variety of simulations using different molecular probes to verify that polarizability, size, and shape all play important roles in the type/extent of structural deformation imparted in the ZIF-8 structure.[21]

5.4.5 CO_2 and 20 wt% Porous Liquid

As seen in **Figure 5-7**, in the 20 wt% porous liquid physisorbed CO_2 peaks appear and have higher absorbance values than those seen in the pure IL. This is consistent with the gravimetric analysis, where incorporation of the porous material enhances the gas sorption capability of the liquid. Even with relatively low CO_2 pressures investigated here, there are significant shifts in position and intensity of some ZIF-8 peaks (denoted by arrows) The changes in the ZIF-8 peaks are similar in some aspects to measurements at pressures up to 1.6GPa applied with a diamond anvil cell which produced red shifts in the peaks at 1584, 1145, 995, and 950 cm^{-1} attributed to weakening of the pi bonds due to ring distortion.[10] Hu and coworkers subsequently examined high pressure CO_2 loadings up to 2.6 GPa and found no pressure dependence on the C=N 1584 cm^{-1} mode at all, only the appearance of 1620 cm^{-1} band for C=C ring stretching.[22]

Upon increasing pressure from vacuum up to 7 bar, significant differences arise in the 20 wt% PL investigated in this work. For example, both the 1584 and 759 cm^{-1} peaks have a blue shift when exposed to moderate pressures of carbon dioxide and decrease in intensity. These changes in structure with respect to the C=N stretch and the ring out of plane bending, suggest perhaps a greater opening to the window apertures of the ZIF-8. Other blue shifted peaks include 995, 684, 653 cm^{-1} which decrease and increase in absorbance repectively. A variety of other bands show decreases in intensity and red shift including 1384, 1311, and 1146 cm^{-1}.

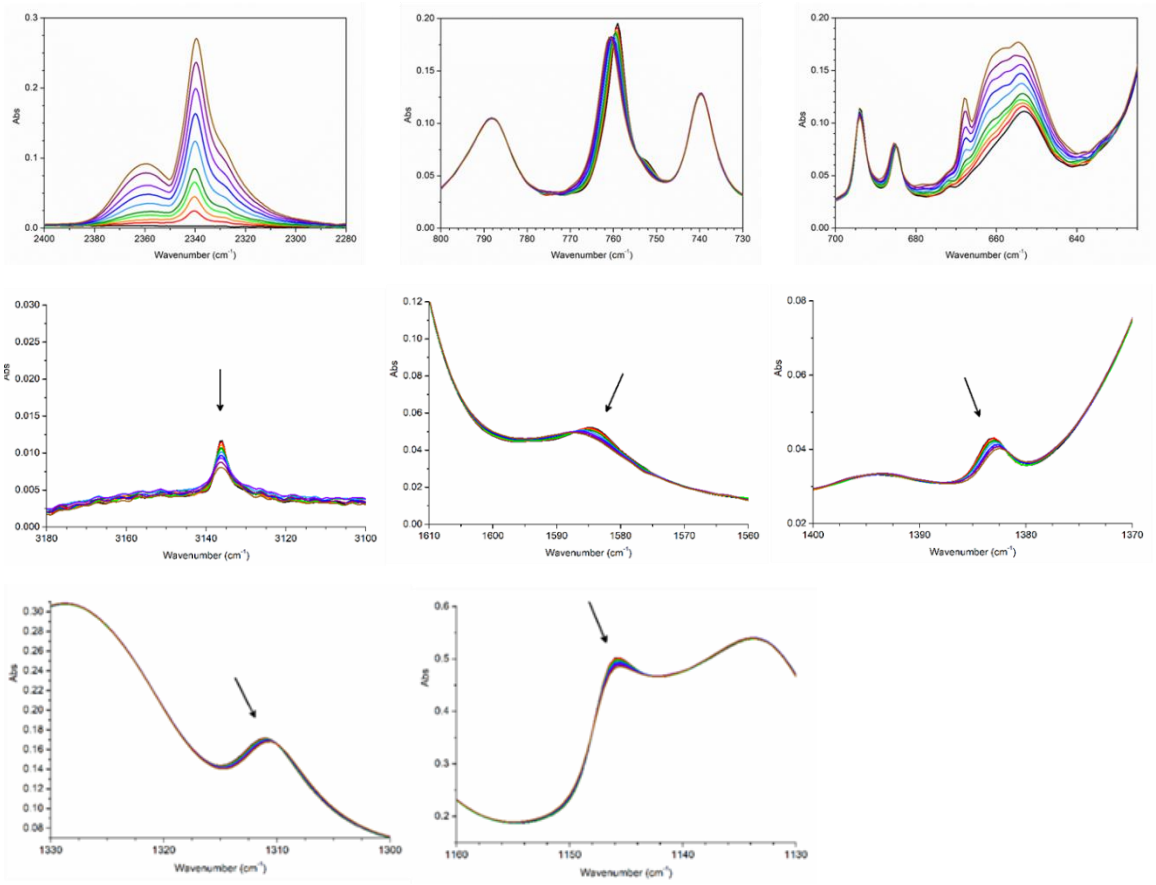

Figure 5-7. In-situ FTIR of 20 wt% PL. Changes in IR absorption with increasing pressure in 20 wt% PL, from vacuum up to 7 bar CO_2. Arrows indicate the direction of intensity change with increasing pressure

5.5 Discussion

5.5.1 Moderate Peak Shift in ZIF-8 and Porous Liquid

Similar systems to porous liquids have been previously investigated, like a ZIF-8-glycol slurry which was found to have a CO_2 capacity of 1.25 mol/L at 1 bar and authors suggest the glycol is too large to enter pores.[23] However, other research has shown that the movable imidazolate linkers add flexibility to the structure and allows the structure to fit larger molecules than would normally be expected from the aperture size.[24] It was previously reported that extremely under extremely high pressures, ZIF-8 has some structural deformation. However, based on results from Fairen-Jimenez and coauthors, even low pressure gas adsorption can have similar effects on the structure of this MOF as seen in the stepwise N_2 isotherm at 77K.[24] The extent of the structure distortion is dependent not only on pressure but also the shape, size, and polarizability of sorbent gases making for very dynamic structure properties.[21] Therefore, the chemical environment surrounding the ZIF-8, such as interactions with the ionic liquid, could have similar aperture or gate/window opening behavior due to the flexibility of the structure.

When ZIF-8 is exposed to aqueous acid gas conditions it decomposes the MOF into its 2-methylimidazole precursor along with a zinc carbonate in an irreversible reaction,[25] where bands appear at 1335 and 1596 for the zinc carbonate/hydroxides and 3200 for reformation of NH bond in the imidazole. However, in alternative solvents this reaction is not seen. The hydrophobicity of the Tf_2N IL, in comparison to hygroscopic liquids will inhibit this destabilization. Narayana used Brillouin spectroscopy to study the effects of pore occupancy on the elastic modulus of ZIF-8 and found that incorporation of gases increase the flexibility of the structure.[26] They also found significant differences at temperatures below 270 K suggesting a possible change in the structure due to deformation of the imidazolate linker similar to a gate opening effect seen at high pressures[26]

5.5.2 Free CO_2

Most FTIR studies have been done at higher pressures and temperatures, at least to some extent due to the interference of atmospheric CO_2 all begin measurements at 10 bar or higher due to baseline fluctuations. The closest spectroscopic comparisons in literature are primarily studying the effects of supercritical CO_2 on liquids and polymers. Using a constant purge gas prior to and throughout the duration of the measurement allows greater sensitivity and a lowered limit of detection. The appearance of the 2360 cm^{-1} free CO_2 peak seen here could be a result of a cleaner background baseline. By minimizing fluctuations in the peak of interest, long term measurements can be achieved. These comparatively "low pressure" measurements provide a better approximation to how the systems would be used in real world applications. In the carbon capture and sequestration process near ambient pressures and low partial pressures of CO_2 are closer to what is investigated here.

This peak is of particular interest due to the variable contributions from free carbon dioxide in the pure components and the porous liquid. A comparison of the antisymmetric stretching mode of CO_2 between the pure gas and the dissolved gas incorporated into the sorbents is shown in **Figure 5-8**. The ionic liquid shows the lowest ratio of free to dissolved CO_2 and as opposed to the ZIF-8 which shows the highest ratio. The fact that ZIF-8 signal has a high percentage of free CO_2 is intuitive since its structure has open cages in which the gas can be stored. More interesting is the existence of free gaseous CO_2 in the ionic liquid phase. One explanation of this could be that CO_2 is nonpolar and can nucleate and grow into a microphase separated regime. Both Brennecke and Berne have extensively studied IL carbon dioxide mixtures and found that while the IL is a good solvent for CO_2, a CO_2 rich phase is a poor solvent for the IL.[27-28] Because the CO_2 phase is nonpolar, at higher gas loadings nucleation of the gases could lead to microphase separation or even macroscopic heterogeneity. This is one reason supercritical fluids such as carbon dioxide have started gaining prevalence for use in extractions, purifications, and chromatographic separations since a single phase is achieved.

From computational analysis, the radial distribution function suggests there are two

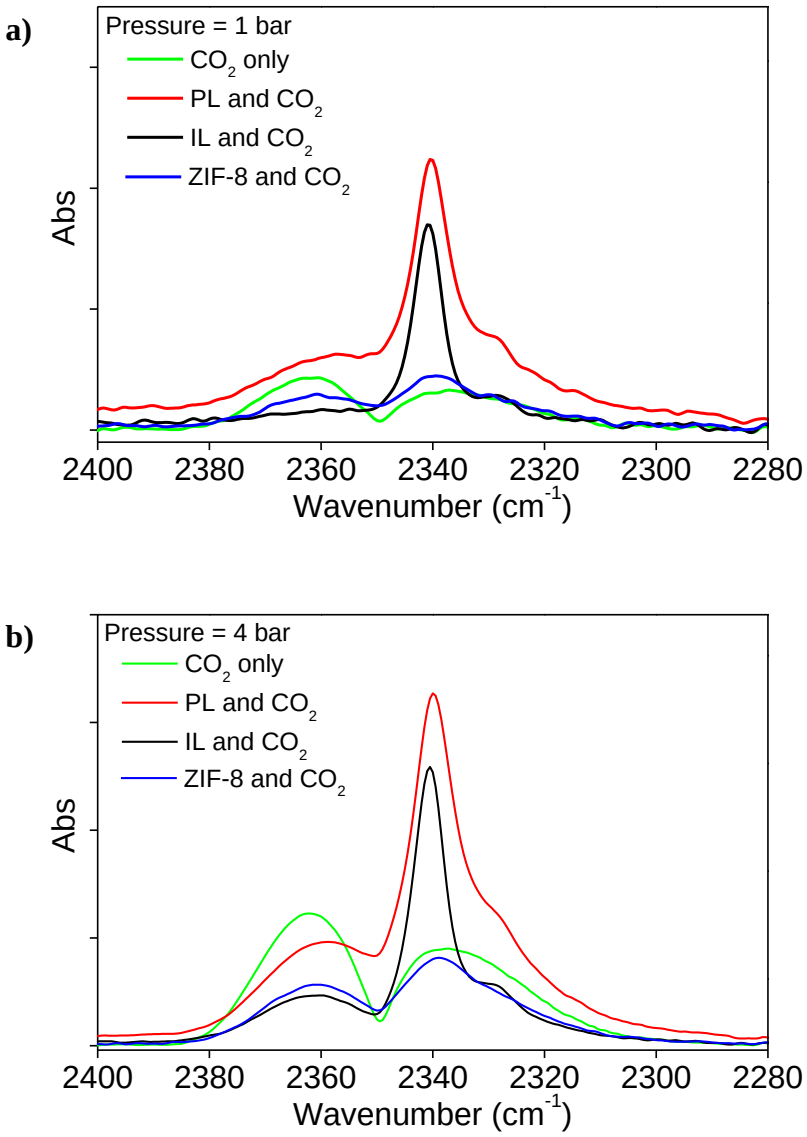

Figure 5-8. Differences in the CO_2 asymmetric stretching region between pure gas and CO_2 sorption into IL, ZIF-8, and PL at 1 bar (a) and 4 bar (b).

primary configurations of the [DBU-PEG] di-cation, where the positive to positive sites vary from a compressed 7.27A to outstretched 9.21A. The AMBER molecular dynamics modelling shows that the cation forms a bowl shape which can expand to hold more carbon dioxide (**Figure 5-9**). This molecular inclusion of CO_2 in the ionic liquid can cause swelling and expansion of the structure that could be analogous to clathrate formation or intercalation.

5.5.3 Relative Quantitation of CO_2

A preliminary evaluation of the data was done to validate the measurement, where the peak height was plotted against the cell pressure for the precursors and the composite PL in **Figure 5-10**. Both regions, asymmetric and bending modes, of carbon dioxide were evaluated. The peak height fits a linear regression with R^2 values of 0.94 or higher for each of the free and dissolved CO_2 peaks. The best correlation was found for the peak height of the 2340 cm^{-1} asymmetric band of dissolved CO_2 with R^2 0.999+ due to negligible baseline or sample interferences. Slightly lower correlation values were found for the bending mode because of interference from an IL peak that overlaps the CO_2 bending mode. Therefore, the CO_2 antisymmetric stretching from 2300-2400 cm^{-1} will be considered since it should remain unaffected by any possible IL swelling.

Notable differences arise in the relative peak intensity between the different samples. In general, the peak height of the free CO_2 peak at 2360 cm^{-1} changes at a different rate than the absorbed CO_2 peak at 2340 cm^{-1}. The free CO_2 peak increases by 5.572×10^{-3} per bar of pressure in the pure IL, while it increases at 1.273×10^{-2} per bar in the PL. This difference in relative intensity is interesting since the absorbed CO_2 peak at 2340 cm^{-1} remains fairly constant, at 3.195×10^{-2} and 3.815×10^{-2} for the IL and PL respectively. A greater change in the free CO_2 versus the absorbed CO_2 provides some preliminary evidence that the incorporation of ZIF-8 allows for storage of the gas in a free cavity rather than purely in the bulk liquid phase or in the ZIF apertures.

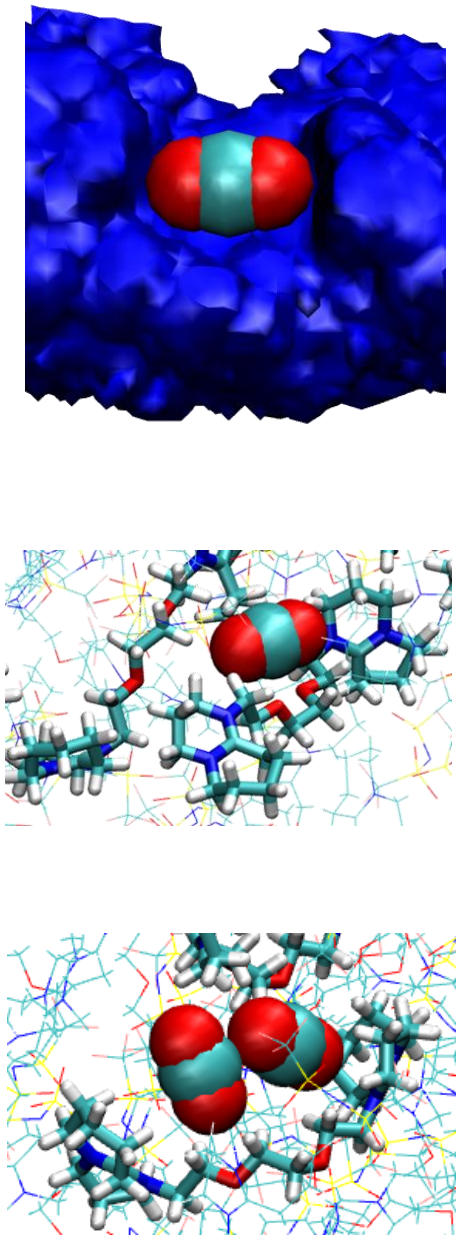

Figure 5-9. Molecular dynamics showing the interactions of carbon dioxide with the ionic liquid. The bulky cation, $[DBU\text{-}PEG]^{2+}$, adopts a bowl shape that expands with increasing CO_2 concentration.

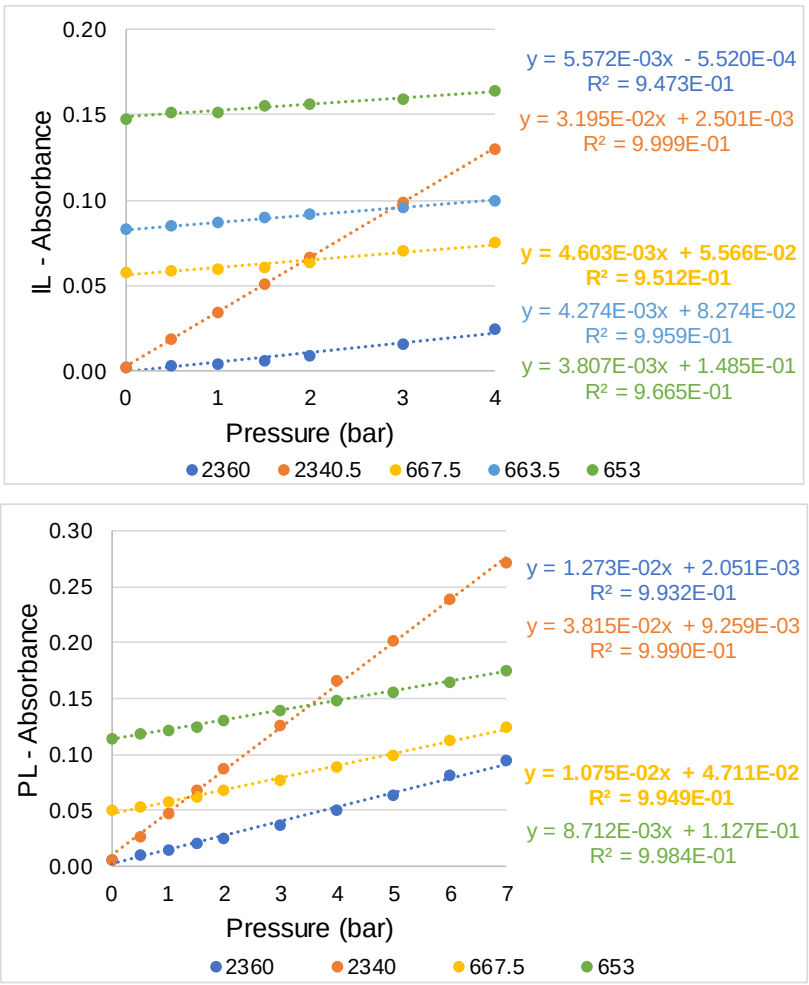

Figure 5-10. Trends in absorbance peak heights with increasing pressure for a) IL [DBU-PEG][Tf_2N]$_2$, b) 20 wt% PL, and c) ZIF-8

In most systems, peak areas provide a better metric for quantitation. The integrated absorbance for the antisymmetric and bending modes of carbon dioxide are presented in **Figure 5-11**. The region of 2285-2385 cm^{-1} was used for integration, since it encompasses the entirety of the CO_2 signal. At low pressures the initial contributions are only from dissolved gas. However, the signal of free CO_2 becomes apparent at pressures in excess of 1 bar, so the inherent deviations from linearity would be better mitigated through a deconvolution of the asymmetric peak. An additional ionic liquid peak at 1050 cm^{-1} and ZIF-8 peak at 995 cm^{-1} were also monitored as a control. In both the porous liquid and ZIF-8, there is no correlation between pressure and peak area. The coefficient of variation in the peak areas is small 0.07% and 1.4% for the porous liquid and ZIF-8. However, in the pure ionic liquid, there is a clear correlation between pressure and absorbance with a negative slope since the incorporation of CO_2 imparts swelling to the IL structure.

5.5.4 IR Pathlength

While absorption measurements are good for quantitation, measurements via ATR are subjected to differences due to penetration depth differences that are dependent on wavelength according to the equation:

$$d_p = \frac{\lambda}{2\pi\sqrt{n_1^2 sin^2\theta - n_2^2}}$$

Where d_p is the probe depth of the IR beam into the sample, λ is the wavelength of interest, n_1 and n_2 are the refractive indices of the crystal and the sample respectively, and θ is the angle of incidence with which the IR beam penetrates the sample. The evanescent wave intensity decreases exponentially with penetration depth. The ATR diamond crystal used here has a refractive index of 2.4 and a 45° angle of incidence. In some cases, the penetration depth has been used by other researchers as the path length for concentration calculations.[5] However, this is not the most accurate representation of the beam path through the sample.

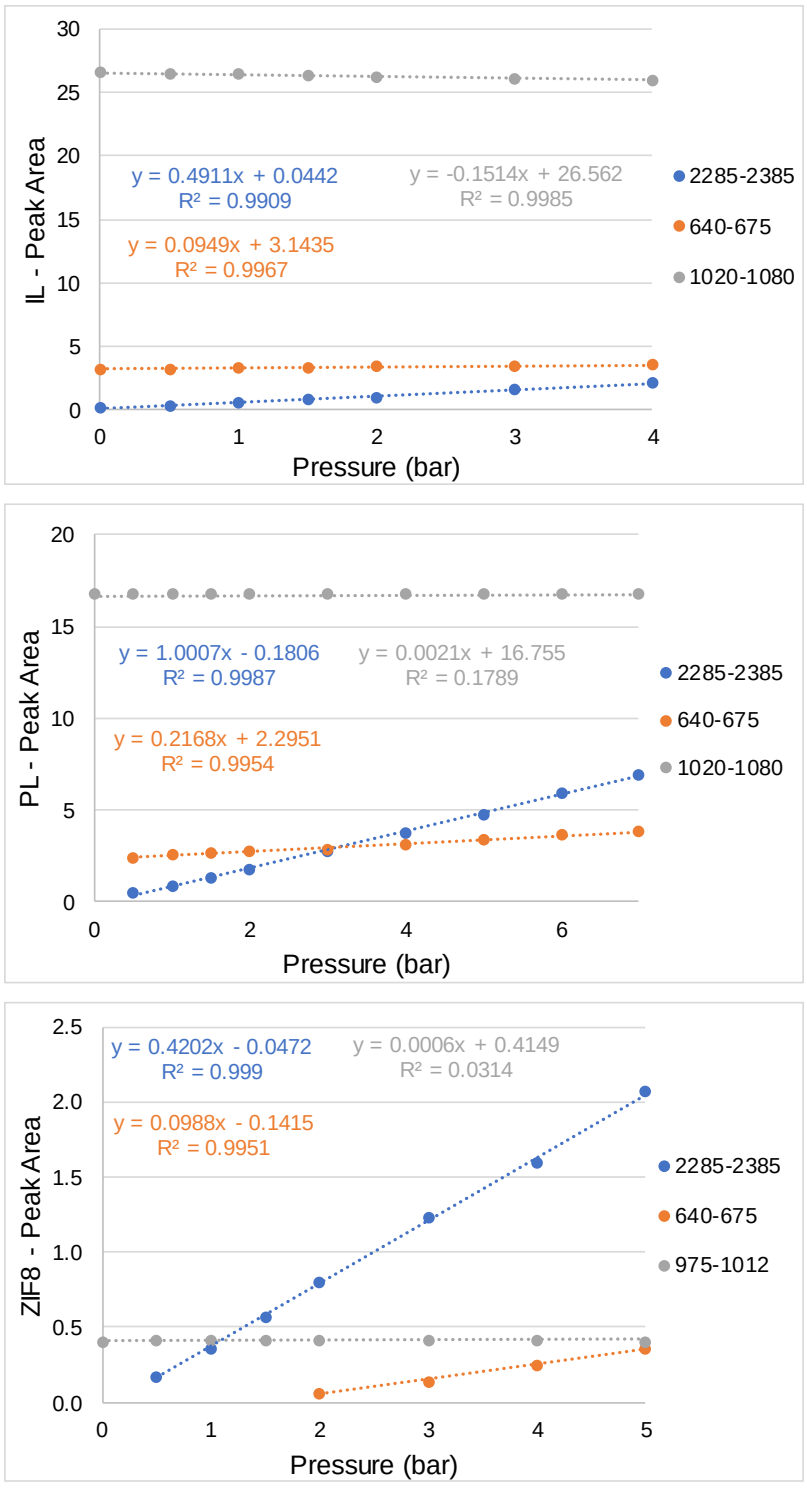

Figure 5-11. Trends in integrated peak areas with increasing pressure for a) IL [DBU-PEG][Tf_2N]$_2$, b) 20 wt% PL, and c) ZIF-8

While the probe depth is important for understanding the region of the sample matrix that is represented by the data, i.e. ATR is primarily a surface technique, to make quantitative concentration measurements the path length must be known precisely. Therefore, the volume of the evanescent wave should be derived from the parallel, $d_{e\parallel}$, and perpendicular, $d_{e\perp}$, polarization of the incident beam to determine the effective path length, d_e.[29]

$$\lambda_1 = \frac{\lambda}{n_1}$$

$$d_{e\perp} = \frac{\frac{n_2}{n_1}\lambda_1 cos\theta}{n_1\pi\left(1-\frac{{n_2}^2}{{n_1}^2}\right)\sqrt{sin^2\theta-\frac{{n_2}^2}{{n_1}^2}}}$$

$$d_{e\parallel} = \frac{\frac{n_2}{n_1}\lambda_1 cos\theta\left(2sin^2\theta-\frac{{n_2}^2}{{n_1}^2}\right)}{n_1\pi\left(1-\frac{{n_2}^2}{{n_1}^2}\right)\left[\left(1+\frac{{n_2}^2}{{n_1}^2}\right)sin^2\theta-\frac{{n_2}^2}{{n_1}^2}\right]\sqrt{sin^2\theta-\frac{{n_2}^2}{{n_1}^2}}}$$

$$d_e = \frac{d_{e\perp}+d_{e\parallel}}{2}$$

By calculating the interaction volume of the evanescent wave from the ATR crystal, we can determine the path length of the IR beam using the refractive index of the ionic liquid or porous liquid. On average, for a single reflection diamond crystal and an estimated sample refractive index (RI) 1.5, the average penetration depth is approximately 2 micrometers, with an effective path length of 4.36 micrometers at 1000 cm^{-1}. From this example, it is easy to see the significant differences between using d_p rather than d_e. Since the exact refractive index of these materials is unknown, an RI of 1.45 was used since it is common for Tf_2N ionic liquids. The feature of interest is the CO_2 peak at 2340 cm^{-1}, therefore, the path of the evanescent wave will be determined for this wavelength. For the pure ionic liquid the approximated penetration depth is 0.77 micrometers, and the pathlength is 1.56 x 10^{-4} cm. The refractive index of evacuated ZIF-8 was previously reported as 1.39, and a calculation proposed to determine the effective refractive index to estimate for solvent filled ZIF.[26] Absolute quantitation for this system may be challenging,

but it provides a validation of the technique to compare with previous gravimetric adsorption experiments.

5.5.5 Concentration Calculations

Using the determined pathlength, *b*, Beer's law can be used to extrapolate the concentration using the integrated absorbance, *A*. Peak integrations are directly proportional to the number of groups and can be analyzed independent of peak shifts and changes in shape. The molar absorptivity, ε, of carbon dioxide in water can be used to approximate the concentration, *c*, of CO_2 in the liquid phase.

$$A = \varepsilon bc$$

The molar absorptivity of CO_2 in water was determined by Maiella et al where the value is 0.89 x 10^6 cm^2/mol or 1.58 x 10^4 cm/mmol when using either peak height or peak area respectively.[30] CO_2 concentration in these sorbents was calculated from the integrated IR absorbance over the 2285-2385 cm^{-1} interval. The ATR calculated concentration was 0.201 mol/L atm for the ionic liquid and 0.203 mol/L atm for the ZIF-8. In previous gravimetric determinations the corresponding concentrations were determined to be 0.051 mol/L atm for [DBU-PEG][Tf_2N]$_2$ and 0.235 mol/Latm for ZIF-8. The high error in the ionic liquid determination is likely due to the approximated refractive index. One possible source of error could be due to the changes in refractive index over different wavelengths, which tend to correspond with peaks of higher absorbance. Averett and Griffiths reported that the accuracy of the above formulas could be improved by using the refractive index as a function of wavenumber, rather than using the average refractive index.[29]

5.5.6 Additional Structure Factors – XRD

To further probe the structure X-ray diffraction (XRD) was used to verify the crystal structure of the porous material and interrogate the liquid structure as well. Prior work from Fujie et al focused on incorporating the ionic liquid into the microporous framework and confirmed loadings of [emim][Tf_2N] into ZIF-8 where the powder XRD

showed no evidence of the broad IL peak, but rather the main difference was a variation in intensity of the 011 and 013 peaks of ZIF-8.[31] Very recently Gomes et al created two new "liquid MOFs" using $[P_{6,6,6,14}][Tf_2N]$ to disperse either ZIF-8 or Mg-MOF-74. Unfortunately the XRD presented was of the materials after washing away the ionic liquid, explaining why the ZIF-8 resembles the pure powder, however Mg-MOF-74 retained features of the IL most likely due the incorporation of IL into the channels.[32]

If the porous phase is indeed isolated from the liquid phase in a non-filling suspension, with the crystal structure and voids maintained, one would expect the XRD of the mixture to resemble the combination of the IL and ZIF-8 in an additive pattern. However as seen in **Figure 5-12** the addition of ZIF-8 further resolved and changed the peak structure of the IL.

Araque et al. recently published an overview that interprets the structure of ILs based on three predominant broad peaks that have been attributed to the polarity, charge, and adjacency of its constituent ions.[33] The lowest q value is peak, typically below 0.6 $Å^{-1}$, is attributed to structural heterogeneity of the sample due to differences in polarity. This peak is absent from the data acquired here which is not surprising since there is no significant nonpolar regime in the symmetric $[DBU\text{-}PEG]^{2+}$ cation, as opposed to many common IL cations which are comprised of long alkyl chains. The middle peak, typically ca. 0.6-1.1 $Å^{-1}$, is indicative of charge alternation which is always present in RTILs, however its presence depends on the magnitude of individual contributions from +/+, -/-, and +/-. The final peak, usually greater than 1.1 $Å^{-1}$, is representative of the adjacency. In the pure [DBU-PEG] IL the charge and adjacency peak overlap and appear as a broad peak with shoulder. However, in the porous liquid the peaks are better resolved, allowing a clearer picture of both the charge peak and the adjacency peak.

5.6 Conclusion

Although uncommon when using ATR, using a consistent purge gas through the FTIR spectrometer provides better resolution allowing a clear picture of in-situ carbon

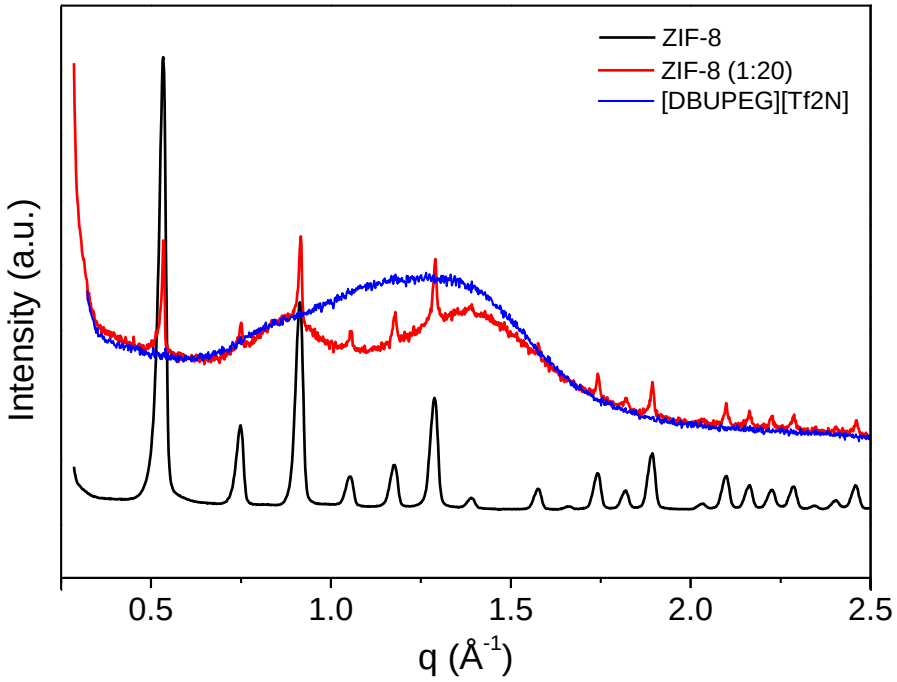

Figure 5-12. XRD of pure ionic liquid (blue) and porous framework (black) with the porous liquid (red) derived from ~5 wt% combination of the two.

dioxide absorption at low pressures. Analysis at low pressures is beneficial because it provides a better representation of the system as it could be implemented as flue gas sorbent or membrane material. The porous liquid formation shows negligible changes from the pure components. From in-situ measurements, the IL shows distinct signs of swelling even at low pressure. The porous liquid doesn't show signs of swelling which further suggests the incorporation of CO_2 into the interior cages of ZIF-8 rather than remaining solely in the interfacial apertures.

5.7 References

1. O'Reilly, N.; Giri, N.; James, S. L., Porous Liquids. *Chemistry – A European Journal* **2007,** *13* (11), 3020-3025.

2. Zhang, J.; Chai, S.-H.; Qiao, Z.-A.; Mahurin, S. M.; Chen, J.; Fang, Y.; Wan, S.; Nelson, K.; Zhang, P.; Dai, S., Porous Liquids: A Promising Class of Media for Gas Separation. *Angew. Chem. Int. Ed.* **2015,** *54* (3), 932-936.

3. Shan, W.; Fulvio, P. F.; Kong, L.; Schott, J. A.; Do-Thanh, C.-L.; Tian, T.; Hu, X.; Mahurin, S. M.; Xing, H.; Dai, S., New Class of Type III Porous Liquids: A Promising Platform for Rational Adjustment of Gas Sorption Behavior. *ACS Applied Materials & Interfaces* **2018,** *10* (1), 32-36.

4. Park, K. S.; Ni, Z.; Côté, A. P.; Choi, J. Y.; Huang, R.; Uribe-Romo, F. J.; Chae, H. K.; O'Keeffe, M.; Yaghi, O. M., Exceptional chemical and thermal stability of zeolitic imidazolate frameworks. *Proceedings of the National Academy of Sciences* **2006,** *103* (27), 10186-10191.

5. Kazarian, S. G.; Briscoe, B. J.; Welton, T., Combining ionic liquids and supercritical fluids: ATR-IR study of CO dissolved in two ionic liquids at high pressures. *Chem. Commun.* **2000,** (20), 2047-2048.

6. Kazarian, S. G.; Vincent, M. F.; Bright, F. V.; Liotta, C. L.; Eckert, C. A., Specific Intermolecular Interaction of Carbon Dioxide with Polymers. *J. Am. Chem. Soc.* **1996,** *118* (7), 1729-1736.

7. Mudunkotuwa, I. A.; Minshid, A. A.; Grassian, V. H., ATR-FTIR spectroscopy as a tool to probe surface adsorption on nanoparticles at the liquid–solid interface in environmentally and biologically relevant media. *Analyst* **2014,** *139* (5), 870-881.

8. Paschoal, V. H.; Faria, L. F. O.; Ribeiro, M. C. C., Vibrational Spectroscopy of Ionic Liquids. *Chem. Rev.* **2017,** *117* (10), 7053-7112.

9. Socrates, G., *Infrared and Raman characteristic group frequencies: tables and charts*. 3rd ed.; Wiley: Chichester, New York, 2001.

10. Hu, Y.; Kazemian, H.; Rohani, S.; Huang, Y.; Song, Y., In situ high pressure study of ZIF-8 by FTIR spectroscopy. *Chem. Commun.* **2011,** *47* (47), 12694-12696.

11. Ordoñez, M. J. C.; Balkus, K. J.; Ferraris, J. P.; Musselman, I. H., Molecular sieving realized with ZIF-8/Matrimid® mixed-matrix membranes. *J. Membr. Sci.* **2010,** *361* (1), 28-37.

12. Ta, D. N.; Nguyen, H. K. D.; Trinh, B. X.; Le, Q. T. N.; Ta, H. N.; Nguyen, H. T., Preparation of nano-ZIF-8 in methanol with high yield. *The Canadian Journal of Chemical Engineering* **2018,** *96* (7), 1518-1531.

13. Wang, B.; Luo, Z.; Elageed, E. H. M.; Wu, S.; Zhang, Y.; Wu, X.; Xia, F.; Zhang, G.; Gao, G., DBU and DBU-Derived Ionic Liquid Synergistic Catalysts for the Conversion of Carbon Dioxide/Carbon Disulfide to 3-Aryl-2-oxazolidinones/[1,3]Dithiolan-2-ylidenephenyl- amine. *ChemCatChem* **2016,** *8* (4), 830-838.

14. Seki, T.; Grunwaldt, J.-D.; Baiker, A., In Situ Attenuated Total Reflection Infrared Spectroscopy of Imidazolium-Based Room-Temperature Ionic Liquids under "Supercritical" CO2. *The Journal of Physical Chemistry B* **2009,** *113* (1), 114-122.

15. Hojniak, S. D.; Silverwood, I. P.; Khan, A. L.; Vankelecom, I. F. J.; Dehaen, W.; Kazarian, S. G.; Binnemans, K., Highly Selective Separation of Carbon Dioxide from Nitrogen and Methane by Nitrile/Glycol-Difunctionalized Ionic Liquids in Supported Ionic Liquid Membranes (SILMs). *The Journal of Physical Chemistry B* **2014,** *118* (26), 7440-7449.

16. Andanson, J.-M.; Jutz, F.; Baiker, A., Purification of ionic liquids by supercritical CO2 monitored by infrared spectroscopy. *The Journal of Supercritical Fluids* **2010,** *55* (1), 395-400.

17. Andanson, J.-M.; Jutz, F.; Baiker, A., Supercritical CO2/Ionic Liquid Systems: What Can We Extract from Infrared and Raman Spectra? *The Journal of Physical Chemistry B* **2009,** *113* (30), 10249-10254.

18. Brinzer, T.; Berquist, E. J.; Ren, Z.; Dutta, S.; Johnson, C. A.; Krisher, C. S.; Lambrecht, D. S.; Garrett-Roe, S., Ultrafast vibrational spectroscopy (2D-IR) of CO2 in ionic liquids: Carbon capture from carbon dioxide's point of view. *The Journal of Chemical Physics* **2015,** *142* (21), 212425.

19. Pasquali, I.; Andanson, J.-M.; Kazarian, S. G.; Bettini, R., Measurement of CO2 sorption and PEG 1500 swelling by ATR-IR spectroscopy. *The Journal of Supercritical Fluids* **2008,** *45* (3), 384-390.

20. Schädle, T.; Pejcic, B.; Mizaikoff, B., Monitoring dissolved carbon dioxide and methane in brine environments at high pressure using IR-ATR spectroscopy. *Analytical Methods* **2016,** *8* (4), 756-762.

21. Ania, C. O.; García-Pérez, E.; Haro, M.; Gutiérrez-Sevillano, J. J.; Valdés-Solís, T.; Parra, J. B.; Calero, S., Understanding Gas-Induced Structural Deformation of ZIF-8. *The Journal of Physical Chemistry Letters* **2012,** *3* (9), 1159-1164.

22. Hu, Y.; Liu, Z.; Xu, J.; Huang, Y.; Song, Y., Evidence of Pressure Enhanced CO2 Storage in ZIF-8 Probed by FTIR Spectroscopy. *J. Am. Chem. Soc.* **2013,** *135* (25), 9287-9290.

23. Liu, H.; Liu, B.; Lin, L.-C.; Chen, G.; Wu, Y.; Wang, J.; Gao, X.; Lv, Y.; Pan, Y.; Zhang, X.; Zhang, X.; Yang, L.; Sun, C.; Smit, B.; Wang, W., A hybrid absorption–adsorption method to efficiently capture carbon. *Nature Communications* **2014,** *5*, 5147.

24. Fairen-Jimenez, D.; Moggach, S. A.; Wharmby, M. T.; Wright, P. A.; Parsons, S.; Düren, T., Opening the Gate: Framework Flexibility in ZIF-8 Explored by Experiments and Simulations. *J. Am. Chem. Soc.* **2011,** *133* (23), 8900-8902.

25. Liu, H.; Guo, P.; Regueira, T.; Wang, Z.; Du, J.; Chen, G., Irreversible Change of the Pore Structure of ZIF-8 in Carbon Dioxide Capture with Water Coexistence. *The Journal of Physical Chemistry C* **2016,** *120* (24), 13287-13294.

26. Radhakrishnan, D.; Narayana, C., Effect of pore occupancy on the acoustic properties of zeolitic imidazolate framework (ZIF)-8: A Brillouin spectroscopic study at ambient and low temperatures. *The Journal of Chemical Physics* **2015,** *143* (23), 234703.

27. Blanchard, L. A.; Hancu, D.; Beckman, E. J.; Brennecke, J. F., Green processing using ionic liquids and CO2. *Nature* **1999,** *399*, 28.

28. Huang, X.; Margulis, C. J.; Li, Y.; Berne, B. J., Why Is the Partial Molar Volume of CO2 So Small When Dissolved in a Room Temperature Ionic Liquid? Structure and Dynamics of CO2 Dissolved in [Bmim+] [PF6-]. *J. Am. Chem. Soc.* **2005,** *127* (50), 17842-17851.

29. Averett, L. A.; Griffiths, P. R.; Nishikida, K., Effective Path Length in Attenuated Total Reflection Spectroscopy. *Anal. Chem.* **2008,** *80* (8), 3045-3049.

30. Maiella, P. G.; Schoppelrei, J. W.; Brill, T. B., Spectroscopy of Hydrothermal Reactions. Part XI: Infrared Absorptivity of CO2 and N2O in Water at Elevated Temperature and Pressure. *Appl. Spectrosc.* **1999,** *53* (3), 351-355.

31. Fujie, K.; Yamada, T.; Ikeda, R.; Kitagawa, H., Introduction of an Ionic Liquid into the Micropores of a Metal–Organic Framework and Its Anomalous Phase Behavior. *Angew. Chem. Int. Ed.* **2014,** *53* (42), 11302-11305.

32. Costa Gomes, M.; Pison, L.; Červinka, C.; Padua, A., Porous Ionic Liquids or Liquid Metal–Organic Frameworks? *Angew. Chem.* **2018,** *130* (37), 12085-12088.

33. Araque, J. C.; Hettige, J. J.; Margulis, C. J., Modern Room Temperature Ionic Liquids, a Simple Guide to Understanding Their Structure and How It May Relate to Dynamics. *The Journal of Physical Chemistry B* **2015,** *119* (40), 12727-12740.

CHAPTER 6. CONCLUSION

6.1 Synopsis

Throughout this dissertation, a variety of carbon capture mediums were explored including ultrathin and dense membrane materials as well as advanced ionic liquid solvents. Conventional ionic liquids that have previously been investigated were focused on relatively small adjustments to the functionalization. One such modification was the lengthening of alkyl substituents, but this systematic approach inadvertently created a bias in molar volume and free volume correlations. Through the creation of new ionic liquid cations in chapter 3, greater free volumes in smaller molar volumes were achieved. This addition of free volume coincided with an increase in the viscosity of the ILs. Through evaluation of several thermophysical properties, these liquids were found to have good thermal stability and gas permeance properties. In a review of the literature, new insights to the proper combination of volume contributions were discovered. The combined attributes of the bicyclic ionic liquids achieved the proper combination of solubility and diffusivity to exceed Robeson's upper bound of permeability and selectivity tradeoffs for membrane separations.

In contrast to adding extrinsic volume through adjustments of packing in the liquid phase, the incorporation of solids with intrinsic porosity have the potential to provide far greater enhancements. It was shown in chapter 4, that through careful selection of a liquid and solid phase, mixed matrix porous liquids can be created. These particular type III porous liquids were comprised of nanoscale porous materials for their ability to persist in solution showing enhanced stability in contrast to other slurries which require mechanical mixing to avoid precipitation. The ordered crystalline structures of metal-organic frameworks were chosen for their well-defined external apertures, making them appropriate for size exclusion, and large internal cages, capable of gas storage. Through the use of two different sized ionic liquid solvents, the flexibility of the zeolitic imidazolate framework-8 (ZIF-8) structure is apparent. Only the larger solvent is successfully excluded from the pores. Preserved internal porosity was observed, as evidenced by a significant decrease in the density of the mixture and positron annihilation lifetime spectroscopy measurements. The porous liquid exhibits distinct enhancement of almost 5 times the

original capacity of the pure ionic liquid phase. Additionally, the ionic liquid medium acts as a gate to the porous material allowing for approximately 5 times higher selectivity in the 30 wt% porous liquid than the pure ZIF-8.

Different from classical liquids, the porous liquid isotherms show substantial hysteresis and delayed desorption. This is similar to the hysteresis seen upon desorption following capillary condensation in mesoporous materials. To further interrogate both the formation of the porous liquid and the mechanism of carbon dioxide sorption, Fourier transform infrared spectroscopy was used. In-situ attenuated total reflectance showed that the CO_2 is physically dissolved into the pure materials and composite. However, at higher pressures the presence of the gaseous CO_2 peak emerges in both the pure and porous liquid suggesting a dual phase system. The only change in the ionic liquid spectrum was a decrease in absorbance from swelling of the IL structure. The integration of ZIF-8 did not distinctly change the chemical environment of the IL, but it removed swelling of the liquid phase at increased gas pressures, by loading of gases into the internal cages of the porous material rather than in the extrinsic vacancies in the liquid. The ZIF-8 structure shows greater changes on absorbance of carbon dioxide, suggesting the possibility of both interfacial and internal absorption. Relative quantitation from peak height and integrated areas provided insight to the fractional composition of CO_2 phases present, unique to these relatively low pressure measurements with stable backgrounds.

VITA

Jennifer A. Schott was born in St. Louis, Missouri. Following high school, she received the Board of Governors full academic scholarship to Missouri State University. Here, she completed her Bachelor of Science in Chemistry in 2012. During her undergraduate career, she was inspired by the research opportunities in the chemistry department and decided to continue her education in the lab of Dr. Erich D. Steinle. She defended her thesis "Anion Selective Polymeric Membrane Electrodes based on Lanthanide Metalloporphyrins" in 2014 and graduated with her Master of Science in Chemistry. Still eager to pursue science, she accepted an assistantship in the doctoral program at The University of Tennessee, Knoxville in August 2014. In January 2015 Jennifer joined the research group of Dr. Sheng Dai and began working on the gas separations project. During her graduate education, she had the privilege of working with researchers in the Nanomaterials Chemistry Group at Oak Ridge National Laboratory and others in the Chemical Sciences Division. In March 2019 she completed the requirements for a Ph.D. in chemistry.